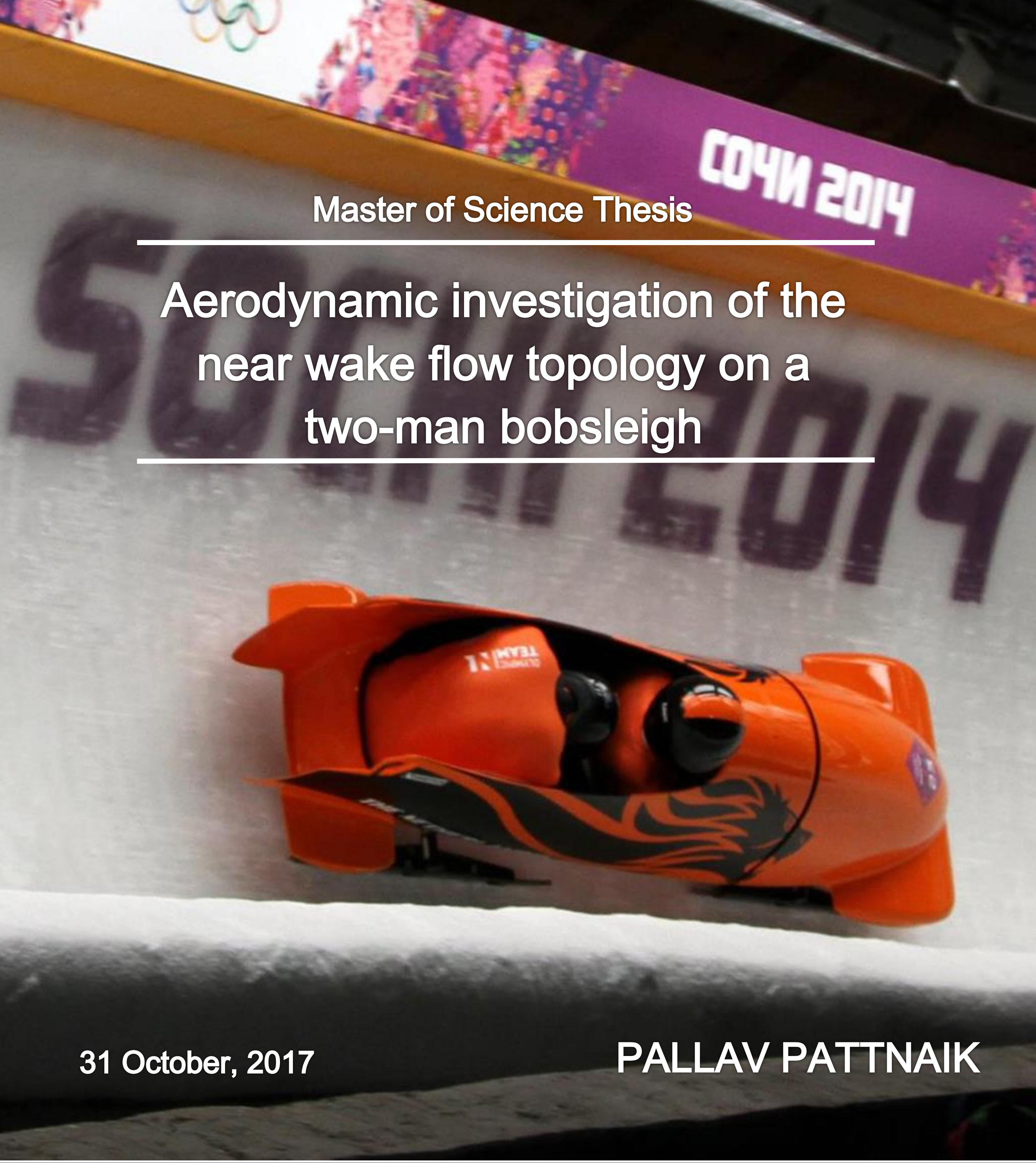

Master of Science Thesis

Aerodynamic investigation of the near wake flow topology on a two-man bobsleigh

31 October, 2017

PALLAV PATTNAIK

Faculty of Aerospace Engineering

Delft University of Technology

Aerodynamic investigation of the near wake flow topology on a two-man bobsleigh

by

PALLAV PATTNAIK

to obtain the degree of Master of Science
at the Delft University of Technology,
to be defended publicly on Tuesday October 31, 2017 at 14:00.

Student number:	4502906		
Project duration:	December 06, 2016 – October 31, 2017		
Thesis committee:	Prof. Dr. Ir. F. Scarano,	TU Delft-Aerodynamics	
	Dr. A. Sciacchitano,	TU Delft-Aerodynamics	supervisor
	Dr. B. W. van Oudheusden,	TU Delft-Aerodynamics	
	Ir. W. A. Nando Timmer,	TU Delft-Wind Energy	

TU Delft

Delft University of Technology

Preface

The Master's programme in aerodynamics at a highly reputed University such as the TU Delft was a dream for me. I started my TU Delft journey in the Aerodynamics track of the faculty of Aerospace Engineering back in 2015. Coming from a Mechanical Engineering background, I was quite fascinated to learn some of the most interesting concepts in aerodynamics. The application of various experimental techniques to improve performance of speed sports caught by attention in particular as I was always into sports right from my childhood. The course on Flow Visualization Techniques in the first year helped me gain more knowledge in the experimental aerodynamics domain. My internship at Inalfa Roof Systems was in the aero-acoustics field and I was assigned the project of minimizing wind buffeting phenomenon in cars of different sizes. This was a quite challenging research assignment and I thoroughly enjoyed my time working on it. Finally, when I had the opportunity to work on bobsleigh aerodynamics for my thesis, I was quite excited because of two of my favourite things – 'aerodynamics' and 'sports' came together.

I am highly grateful to my family for supporting me in pursuing this dream despite the difficult conditions at home. This thesis would not have been successful without them and their prayers. I would like to convey a special gratitude to my brother Pulkit Pattnaik for being very supportive and understanding during my journey at TU Delft. This thesis is a culmination of all the efforts taken by me and all those who have been a part of this unforgettable experience over the past 11 months. I would like to dedicate this thesis to my parents Mr. Ashok Pattnaik and Mrs. Mita Pattnaik.

I would like to express my deepest gratitude to my supervisor Dr. Andrea Sciacchitano for all his input, feedback and help during the entire research and especially during the experimental research campaign. His valuable guidance at every phase of my thesis inspired me to dig deeper into the project. I also thank him for involving me in the ISEA conference paper. I would like give a special mention for my dear colleagues Giuseppe, Stefano and Kahin for their most valuable opinions and resourcefulness.

I would like to thank Nico van Beek, Frits Donker, Leo Molenwijk, Stefan Bernardy, Colette and rest of the support staff at the Aerodynamics Lab for their help with setting up the test bench and easing out the daily activities for me.

Finally, the numerous friends that I made during the past two years deserve a mention. Without them life after working hours would be utterly boring. Yash Shah, Subhajeet Rath, Sumedh, Alessandro, Eugenio, Szymon, Yash Dugar and all the others, thank you for being there and keeping my spirits up.

PALLAV PATTNAIK

Delft, October 2017

Abstract

Drag measurements on bluff-bodies such as bobsleighs using force balance systems have been in prevalence for a few decades. However these studies do not reveal anything on the flow behaviour around the body. In the recent past, various flow visualization techniques have been applied to investigate the flow behaviour around bobsleighs. Even though these studies have highlighted the qualitative flow features, there is a lack of a deep insight into the wake flow topology and the behaviour of the flow structures that are formed in the highly three-dimensional flow. Additionally, when the bobsleigh moves in a curvilinear path, the front cowling rotates with respect to the rear cowling, causing an increase in the frontal area exposed to the wind and in turn a higher drag. However, this perception is not quite straightforward and requires a thorough understanding of the mechanisms and sources of drag generation, in particular at different front cowling angles.

Stereoscopic Particle Image Velocimetry has been used to study the near-wake flow topology of a scaled bobsleigh model. From the velocity field information obtained from PIV, the pressure field in the wake of the bobsleigh model is determined from the Pressure Poisson Equation (PPE) using the methodology outlined by Oudheusden [41]. With the knowledge of the velocity and the pressure fields, the aerodynamic drag is computed using the control volume approach on a wake plane which is at approximately two diameters from the model. The drag obtained from PIV is compared to that obtained from balance measurements. The effects of different bobsleigh configurations on the aerodynamic drag is observed. Secondly, uncertainty quantification of the aerodynamic drag is performed. Finally, a Proper Orthogonal Decomposition (POD) analysis is performed for the velocity fluctuations in order to gain an insight on the motion of the flow structures formed in the wake.

The investigation of the near wake flow topology of the bobsleigh reveals the presence of two counter-rotating vortices with a significant downwash between them in case of the reference configuration. The motion and behaviour of these vortices is obtained by performing the PIV analysis on multiple vertical wake planes. The investigation of the effect of the front cowling misalignment on the drag reveals that there is a reduction of drag for smaller misalignment angles (upto 5°) and a marginal increase in drag for further increase of misalignment (from 5° to 20°). From the analysis of aerodynamic drag conducted on a vertical plane that is approximately two diameters behind the model, it can be seen that the momentum deficit is the highest contributor to the aerodynamic drag (88%) followed by the Reynolds stresses (9%) and pressure (3%). It is also observed that the aerodynamic drag obtained is in good agreement with the results obtained from the balance measurements with a variation of only 2 to 3%. The uncertainty analysis of drag shows that among the different flow variables which affect the drag, the average pressure has the maximum uncertainty. Finally, the POD analysis of the velocity fluctuations shows that the first two fluctuating modes which are the most energetic are not perfectly correlated to each other due to the highly three-dimensional nature of the flow.

Contents

Nomenclature

ρ_∞	Freestream Density	kg/m^3
V_∞	Freestream velocity	m/s
C_d	Drag coefficient	-
A	Total frontal area	m^2
a_∞	Freestream speed of sound	m/s
M_∞	Freestream Mach number	-
τ	Wall shear stress	N/m^2
Re	Reynolds number	-
Re_{crit}	Critical Reynolds number	-
z_0	Distance between the lens and image plane	m
Z_0	Distance between the lens and object plane	m
M	Magnification of the lens	-
f	Focal length of the lens	m
δz	Depth of the field	m
$f_\#$	f-stop or f-number of the camera	-
λ	Wavelength of the light	m
τ_p	Particle response time	s
d_p	Particle diameter	m
μ	Dynamic viscosity of the fluid	Pa s
S_k	Stokes number	-
τ_f	Flow characteristic time	s
u_p	Particle velocity	m/s
$\bar{u}, \bar{v}, \bar{w}$	Time-averaged velocity components	m/s
u', v', w'	Fluctuating velocity components	m/s
p_∞	Freestream pressure	Pa
Fx, Fy, Fz	Force components	N
Mx, My, Mz	Moment components	Nm

$\bar{F}_{Drag}$	Time-averaged drag	N
ϵ_N	Nozzle blockage correction factor	-
ϵ_s	Solid blockage correction factor	-
$U_{\bar{w}}$	Uncertainty in freestream velocity	m/s
N	Number of samples considered for time averaging	-
PPE	Pressure Poisson Equation	-
f_{acq}	Acquisition frequency	Hz
d_τ	Particle image diameter	m
l_x	Length of camera sensor	m
L_x	Length of measurement plane	m
$\vec{n}$	Normal vector	-

List of figures

List of Tables

1

Introduction

Bobsleighing is one of the most popular winter Olympic sports that has gained a lot of attention in the field of speed sports owing to the nature of its close and exciting races. It is a sport wherein two or four athletes from the same team make timed runs down narrow, twisting, banked, iced tracks in a gravity-powered sled. The sled which finishes all the timed runs in the least possible time is considered as the winner. At the highest level of sport, bobsleighing is a combination of speed, agility and fearlessness. It tests the skills of the athletes to maneuver the steep and winding chutes at speeds as high as 150 km/h and G-forces of upto 5g. To remain competitive at this level, it is crucial to take the aid of science and technology in order to have an upper hand over other athletes. Realizing this, the bobsleigh athletes have utilized even the minor technological advancements made in the field of bobsleighing and have continuously raised the bar for the sport. With all the technological advancements, the sport has become faster and faster and nowadays it is often referred to as the 'Formula 1 of the Winter Games'. The margin of win of a typical bobsleigh race is only a few hundredths of a second [1]. From the time the two-man version of the competition was introduced back in 1932 Winter Olympics at Lake Placid, USA till the recent Winter Olympics at Sochi in 2014, the run times have reduced by 54%. From the time the sport has made its first appearance in the Winter Olympic Games in 1924 [2], it has seen quite a lot of advancements in terms of bobsleigh and track design. The total time taken for a typical bobsleigh run depends on the design of the track in particular. The increase of competitiveness in the sport has led to quite a lot of research in the field of bobsleigh aerodynamics. It has compelled the researchers to look for superior aerodynamic design improvements to gain competitive advantage.

Figure 1.1: Two-part bobsleigh configuration. Reproduced from R. Starkman - Toronto Star (December 2009) [3]

The key to a successful race is the ability to get off to a good start as during this phase the sled can go faster whereas during the remaining part of the race, it has to be prevented from slowing down. The modern bobsleigh competition is held over several runs down an iced track. The pilot skills also play a very crucial role in maneuvering the bends and slopes of the bobsleigh track. A good start to the race is necessary because a rule of thumb is that 1/10th of a second lost at the start will result in a loss of 3/10th at the finish line [4, 5]. The primary objective that is to be achieved in order to reduce the total run time is to reduce the aerodynamic drag on the bobsleigh. Even a small reduction of the drag on the sled could lead to a large reduction of run times. Apart from the pilot skills and a good start, another parameter that results in a better outcome is the equipment. The use of bobsleigh equipments that are aerodynamically optimized leads to a significant drag reduction. As a result, a lot of focus has been given to research on shape optimization of the bobsleigh geometry so as to reduce the aerodynamic drag.

This study focuses primarily on the investigation of the dominant flow structures formed in the near wake of a scaled bobsleigh model in order to gain a thorough understanding of the possible mechanisms of drag generation. This aspect of the research on the aerodynamics of bluff bodies is currently missing among all the work that has been done and needs to be explored. Even though some limited studies have been reported in open literature, a deep insight on the interaction of the fluid flow with the bobsleigh and the athletes involved is not available.

1.1. Bobsleigh aerodynamics

The performance of a bobsleigh depends upon several factors such as crew position and posture, the sleigh handling by the crew and on the way in which the bobsleigh interacts with the surrounding environment. The performance is also highly influenced by the aerodynamic design of the bobsleigh. The pattern of fluid flow around the bobsleigh determines the drag on the sleigh. The drag on the sleigh depends upon the freestream conditions as can be seen from the Eqn. (1.1).

$$F_{Drag} = \frac{1}{2} \times \rho_\infty \times (V_\infty)^2 \times C_d \times A \tag{1.1}$$

In Eqn. 1.1, F_{Drag} represents the aerodynamic drag, C_d represents a dimensionless number called the drag coefficient, A represents the total frontal area of the bobsleigh, V_∞ represents the freestream velocity and ρ_∞ denotes the freestream density. The drag coefficient and frontal area, both, depend on the particular configuration of the bobsleigh.

The flow around the bobsleigh is characterized by non-dimensional parameters like Mach number (Ma) and Reynolds number (Re). The Mach number gives an indication of the flow regime. On the basis of the range of variation of Mach number, the flow regime is determined. For Mach numbers less than 0.1 ($Ma <$ 0.1), the flow is incompressible. Bobsleighing is a sport wherein the speeds are relatively low (around $Ma = 0.1$). As a result, it can be assumed that the flow conditions are in the incompressible regime and that the density is constant [6, 7].

The Reynolds number of the flow gives an indication of the viscous nature of the flow and affects the boundary layer characteristics [6, 7, 8] to a large extent. The Reynolds number also gives a measure of the turbulence in the boundary layer and the ability to withstand the adverse pressure gradients [8]. The average Reynolds numbers of a full-scale bobsleigh over a typical bobsleigh run is 1.4×10^6 per meter length of the sleigh [9]. This value lies in the turbulent flow regime and hence most interesting flow features deal with turbulent boundary layers. The critical Reynolds number at which the boundary layer changes from laminar to turbulent is approximately 5×10^5 [6, 10]. At this particular Reynolds number, the thickness of the laminar and the turbulent boundary layers are equal. The flow behaviour is also influenced by other parameters like surface roughness, turbulence in the flow and the adverse pressure gradients [6]. These factors influence the transition from a laminar to a turbulent boundary layer.

1.1.1. Bluff body aerodynamics

Bodies, such as bobsleighs, where the drag is dominated by the shape and strongly influenced by flow separation, are called bluff - bodies [6, 8, 11, 12, 13, 14]. The flow around a bobsleigh can be compared to the flow around other standard bluff-bodies such as cylinders and spheres, thus making it a part of the widely studied branch of aerodynamics known as the bluff-body aerodynamics. The drag coefficient of a bobsleigh depends slightly even on the Reynolds number apart from the configuration of the bobsleigh. The Reynolds number of the scaled bobsleigh model used in this study is around 1.7×10^5 (Re_{model}). Figure 1.2 shows that there is noticeably a significant reduction in the drag coefficient in case of a cylinder around a Reynolds number of 5×10^5 (Re_{crit}) which is very slightly higher than the Reynolds number of the scaled bobsleigh model. This effect is known as the Reynolds number effect in experimental aerodynamics. Hence, in order to achieve a lower drag and to ensure a turbulent flow, the Reynolds number of the model is needs to be increased upto the critical value by adding some roughness. Even though the front cowling of the bobsleigh is streamlined, the surface which joins the front to the rear cowling is not smooth and it has sharp edges. As a result the separation occurs at fixed points unlike the case of a cylinder wherein the points of separation can be varied depending on the Reynolds number of the flow. Hence the separation in case of the bobsleigh has lesser dependence on Reynolds number as compared to that of a cylinder. Due to this low dependence on Reynolds number, the sources of drag generation and the mechanisms responsible for aerodynamic drag remain the same between a scaled bobsleigh model and a full-scale model inspite of no Reynolds similarity.

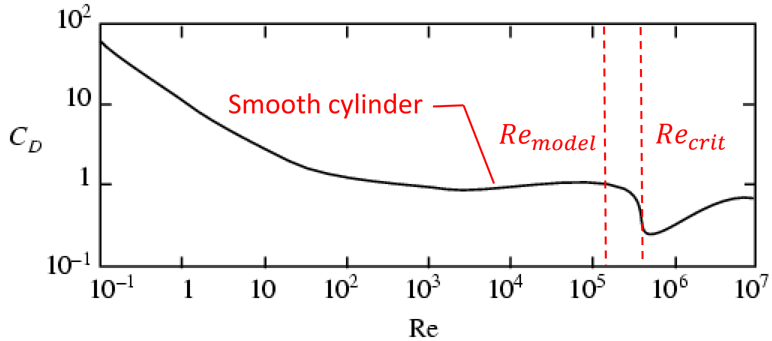

Figure 1.2: Coefficient of drag against Reynolds number for a circular cylinder. Adapted from Weisstein (2007) [15]

The flow separation in case of bluff bodies leads to the formation of a large wake. The wake is a region of low pressure and decelerated fluid flow formed right behind the bluff object. Due to the shape of the bobsleigh, there is a pressure difference created between the front of the body and the wake of the body. The main reason for this pressure difference is the separation of flow at regions of high curvature and sudden geometrical changes like the pilot helmet and the cowling cavity [16]. This leads to adverse pressure gradients and ultimately to the formation of a wake. The drag force caused by the pressure difference resulting from the formation of the low pressure wake is known as the pressure drag or form drag. In case of bluff bodies, the pressure drag is the major component of drag force. This component of drag force can be minimized by aerodynamic shape optimization of the bluff-body. The other component of drag is the friction drag and it arises due to the viscosity of the fluid. The pressure drag increases and the skin friction decreases as the bluffness the body (L/D) increases. This can be observed in Figure 1.3.

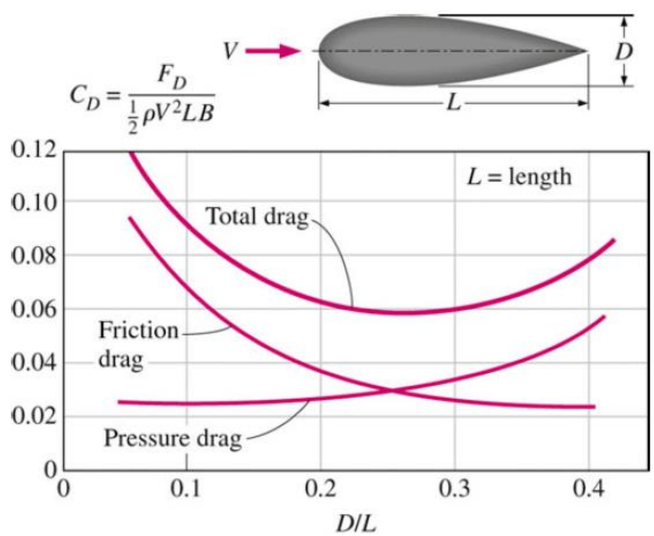

Figure 1.3: Variation of drag components with bluffness of a body. Adapted from Flay [8], original work by Cengel et.al. [17]

1.1.2. Cowling aerodynamics

A bobsleigh contains two parts namely the front cowling (nose) and the rear cowling (see Figure 1.1). These two parts are generally rotated about a pivot point with respect to each other so as to have a smooth cornering of the bobsleigh on the iced track. The two parts are misaligned for majority of the race and there is a gap present between them. Due to the presence of this gap, the frontal area increases and hence the aerodynamic drag increases as well [14, 18]. The flow around the bobsleigh can enter the rear cowling cavity and hence can alter the internal flow behaviour. The nose radius and the presence of sharp edges influence the flow separation on the front cowling. The shape of the nose plays a crucial role in the development of the total drag [19] and in improvement of the performance of the bobsleigh at low Reynolds numbers. In the presence of sharp corners, the separation is independent of the Reynolds number [8]. As the corner radius is increased, the corners become smoother and thus the drag gets reduced and becomes more Reynolds number dependent. As the fluid flows over the bobsleigh, it passes over the nose and first encounters the sharp edges of the cavity. It separates at the edges and forms a wake [20]. The fluid passing over the rear cowling is partly ingested into the cavity due to the low pressure wake that is formed inside the rear cowling. This can be seen in the flow visualization in Figure 1.4.

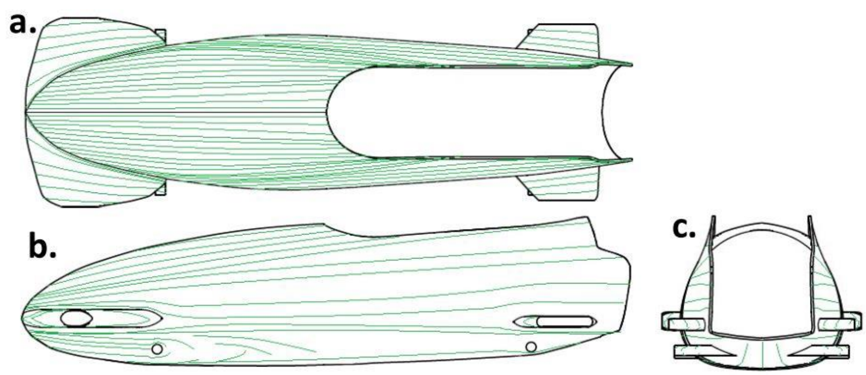

Figure 1.4: Interpreted streamlines over the bobsleigh. Reproduced from Chowdhury et al. [20]

From Figure 1.4, it is observed that, the streamlines in the first half of the rear cowling are directed into the bobsleigh cavity due to the low pressure wake whereas those on the rear half remain parallel to the geometry.

1.1.3. Bobsleigh cavity flow

During the fluid flow over the bobsleigh, sharp edges are encountered at the cowling cut out and this results in flow separation followed by the formation of a low-pressure wake. As the separation becomes more severe, the pressure in the wake decreases and this reduced pressure increases flow ingestion over the sidewalls into the cavity [14, 19, 20]. This ingestion causes twisting of the streamlines towards the rear cowling cavity. The behaviour of the cavity flow with respect to a bobsleigh geometry can be found seen in Figure 1.5.

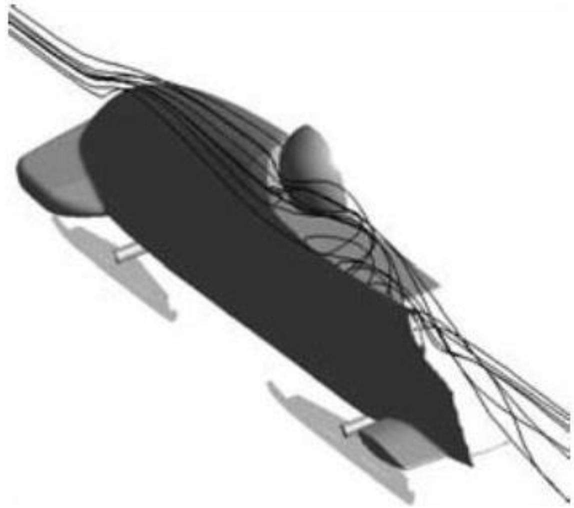

Figure 1.5: Vortex shedding in the bobsleigh cavity. Reproduced from Winkler et al. [14]

Twisting of streamlines can be observed due to the flow ingestion and they contribute significantly to the increase in drag due to a negative pressure coefficient [7, 14] in Figure 1.5. The streamlines form closed recirculation regions and this leads to a vortex formation. It can be seen that the vortex formation is initiated in the cavity of the rear cowling. The vortex shedding shown in Figure 1.5 is highly irregular due to the complex three dimensional nature of the flow. The twisting streamlines corresponding to these vortices are a potential drag source.

1.2. Drag measurement studies

Due to the high speeds (up to 150 km/h) and bluff body shape, bobsleighs are subject to large air resistance, which has great impact on the sport performance. In bobsleighing, the aerodynamic drag accounts for roughly 25% of the total drag [21]. Literature survey reveals that quite some work has been done on drag investigations of a 2-man bobsleigh. Various factors affecting the drag on the bobsleigh have been investigated in detail. Some of the important factors include optimal crew position and posture, shape of the front cowling and wake formation in the cavity of the bobsleigh.

1.2.1. Brakeman position

The angle of inclination of the athlete's (brakeman) body with respect to the bobsleigh plays a major role in the determination of drag coefficient [14, 19, 22]. Previous investigations carried out by Winkler et al [14, 60] show that the aerodynamic drag is significantly affected by crew position and posture. A lot of work has been done by Dabnichki et al. [4, 19] on optimization of the crew position and posture in order to minimize drag. Experiments have been performed on several body inclination angles in the range of 0° and 90° and an optimal inclination angle has been determined.

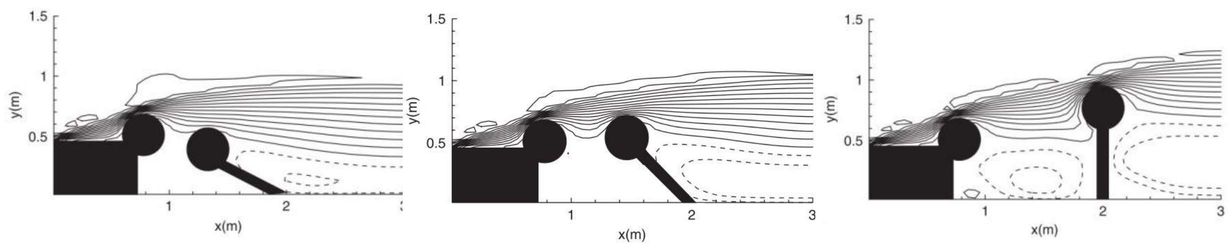

Figure 1.6: Contour plots of axial velocity for brakeman varying positions at an inclination of 30° (left), 60° (centre) and 90° (right). Reproduced from Dabnichki et al. [9]

Figure 1.6 shows that the formation of the recirculation regions behind the brakeman and in between the athletes. It is observed that among the three configurations shown in Figure 1.6, the minimum circulation is obtained in the case of the 60° case. The 90° case produces the highest drag due to the formation of an open separated region behind the brakeman and a closed separated region between the athletes. It was observed that 90° case resulted in a 12% increase in drag compared to the 0° case. The main finding of the work done by Dabnichki et al. [4, 19] was that in the range of 40° to 52°, a reduction of 9.5% is achieved with respect to the 0° case and the optimal angle for minimum drag is around 55°. At this angle, the recirculation region behind the brakeman is reduced to a minimum and no secondary circulation between the two athletes is observed. These results also are in good agreement to the results obtained from the work of Chowdhury et al. [20] as shown in Figure 1.7.

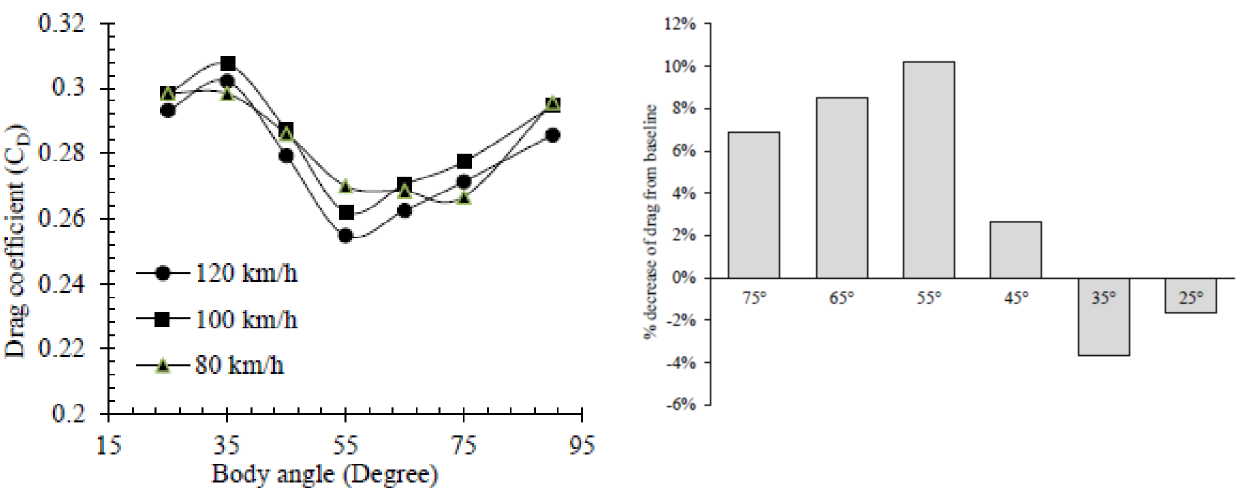

Figure 1.7: Drag coefficient at different speeds (left) and percentage decrease of drag with respect to 0° case (right) as a function of brakeman body inclination. Reproduced from Chowdhury et al. [20]

1.2.2. Front cowling misalignment

The misalignment of the front cowling with respect to the rear cowling has a significant impact on the drag of the bobsleigh. In the recent past, many wind tunnel tests have been conducted in order to investigate the effect of front cowling misalignment on the drag of the bobsleigh. In 2016 Harm Ubbens carried out his master thesis titled “Aerodynamic analysis of cowling misalignment on a two-man bobsleigh” [16]. The objective of Ubbens’ master thesis was to analyze the effect of cowling misalignment on the aerodynamic drag of a two-man bobsleigh using both wind tunnel testing and CFD analyses [16]. A scaled model (scale 1:5.5 – see Figure 1.8) was used as a test model in the Delft University of Technology M-tunnel to perform PIV as well as force balance measurements on various configurations. These tests were validated by performing CFD simulations on the same bobsleigh model as used in the wind tunnel measurements.

Figure 1.8: Wind tunnel model. Reproduced from Ubbens [16]

There are two main findings of this work that are relevant for our research. Firstly it can be observed from Figure 1.9 that for a clean configuration, drag initially decreases upto a certain angle (10°)and increases with further increase in the angle of misalignment of the front cowling [16]. Secondly, it can also be observed from Figure 1.9-left that the drag area decreases with increase in Reynolds number. These results have been obtained using balance measurements.

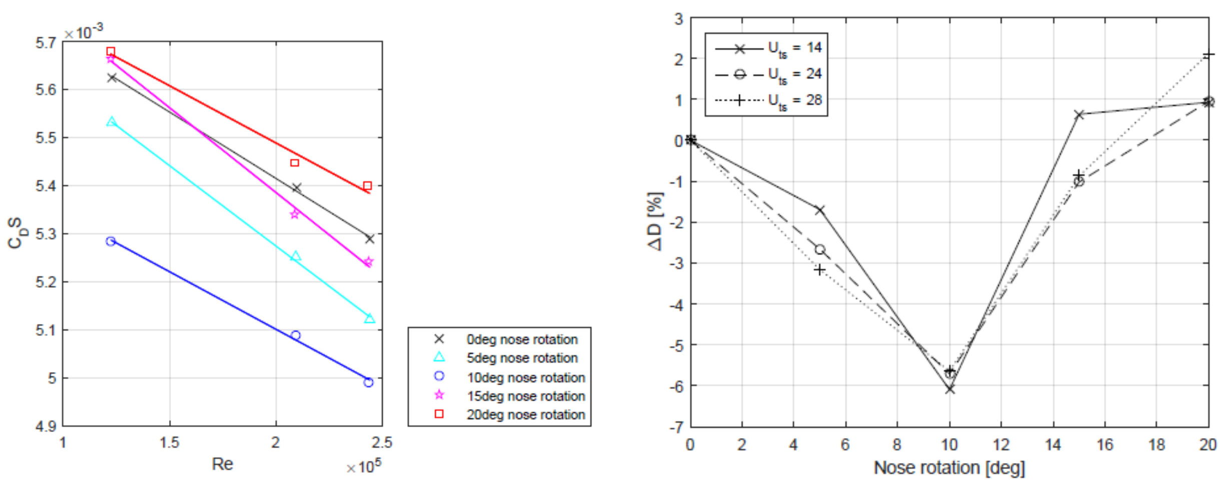

Figure 1.9: Drag area as a function of Reynolds number for different nose angles (left) and percentage change in drag as a function of nose angle for different tunnel speeds (right). Reproduced from Ubbens [16]

The reason behind the increase in drag with nose rotation angle is two-fold. Firstly, the increase in frontal area increases the drag. Secondly, the blockage imposed by the crew creates a momentum deficit inside the cavity. The possible decrease of drag for smaller nose rotation angles is due to the reduction of momentum deficit due to the acceleration of flow between cowling edge and pilot However, the decreasing and increasing trend of the drag has not been clearly explained. The mechanism of drag generation and the formation of the flow structures in the wake have not been investigated in detail.

1.3. Flow visualization studies

Drag reduction studies are performed using balance measurements in a wind tunnel as it is the most accurate method. However, the method involves large number of measurements in order to optimize a particular parameter. For measurements in which the data is to be obtained by changing either the position of the model or by adding or removing aerodynamic attachments, the balance measurements could lead to longer testing times. With the present state of art of flow measurement techniques, it is possible to not only visualize the flow but also derive the forces from it. Several flow visualization techniques have been used in order to gain qualitative information about the flow behaviour. Out of these techniques, smoke flow visualization and flow visualization with woolen tufts have been most commonly used.

1.3.1. Smoke flow visualization

Smoke is used to visualize the flow that is away from the surface of the model. Smoke can be used to detect vortices and regions of separated flow [23]. Smoke-flow visualization [24] is a technique wherein streams of vapor are injected into the flow. The vapor follows a certain path which is known as a filament line. These filament lines are lines constituting all the fluid particles that pass through the points of vapor injection. In steady flow, the filament lines are identical to stream lines [25]. Smoke flow visualization reveals the complete flow pattern around a body. The one major drawback of this technique is that it does not work well at higher flow speeds ($\sim 480 km/h$) [23].

One of the smoke-flow visualization studies that has been carried out in the field of bobsleigh aerodynamics is by Chowdhury et al. [20]. Smoke flow visualization was performed on different regions of the bobsleigh body and around the crew as shown in Figure 1.10. In this work, the smoke stream was only effective at visualizing the flow at low Reynolds number (i.e. at 5 km/h). It was not possible to carry out this visualization at higher Reynolds numbers.

Figure 1.10: Smoke flow visualization on a 1:2 scaled model of a two-man bobsleigh at 120km/h wind speed. Isometric view (left) and close detailed view (right). Reproduced from Chowdhury et al. [20]

Two main observations can be made. It can be seen that the flow below the front bumper (see Figure 1.10-right) is deflected upwards as a result of suction of the streamlines into the bobsleigh cavity due to a low pressure wake. Additionally, the air flow passing over the rear cowling is partly directed into the rear cowling cavity and travels over the crew.

1.3.2. Tuft flow visualization

Tufts flow visualization is an old visualization technique that is used in wind tunnel testing. Tufts are small lengths of string that are frayed on the ends. The tufts are attached to the surface of the model using some adhesive such as tape or glue. As the air flows over the model, the tufts are blown and point downstream. When the entire model is tufted, as shown in Figure 1.11, then regions of strong cross-flow, reverse flow, or flow separation are indicated by the direction of the tufts [23].

Several flow visualization studies have been performed on bluff bodies using tuft flow visualization in particular. One such work is done in the field of bobsleigh aerodynamics by Chowdhury et al. [20]. Wind tunnel tests were carried out with wool-tufts to notice the airflow pattern around the driver and brakeman surrounding region.

Figure 1.11: Tuft flow visualization on a 1:2 scaled model of a two-man bobsleigh at a wind speed of 120km/h (left) and 10 km/h (right). Reproduced from Chowdhury et al. [20]

The effectiveness of the woolen tufts made the tuft flow visualization possible at high Reynolds number. At 120 km/h, the wool-tufts directly behind the front bumper and front axle show significant oscillation. It is also seen that the flow downstream of the front bumper is deflected upwards before following the contour of the bobsleigh model. This phenomenon cannot be seen at 10 km/h wind speed. The air flow which passes over the rear cowling is partly directed into the bobsleigh cavity and travels along the sidewall. It is also observed that first half of the cowling cut-out allows flow into the bobsleigh cavity whereas the flow on the rear half of the cowling is directed parallel to the bobsleigh geometry.

1.3.3. CFD studies

Apart from experimental studies in the wind-tunnels, several researchers have studied bobsleigh aerodynamics using the advanced computational fluid dynamics tools. One such study shown here (see Figure 1.12) shows the viscous flow behaviour around the 2D bobsleigh with no nose rotation at a Mach number of 0.1. This result is obtained by performing a viscous CFD simulation which uses first-order spatial numerical flow integration.

When the viscous flow is analysed (see Figure 1.12- top left), it is seen that the flow accelerates over the head of the pilot. There is a formation of a region of stagnation of the flow immediately upstream of the pilot head and on the nose tip of the bobsleigh. Large recirculating regions are formed inside the nose of the bobsleigh just in front of the pilot head and also in the rear cowling cavity in the wake trailing the bobsleigh.

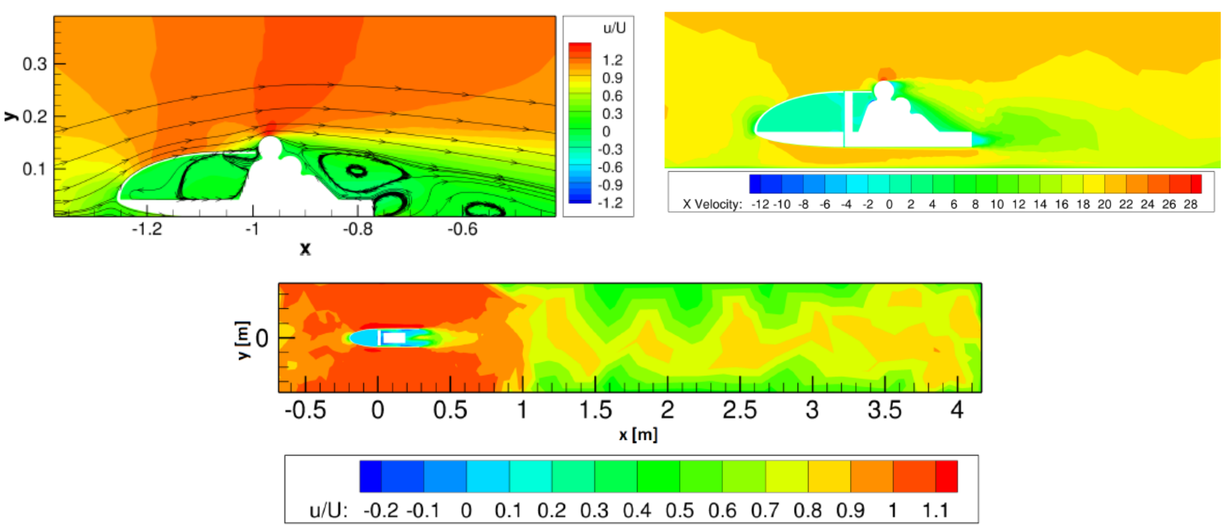

Figure 1.12: Two dimensional viscous flow behaviour around the bobsleigh (top left). Flow around the centerline of the bobsleigh (top right) and flow through the domain (bottom centre) at a freestream velocity of 20 m/s using viscous CFD analysis on a scaled model of a two-man bobsleigh. Reproduced from Ubbens [16]

From Figure 1.12- top right, it is observed that the flow stagnates on the nose and in front of the pilot head. The flow accelerates over the head of the pilot after which it separates. The area of separation formed after the athletes is not large in the center line of the bobsleigh.

The results obtained from this viscous CFD analysis show some similarity to those observed from the other flow visualization techniques in terms of the direction of streamlines and the formation of certain flow patterns. However, the prediction of drag through CFD is inaccurate. Moreover, being such a three-dimensional and complex flow, the results from CFD depend on the choice of turbulence models. The choice of turbulence models varies depending on the geometry. Until now there is not a clear consensus in the CFD community on the applicability of any of the models for such complex geometries. Hence, flow visualization through experimental techniques is the only reliable option for simultaneously visualizing the flow and obtaining accurate forces [26].

1.4. Research Objective and Questions

1.4.1. Research Objective

The main objective of this research is to investigate the near wake flow field of a 1:5.5 scaled bobsleigh model using 2D stereoscopic PIV in order to gain an understanding on the mechanisms of drag generation and on the flow structures generated in the wake. In addition, the objective is to evaluate the drag force from the velocity fields and to obtain pressure fields from the statistically converged time averaged flow-field measurements. Further it is intended to evaluate the uncertainty of the average drag obtained.

1.4.2. Research Questions

The thesis aims at answering the following research questions:

1. How does the near wake flow topology of the bobsleigh model look like?
2. What is the effect of front cowling misalignment on the aerodynamic drag of the bobsleigh model?
3. What is the effect of nose shape on the aerodynamic drag of the bobsleigh model?
4. What is the effect of using passive flow control devices on the near wake aerodynamics of the bobsleigh model?
5. What is the uncertainty of the aerodynamic drag obtained from PIV?

1.4.3. Relevance

Most applications in aerodynamics deal with large scale bodies be it a car or an aircraft. In order to perform an aerodynamic investigation on these large scale bodies, they are usually scaled down to perform wind tunnel tests. Typically, scaling of a model is done based on Reynolds numbers in the case of low-speed flows. Even though the bobsleigh model used in this thesis is not an exact representation of a real bobsleigh (no Reynolds number similarity), the sources of drag generation and the mechanisms responsible for the formation of the flow structures in the wake remain the same. This is because of the fact that the due in case of the bobsleigh model, the separation points are fixed and hence there is very less dependency on the Reynolds number. This thesis serves as a basis for thorough understanding of the near wake topology of a bobsleigh and a deep insight on the flow behaviour is obtained from the resolution of the flow structures. Quantitative evaluation of the velocity, pressure and drag provides an idea on the aerodynamic developments that can be implemented in order to gain faster speeds and to minimize run times. The thesis also illustrated the implementation of several aerodynamic changes and showcases their effectiveness. These key design inputs play a vital role for the future of the field of speed sports and the findings of this work in general is quite exciting for young aerodynamicists.

Thesis Outline

Chapter 2 describes the theory and the various techniques that have been utilized during the experimental campaign for this thesis. The experimental setup used for performing the PIV and balance measurements is described in Chapter 3. This is followed by the data reduction and analysis in Chapter 4. Chapter 5 shows the qualitative and quantitative results obtained from the measurements, and the final conclusions are addressed in Chapter 6.

2

Experimental Techniques

This chapter outlines the different experimental techniques that have been used in this study. Two types of wind tunnel measurements are performed in this experimental campaign. Particle Image Velocimetry (PIV) measurements and force balance measurements are carried out in order to determine the aerodynamic drag of a scaled bobsleigh model. The working principle of these techniques and their application to this study are discussed in detail. The reasons for the choice of these techniques and the expected outcomes from the application of these techniques are also delineated.

In this chapter, the section 2.1 gives a general introduction to PIV as an experimental technique and explains its working principle with a focus on the imaging system, tracer particles and the illumination systems used during the PIV measurements. Section 2.2 discusses the technique used for the evaluation of particle image motion. Section 2.3 discusses in brief the working principle of the Stereoscopic PIV technique that is used for the current study. The methodology of evaluating the forces from PIV data using the control volume approach with a focus on the methodology of pressure reconstruction in particular is dealt with in section 2.4. Finally section 2.5 briefly describes the working principle of a wind tunnel force balance system and its applicability to measure the drag force in case of a scaled bobsleigh model.

2.1. Particle Image Velocimetry

Particle image velocimetry [27] is an imaging based experimental technique that measures the fluid velocity from the displacement of small tracer particles inserted into the flow. The particles are illuminated within a thin light sheet generated from a pulsed light source (typically a double-head pulsed laser system). The light scattered by these tracer particles is recorded onto two subsequent image frames by a digital imaging device, typically a CCD camera placed perpendicular to the measurement plane. A typical layout of a planar PIV measurement system is shown in Figure 2.1. It consists of a laser system with laser optics to create a laser-light sheet, light-scattering tracer particles in the flow, and a lens-camera combination (imaging optics and image plane) to record the location of the particles at different times. The main features of typical PIV setups are discussed in detail in the following subsections.

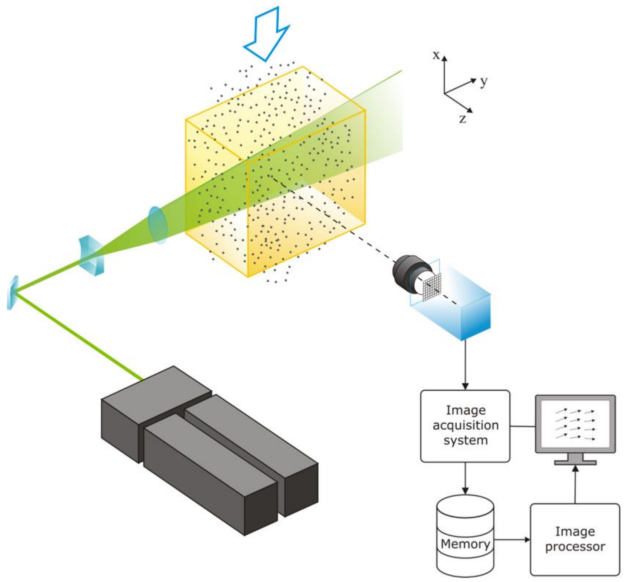

Figure 2.1: Schematic of a typical PIV measurement system. Reproduced from Scarano 2013 [28]

2.1.1. Imaging System

The PIV imaging system consists of a CCD camera which is equipped with an objective (lens) to allow light from the measurement plane (object plane) to be focused on to the image sensor (image plane) of the camera (see Figure 2.2).

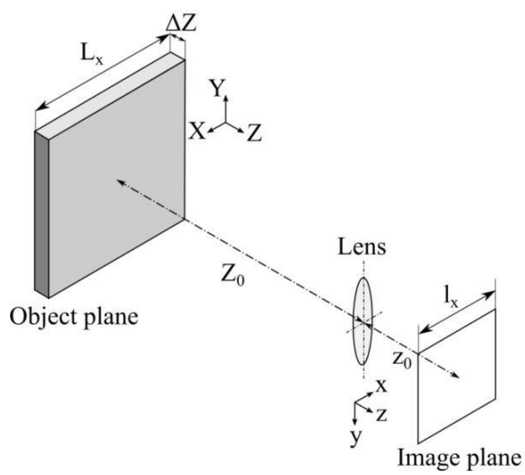

Figure 2.2: Imaging system for PIV. Reproduced from Sciacchitano 2014 [29]

The magnification of the system is given as

$$M = \frac{z_0}{Z_0} = \frac{l_x}{L_x} \tag{2.1}$$

z_0 is the image distance (between lens and image plane), Z_0 is the object distance (between lens and object plane), l_x is the sensor size and L_x is the imaged object size.

Under the assumption of thin lens (lens thickness negligible compared to the focal length), focal length 'f' and optical system distances (z_0 and Z_0) are related via the thin lens equation (Hecht, 2002 [30]):

$$\frac{1}{f} = \frac{1}{z_0} + \frac{1}{Z_0} \tag{2.2}$$

Another critical parameter in the case of large-scale PIV measurements is the depth of field (δz). The *depth-of-field* δz is defined as the thickness of the region containing in-focus particles in the object space. The expression for the depth of field is as follows

$$\delta z = 4.88\left(\frac{1+M}{M}\right)^2 . {f_\#}^2 . \lambda \tag{2.3}$$

The depth-of-field should be at least equal to the laser sheet thickness to minimize the background noise induced by out-of-focus particles. The f-number ($f_\#$ = f/D) controls this optical depth and λ is the wavelength of the laser light.

2.1.2. Tracer particles

One of the major factors affecting the accuracy of the results in PIV is the choice of tracer particles in the flow. The choice should be made in such a way that the tracer particles are small so that they accurately follow the flow without altering the flow properties. However, these particles should be large enough to scatter enough light that can be captured by the camera.

Firstly, in order to assess the capability of the tracer particles to follow the flow, the particle response time is used. Particle response time is defined as the time taken by the tracer particles to respond to a sudden change in fluid velocity. The lower this response time, the more accurately the tracer particles follow the fluid. Properties like density and particle size are of foremost importance for the particles to have low response time τ_p (see Eq. 2.4, [31]). Assuming that the tracer particles operate in the Stokes flow regime, the expression for particle response time τ_p is given by [31]:

$$\tau_p = \frac{{d_p}^2 . (\rho_p - \rho_f)}{18\mu} \tag{2.4}$$

where ρ_p is the particle density, ρ_f and μ are the density and the dynamic viscosity of the fluid and d_p is the particle diameter. In case the tracer particles have comparable densities as that of the working fluid, the difference $\rho_p - \rho_f$ would be very low and as a result, the particle diameters can be larger while keeping low response times. For the tracer particles to follow the surrounding fluid accurately, the velocity lag between the two should be minimized. For this, the response time of the tracer particles needs to be lower than the flow characteristic time (τ_f). The Stokes number defined as $S_k = \tau_p/\tau_f$ determines the suitability of a tracer particle for a particular flow measurement. For a reliable tracing particle, the Stokes Number (S_k) should be of the order of 0.1 or lower [32]. Here, the flow characteristic time is defined as the ratio of a characteristic length scale and a velocity scale.

Secondly, the light scattering capability of the tracer particles are important so that their motion can be accurately captured by the cameras. The scattered light intensity is a function of the ratio of the refractive index of the particles to that of the fluid, of the particles size, shape and orientation and of polarization and observation angles [31]. Typically for particles whose diameters are more than the wavelength of the illuminating light, Mie's scattering theory applies (Mie, 1908). Further, for $d_p > \lambda$, the maximum light intensity is scattered in the forward direction, while the light scattered in backward and side directions is several orders of magnitude lower. Figure 2.3 illustrates the polar distribution of the scattered light intensity of a 1 μm oil particle in air with light wavelength of 532 nm according to Mie's theory.

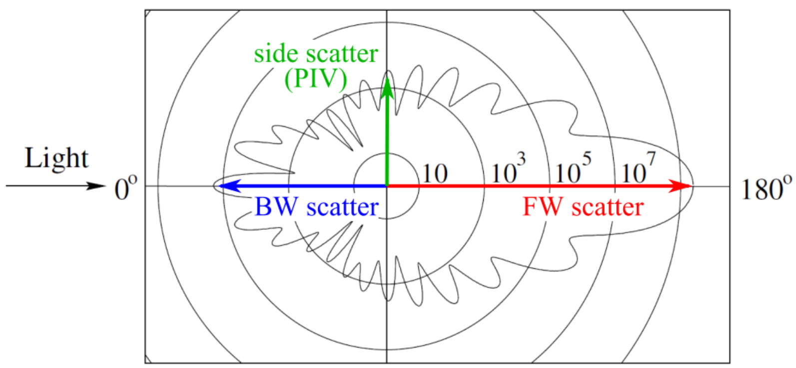

Figure 2.3: Light scattering by a 1 μm oil particle in air. Adapted from Raffel *et al* (2013) [31]

2.1.3. Illumination

The illumination system provides the light that allows the tracer particles to be visible in the recordings. Illumination of the measurement plane is typically achieved with Nd: YAG (Neodymium: Yttrium-Aluminium-Garnet, λ = 1064nm) solid-state laser. These lasers have a very short pulse duration and the ability to emit monochromatic light with high energy density, which can easily be shaped into thin light sheets by means of spherical and cylindrical lenses [29]. The parameters to be selected regarding illumination during the image acquisition phase include the light pulse width δt, the pulse separation Δt and the time interval between subsequent image pairs ΔT (see Figure 2.4). The parameter ΔT is dependent upon the acquisition frequency f_{acq} which in turn determines whether subsequent velocity fields are correlated or uncorrelated in time [29]. The pulse width determines whether the tracer particles are imaged as dots or streaks. The PIV images record a snapshot of the tracer particles as if they were frozen at one time instant so that the particles do not appear as streaks. Hence, there is an upper limit for the pulse width (δt) which can be estimated as the time interval during which the particle image displacement is equal to the particle image diameter (d_τ). This can be seen in the following expression

$$\delta t \ll \frac{d_\tau}{M|u_p|} \tag{2.5}$$

where M is the optical magnification factor and u_p is the particle velocity

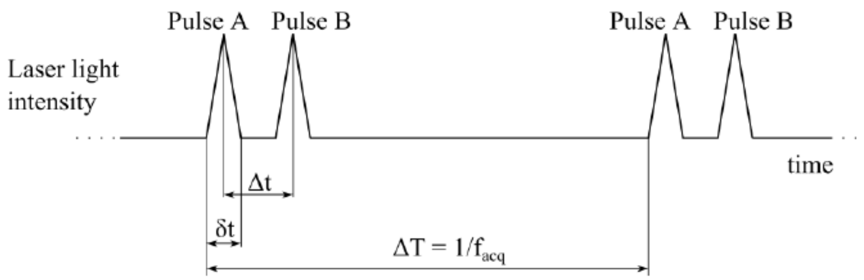

Figure 2.4: Illustration of laser pulse width and pulse separation. Reproduced from Sciacchitano 2014 [29]

2.2. Evaluation of particle image motion

In PIV, the images are captured within a very small interval of time and the relative particle motion is evaluated in that interval. This evaluation involves different steps as discussed below

(a) Image windowing

The entire image is divided into small cells known as interrogation windows each containing a certain number of tracer particles (atleast ten). The local velocity is computed in each interrogation window by taking the average particle velocity in the particular window. Typically the interrogation window sizes vary from 16×16 pixels to 128 ×128 pixels.

(b) Cross-correlation analysis

The cross-correlation procedure compares the corresponding interrogation windows extracted from the two exposures. It generates a correlation map which contains light intensity peaks at several locations within each window. The location of the highest peak is considered as the peak position within each window. The position of the highest peak with respect to the origin (see Figure 2.5) is regarded as the average particle image displacement. At times, the cross-correlation algorithm results in peaks resulting from noise signals or non-paired particles. These peaks can be eliminated by minimizing reflections in the PIV images.

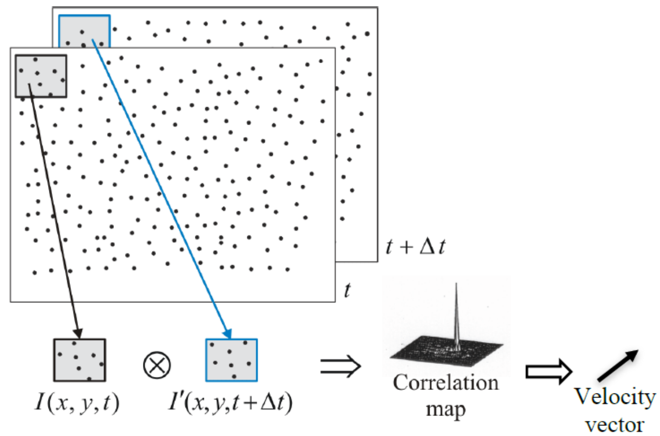

Figure 2.5: Image windowing and cross-correlation map. Reproduced from Scarano 2013 [28]

(c) Correlated peak sub-pixel interpolation

The location of the highest peak is related to the pixel position leading to a pixel shift. Since particle image displacement is not a discrete number of pixels and the correlation function is a discrete function defined at only discrete pixel locations, a more accurate peak position can be found by the interpolation of the correlation peak. In this way, sub-pixel accuracy can be achieved.

(d) Divide by time and scaling

The particle displacement obtained after sub-pixel interpolation is in terms of pixel shift between corresponding windows. This shift is first multiplied by the pixel size to obtain a displacement in the image scale. The velocity in the image scale is obtained by dividing by the time separation between the laser pulses. This velocity in the image scale must be further divided by image magnification in order to obtain the velocity in the object scale.

2.3. Stereoscopic Particle Image Velocimetry

In case of planar PIV, the out-of-plane velocity component is lost while the in-plane components are affected by an error due to the perspective transformation. For highly three-dimensional flows this can lead to substantial measurement errors of the local velocity vector. Due to the shortcomings of the classical planar PIV, there is a need for implementation of two cameras. The method of using two cameras to obtain the out of plane component of displacement has been practiced for several decades for various engineering applications [33].

Working principle of Stereoscopic-PIV

Stereoscopic particle image velocimetry employs two cameras (see Figure 2.6) to image the illuminated flow particles in order to record simultaneous but different perspectives of the same region of interest.

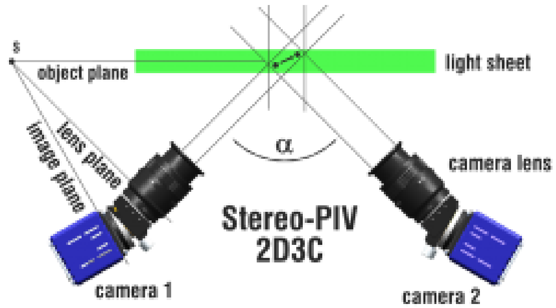

Figure 2.6: Sketch of stereoscopic PIV setup. Reproduced from Lavision [34]

The combination of both camera projections contains sufficient information to reconstruct all three components of displacement vectors in the measurement plane from the two projected planar displacement vectors detected by the two cameras. First of all, the apertures of the two cameras are set such the entire measurement plane is in focus. The Scheimpflug lens arrangements keep both image planes in focus. Geometrical calibration is performed by placing the calibration plate at the location of the measurement plane. This calibration is carried out using the pinhole model [35]. This is followed by the self-calibration procedure [36] and it helps in reducing calibration errors to the order of 0.1 pixels. The calibration makes an accurate relation between the object space and image space with the use of mapping functions [37]. Using this imaging configuration and a laser to illuminate the measurement plane, several sets of images are acquired in the double-pulsed mode in the presence of the tracer particles which are flowing through the measurement plane. Each set of images is then used to reconstruct the positions of the particles based on the calibration. When the positions of the particles are obtained on the measurement plane, a stereo-cross-correlation algorithm yields the velocity vectors by finding average displacements in each interrogation window. The details of the reconstruction process can be found in Raffel *et al* (1998) [31].

2.4. Determination of drag from PIV

During the 1930s, the integral form of the momentum equation was used to measure the drag characteristics of airfoils [38]. Nowadays, it is being frequently used to estimate drag forces using PIV. For this approach, a control volume needs to well-defined as in Figure 2.7 surrounding the body under consideration (in this case, the airfoil).

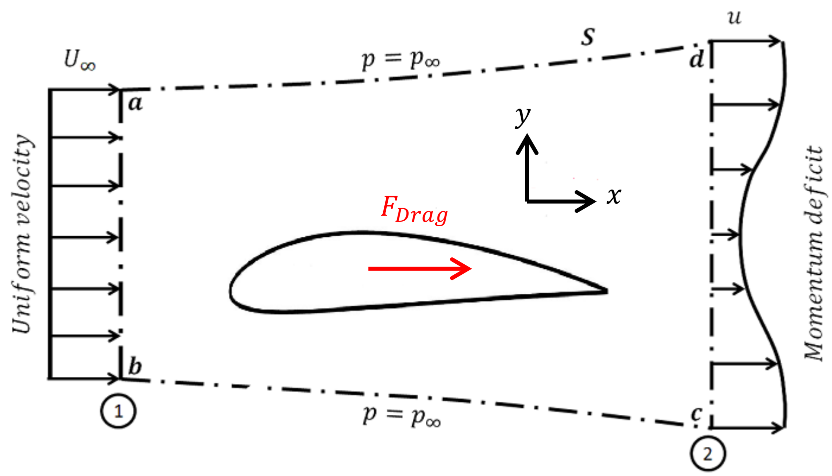

Figure 2.7: Schematic of the control-volume approach to determine drag.

The criteria for defining this control volume are as follows:

1. Lines ab and cd must be far upstream and downstream respectively and must be perpendicular to the flow velocity.

2. Lines ad and bc must be streamlines far away from the body such that the pressure on those lines is equal to the freestream pressure (p_∞).

The Figure 2.7 shows the two-dimensional control volume with the x-axis aligned along the streamwise direction. The above two criteria must be satisfied along all the three directions.

Drag force is aligned along the x-direction (streamwise direction). Considering the conservation of momentum within the control volume $abcd$, the following equation is obtained

$$F_{Drag}(t) = -\rho \oiiint_V \frac{\partial u}{\partial t} dV - \rho \oiint_S (\vec{v}.\vec{n})u \, dS - \oiint_S \left((p\vec{n} - \vec{\tau}.\vec{n})dS\right)_x \tag{2.6}$$

In the Eqn 2.6, V represents the control volume and S represents the control surface (boundary of the control volume) as shown in Figure 2.7. $\vec{n}$ is the outward normal vector on each control surface S. The incoming flow is assumed to be uniform with a velocity V_∞ and pressure p_∞. The outflow velocity profile ($\vec{u}$) is not uniform due to the formation of the wake. ρ is the density of air, $\vec{\tau}$ is the shear (viscous) stress tensor and p is the static pressure.

It is known that the viscous forces are dominant close to the body. Since the one of the criteria for this control volume states that the control surfaces are considered sufficiently far away, the contribution of the viscous terms can be considered negligible in comparison to the other terms [39]. The normal vector $\vec{n}$ is normal to the velocity vector $\vec{v}$ along the boundaries ad and bc. As a result, $(\vec{v}.\vec{n})_{ad,bc} = 0$. Moreover, there is no pressure force ($\iint pdS$) along the streamlines ad and bc. On implementing these conditions on Eq. 2.6, it reduces to the following equation

$$F_{Drag}(t) = -\rho \oiiint_V \frac{\partial u}{\partial t} dV + \rho \left(\oiint_{ab} {V_\infty}^2 \, dS - \oiint_{cd} u^2 \, dS \right) + \left(\oiint_{ab} p_\infty dS - \oiint_{cd} p dS \right) \tag{2.7}$$

From the conservation of mass for the control volume $abcd$, the mass entering the control volume should be equal to the mass leaving the control volume. Hence the following equation is applicable

$$\oiint_{ab} \rho V_\infty \, dS = \oiint_{cd} \rho u \, dS \tag{2.8}$$

Multiplying both sides of equation (2.8) by U_∞, we get

$$\oiint_{ab} \rho {V_\infty}^2 \, dS = \oiint_{cd} \rho u V_\infty \, dS \tag{2.9}$$

Substituting Eqn 2.9 into the Eqn 2.7, the following simplified equation is obtained

$$F_{Drag}(t) = -\rho \oiiint_V \frac{\partial u}{\partial t} dV + \rho \oiint_{wake} (V_\infty - u) u \, dS + \oiint_{wake} (p_\infty - p) dS \tag{2.10}$$

Reynolds decomposition is applied to the velocity and pressure term: $u = \bar{u} + u'$and $p = \bar{p} + p'$, where $\bar{u}$ represents the mean velocity component and u' represents the fluctuating velocity component. Then, the time-averaging is applied to each term in the equation 2.10. The time average of fluctuating terms is always zero by definition and the unsteady term $\frac{\partial u}{\partial t}$ drops out due to time averaging. As a result, the following equation is obtained

$$\bar{F}_{Drag} = \rho \oiint_{wake} (V_\infty - \bar{u}) \bar{u} \, dS - \rho \oiint_{wake} \overline{u'^2} \, dS + \oiint_{wake} (p_\infty - \bar{p}) dS \tag{2.11}$$

The Equation 2.11 represents the equation for time-average drag force. It consists of three terms. The first integral represents the momentum term, the second one represents the Reynolds stress term and the last one represents the pressure term.

Pressure reconstruction

In this study, pressure in the wake of the bobsleigh is reconstructed from the velocity data obtained from PIV measurements. Pressure reconstruction is performed using the methodology described by van Oudheusden [40, 41].

The Navier-Stokes equation is used to estimate the pressure gradient and it reads as follows

$$\nabla p = -\rho \frac{D\vec{v}}{Dt} + \mu \nabla^2 \vec{v} \tag{2.12}$$

In Eq. 2.12, the term $\frac{D\vec{v}}{Dt}$ represents the material derivative and is evaluated as follows

$$\frac{D\vec{v}}{Dt} = \frac{\partial\vec{v}}{\partial t} + (\vec{v}.\nabla)\vec{v} \tag{2.13}$$

Substituting Eq. 2.13 into Eq. 2.12, the following equation is obtained

$$\nabla p = -\rho\left(\frac{\partial\vec{v}}{\partial t} + (\vec{v}.\nabla)\vec{v}\right) + \mu\nabla^2\vec{v} \tag{2.14}$$

Reynolds averaging of Eq. 2.14 results in a time-averaged pressure gradient

$$\nabla\bar{p} = -\rho\left(\bar{\vec{v}}.\nabla\right)\bar{\vec{v}} - \rho\nabla.\left(\overline{\vec{v'}.\vec{v'}}\right) + \mu\nabla^2\bar{\vec{v}} \tag{2.15}$$

van Oudheusden [40, 41] observed that the contribution of the viscous terms to the time-averaged pressure gradient was negligible. On neglecting the viscous terms and taking a divergence on both sides of Eq. 2.15, the following equation is obtained

$$\nabla^2\bar{p} = -\rho\left(\bar{\vec{v}}.\nabla\right)\bar{\vec{v}} - \rho\nabla.\nabla.\left(\overline{\vec{v'}.\vec{v'}}\right) \tag{2.16}$$

Eq. 2.16 represents the Pressure Poisson Equation (PPE). For solving the PPE, there is a requirement of four Boundary conditions (BCs) (one for each of the boundaries of the domain). Specifying the BCs (either Dirichlet or Neumann or a combination of both) on the boundaries of the measurement plane, the PPE is solved numerically on a Cartesian grid to reconstruct the pressure in the entire domain following the methodology given by Hoffmann [42].

The Eqn. 2.16 can be represented as $\bar{p}_{xx} + \bar{p}_{yy} = RHS$. The discretized form of the LHS of this equation can be evaluated at the non-boundary points by using a second order finite difference scheme wherein pressure at each location is computed by using a five point method [42]. This is illustrated in the following equation

$$\nabla^2 p_{i,j} = \frac{1}{\Delta x^2}\left(p_{i+1,j} + p_{i-1,j} + p_{i,j+1} + p_{i,j-1} - 4p_{i,j}\right) = RHS_{i,j} \tag{2.17}$$

In Eqn. 2.17, Δx is the grid spacing and it is assumed equal in both directions. This equation can be written as $ap = RHS$ where p is the matrix containing the pressures in the domain and a is the coefficient matrix known as the Poisson matrix. The evaluation of the elements of RHS are discussed later in section 4.2.

2.5. External force balance

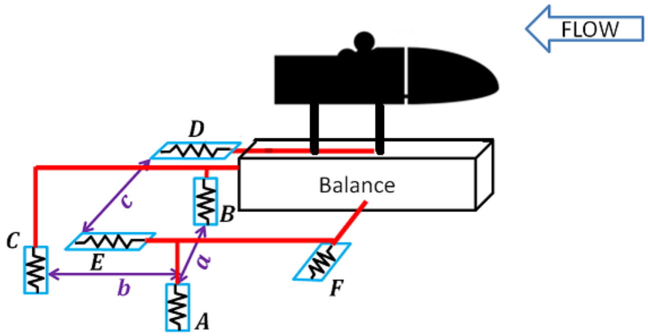

Figure 2.8: Schematic arrangement of strain gauges inside an external force balance with the bobsleigh mounted on the balance [43].

External force balance systems are the most common devices to measure the aerodynamic forces and moments on a test object in a wind tunnel. Usually, the model is mounted on the balance with the help of struts. The balance consists of sensitive electrical elements called the strain gages (shown as A to F in Figure 2.8). As the bobsleigh model mounted on the balance experiences any force in a particular direction, it causes the strain gauges to stretch in that direction. Due to the stretching of the strain gauges, their electrical resistances get altered. Forces can be measured by pre-calibrating the change of the electrical resistances of these strain gages in the respective directions. Moments are measured by using the distance between the two strain gages (a to c). In the above sketch the drag force in the direction of the flow is given by summing the strain gages $D + E$.

3

Experimental Setup

An experimental campaign was conducted on a simplified model of a bobsleigh at the Low Speed Laboratory of Delft University of Technology. This chapter focusses on the wind tunnel experimental facility in Section 3.1 and on the design and specifications of the bobsleigh model in Section 3.2. The stereocopic PIV setup including the equipments used and the quantities measured are discussed in Section 3.3. Finally Section 3.4 deals with the setup of the wind tunnel force balance system and the balance measurements performed.

3.1. Experimental Wind Tunnel Facility

The wind tunnel experiments are performed in the M-tunnel (see Figure 3.1 (left)) of the Low Speed Laboratory (LSL) of the Faculty of Aerospace engineering at Delft University of Technology. This tunnel has two configurations - open jet and closed jet. For this research work, the open jet type is used. The open jet configuration is preferred in order to avoid the large solid blockage that would be imposed by the model due to presence of solid walls in the closed test section. The test section used for this research (see Figure 3.1 (right)) has a square cross section with dimensions 0.4 x 0.4 m^2 and due to the large contraction ratio the turbulence level of the flow in the test section is low. The tunnel operates in the speed range of 2 to 30 m/s.

Figure 3.1: Wind tunnel facility. Delft University of Technology M-tunnel [44] (left) and wind tunnel test set-up (right).

The wind tunnel tests performed in this research focus either on drag measurements from force balance systems or on obtaining velocity field data from stereoscopic PIV measurements for various configurations of the bobsleigh model. The scaled bobsleigh model which is used for the tests is described in detail in the next section.

3.2. Bobsleigh model

The wind tunnel tests are conducted on a simplified 1:5.5 scaled model of a bobsleigh (see Figure 3.2 (left)). The model is been painted black in order to limit the reflections of the laser light during the PIV measurements. The model consists of two parts namely the front cowling (nose) and the rear cowling. The 3D printed front cowling is elliptical in shape but has a circular cross section whereas the rear cowling which is made from PVC tube has a cutout on top which represents the bobsleigh cavity. The front cowling has a length of 200 mm, a diameter of 125 mm and a thickness of 3.75 mm. The rear cowling has a length of 285 mm and the same diameter as that of the front cowling. A threaded rod is used to connect both the parts of the model and it also controls the front cowling rotation by means of a non-centered pivot point. This threaded rod passes through a pipe which is connected to the rear cowling and which keeps the base of the rear cowling structure intact (see Figure 3.2 (right)). The rod is fastened to the rear end of the rear cowling using a wing nut. The crew model which is made of wood is placed in the cowling cavity and it represents the pilot and the brakeman inside the bobsleigh model. Zig-zag strips of 0.5 mm height are applied onto the front cowling at 60 mm from the leading edge to ensure the turbulent regime of the boundary layer.

Figure 3.2: Wind tunnel test model. Test model in the wind tunnel (left) and CAD-model of the bobsleigh (right).

Several bobsleigh configurations are tested in the wind tunnel. Three of these configurations along with their specifications are shown in this section. One of these configurations is the attachment of the vortex generators on the sidewalls of the bobsleigh model. Vortex generators having dimensions $187.5\,mm \times 26\,mm$ are positioned on the outer sidewalls symmetrically on either side at 5 mm from the rear end of the rear cowling as shown in Figure 3.3.

Figure 3.3: Bobsleigh model with vortex generators attached on the sidewalls. Side view (left) and top view (right).

Second important configuration is the ducted nose configuration. The ducts have a cross-sectional area of $700\,mm^2$ each and extend upto three-fourths of the length of the rear cowling as shown in Figure 3.4.

Figure 3.4: Bobsleigh model with ducted nose configuration. Back view (left) and top view (right).

Finally, the bobsleigh configuration with zig-zag strips attached to the side walls is tested. The zig-zag strips of dimensions $230\,mm \times 10\,mm$ are positioned on the outer side walls symmetrically on either side starting from the rear end of the rear cowling as shown in Figure 3.5.

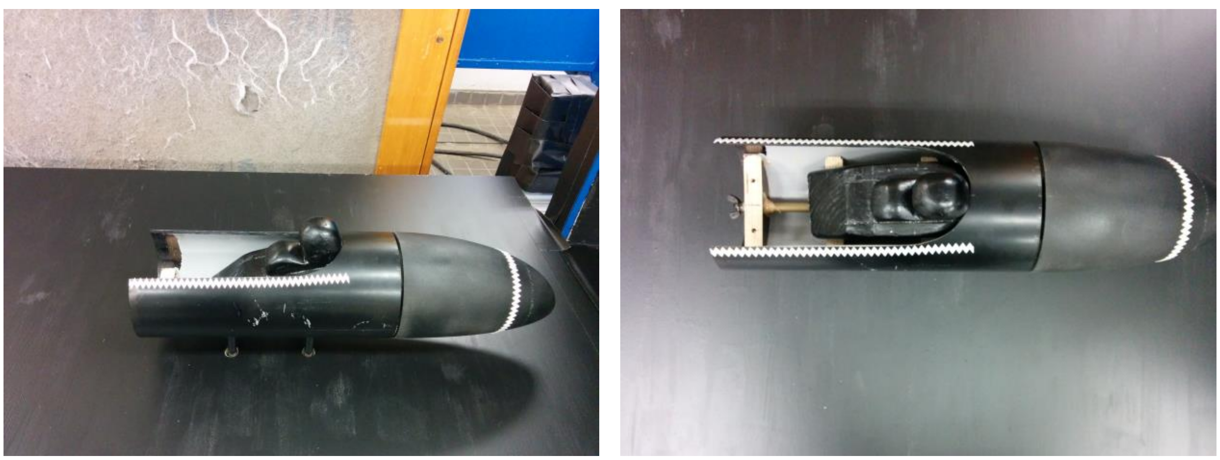

Figure 3.5: Bobsleigh model with zig-zag strips attached to the side walls. Isometric view (left) and top view (right).

3.3. Stereoscopic PIV setup

The stereoscopic PIV setup consists of two CCD cameras, an Nd-YAG laser, a programmable timing unit, a computer with DaVis software for data acquisition and for controlling the sequence of actions and a seeding system for seeding the air-flow with fog particles.

Imaging and illumination

Images are captured by two 2M*pix* Imperx Bobcat IGV-B1610 cameras (CCD, 1628×1236 pixels, 4.4 μm pixel pitch, and 10 bit) in stereoscopic configuration. It is made sure that the cameras are placed sufficiently far downstream in the wake such that they do not affect the flow behaviour. They are placed in the wake of the model, one facing the flow straight and the other at an angle of nearly 35°. The cameras mount Nikon objectives of focal length 35 mm and 50 mm and the lens apertures are set to *f*# = 4 and 5.6 respectively for optimal data collection. The field of view is 32×24 cm^2, yielding a magnification factor of 0.022 and a digital image resolution of 0.20 mm/pixel. A Quantel Evergreen 200 Nd: YAG laser is used with a 200 mJ pulse at a 15 Hz maximum repetition rate. Illumination is provided by a Quantel Evergreen 200 Nd: YAG on a vertical plane behind the model. A laser sheet thickness of around 3 mm and is produced with the help of a combination of spherical and cylindrical lenses. The stereoscopic PIV test setup is shown in Figure 3.6.

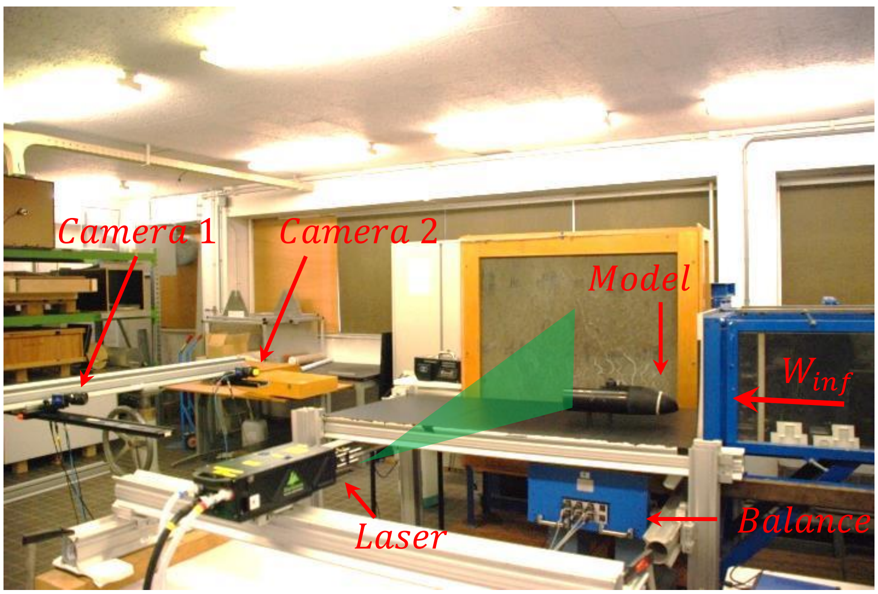

Figure 3.6: Stereoscopic PIV test setup

Seeding

The flow is seeded with micron-sized droplets from a SAFEX smoke generator. The smoke generator is placed such that a jet of fog particles is injected into the wind tunnel inlet. First, the wind tunnel is turned on and then the smoke generator is switched on. The flow is allowed to reach a steady state such that a uniform stream of fog particles is obtained. A freestream velocity of 20 m/s is used for most of the tests in the experiment.

Acquisition

For all the bobsleigh configurations, 500 uncorrelated samples are acquired at an acquisition frequency of 8.33 Hz. The time separation between two laser pulses is calculated to be 50 µs for a freestream velocity of 20 m/s. Measurements are performed at different planes in the wake of the model, namely $z/D = 1$ and 2, z being the streamwise distance from the back of bobsleigh and D the diameter of the bobsleigh. The front cowling is rotated by angles between 0° and 20° towards the left of the model in order to investigate the effect of the front cowling misalignment on the aerodynamic drag. Image acquisition and data analysis are conducted with the LaVision DaVis 8.3 software. Each set of data that is acquired is preprocessed in order to avoid unwanted noise signals due to reflections. The details on pre-processing are further discussed in section 4.1 of the next chapter. Velocity fields are evaluated using a multipass stereoscopic cross-correlation algorithm with final interrogation window of 32×32 pixels and 75% overlap factor. From the velocity fields, the time-averaged pressure fields are reconstructed solving the Poisson equation for pressure and the aerodynamic drag is evaluated invoking the conservation of momentum in a control volume [41]. The method of pressure reconstruction has been dealt with in detail in the section 2.4 of the previous chapter.

3.4. Wind tunnel external balance

The OJF External Balance is a six-component wind tunnel balance designed, manufactured and calibrated at the National Aerospace Laboratory, Netherlands (NLR). The balance measures the three force components *(Fx, Fy, Fz)* and the three moments *(Mx, My, Mz)*. Under simultaneous loading of all six components, the balance is capable of measuring loads up to 250 N in the streamwise direction with a maximum uncertainty of 0.06% [45]. The balance is mounted directly under the ground plate and connected only to the feet of the bobsleigh model without touching the ground plate directly. Balance measurements are conducted at acquisition frequency of 1612 Hz for a time interval of 9.5 seconds. The *Fx* component of the force measures the drag force directly. Before performing balance measurements, the balance is biased (zeroed at no wind speed). In case of any differences, the readings at zero velocity are noted and then subtracted from the final measured value. In order to have comparable drag measurements with stereoscopic PIV results, the balance measurements are acquired in the presence of seeder particles in the flow. Other parameters that are measured include ambient pressure, ambient temperature, streamwise velocity and dynamic pressure. From the balance measurements, two types of output files are obtained. One of them contains mean values over a time interval of 9.5 seconds and the other one contains instantaneously measured force data points over this time interval.

4

Data Reduction and Analysis

This chapter describes the sequence of steps taken to process the acquired PIV data in order to visualize the flow field and estimate the drag force. Section 4.1 describes the necessary pre-processing and processing steps including calibration procedures. Section 4.2 deals with the post processing techniques and visualization tools used in the analysis. Section 4.3 discusses the procedure used to evaluate each term of the drag equation in order to achieve the total drag force from PIV. Section 4.4 investigates the uncertainty quantification related to the aerodynamic drag using the error propagation formula. Finally Section 4.5 deals with the POD analysis of the streamwise velocity fluctuations derived from the PIV measurements.

4.1. PIV processing techniques

4.1.1. Calibration

Figure 4.1: LaVision type 30 calibration plate

The calibration plate (see Figure 4.1) used was a LaVision Type 30 plate [46]. Two types of calibrations are performed using the calibration plate – geometrical calibration and self-calibration. In case of geometrical calibration, the position of each camera is measured with respect to a known set of points on the calibration plate. This calibration is performed so as to combine two-dimensional apparent velocity fields into a single three-dimensional velocity field. Geometrical calibration is performed with the pin-hole model [35]. On the other hand, self-calibration [47] is performed in order to avoid misalignment between the calibration plane and the measurement plane. Every time the position of the cameras or the laser head is changed with respect to the model, a new set of geometrical and self-calibration needs to be performed.

4.1.2. Image pre-processing

The raw images acquired during the PIV measurements are preprocessed by masking reflections formed due to the laser sheet on the ground plate and subsequently subtracting the minimum intensity using a time series filter for each pixel position in order to lower the background noise. The background light intensity after using this operation is less than 10 counts. Low background noise is desirable in order to reduce the uncertainty associated with the PIV measurement. The averaged light intensity of the brightest particles was found to be in the range of 100 to 150 counts.

4.1.3. Velocity field calculation

After the pre-processing of the images, the velocity field is calculated. For velocity calculation the particle image of each camera is subdivided into small interrogation windows. The average particle displacement within an interrogation window is determined by cross-correlation followed by the localization of the correlation peak. Velocity fields are reconstructed on interrogation windows of 64×64 pixels with 75% overlap factor using multipass stereo cross correlation algorithm. From the known time difference Δt and the measured displacement in each direction, the velocity components are calculated [48].

4.1.4. PIV post-processing techniques

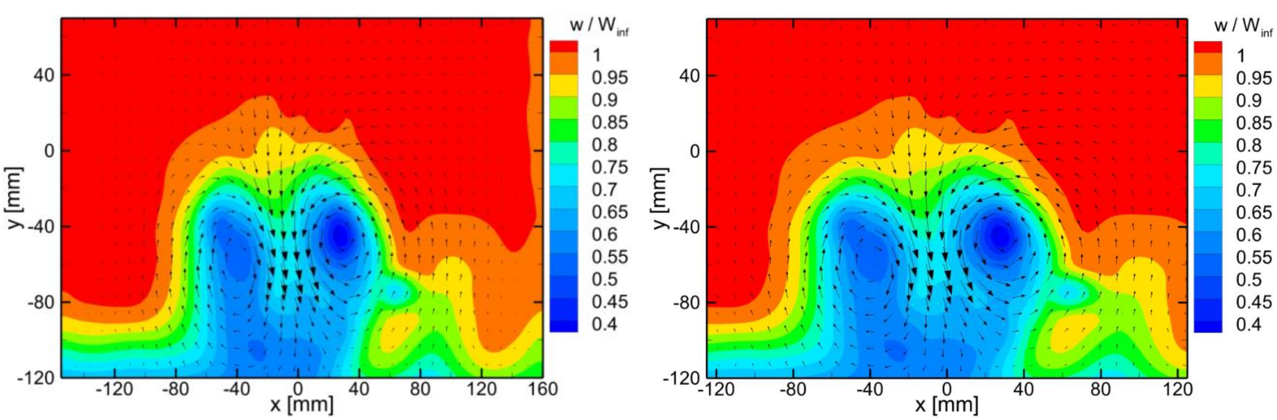

Figure 4.2: Time-averaged velocity field at plane z/D =1 with edge effects (left) and after correcting for edge effects (right)

After calculating the velocity fields, the edge effects that occur due to wrong cross correlation in the presence of spurious intensity values are corrected. This is done by extracting the region of interest by eliminating the edges. The edge effects can be observed in the Figure 4.2-left wherein the right edge contains spurious intensity values corresponding to velocities less than the freestream velocity which is not expected. All the other spurious vectors lying in the region of interest are removed and the empty spaces are replaced by interpolation during vector post processing. A median filter is used as well in order to eliminate particle data that lie outside local limits. Thus the entire interrogation window is divided into several regions and the filter is implemented on each region in order to filter out particles whose velocity information lies outside limits. Another post processing technique that is used is the proper orthogonal decomposition analysis (POD analysis) is explained in detail in section 4.4.

After post-processing the velocity data, the time-averaged pressure fields are reconstructed by solving the Poisson equation for pressure with appropriate boundary conditions and then the aerodynamic drag is evaluated invoking the conservation of momentum in a control volume [41]. The methodology of pressure field reconstruction from PIV data is discussed in section 2.4 and the details of pressure field computation are dealt in section 4.2 (sub-section 4.2.3). The evaluation of aerodynamic drag is outlined in the following section of the chapter.

4.2. Drag computation using control volume approach

The drag computation from PIV data for an arbitrary body in relative motion with respect to a surrounding fluid is performed by using a control volume approach which has been developed by Oudheusden et.al [40]. In this approach, the time-averaged drag force is evaluated from a velocity data obtained from uncorrelated PIV acquisitions. For the estimation of time averaged drag force, a mean velocity field and a mean pressure field in the wake of the object is to be determined. Thus, all the terms in the drag equation (Eq. 4.1) are evaluated and combined in an attempt to predict the drag force with utmost accuracy.

$$\bar{F}_{Drag} = \rho \iint_{S_{wake}} (W_\infty - \bar{w})\bar{w} \; dS - \rho \iint_{S_{wake}} \overline{w'^2} \; dS + \iint_{S_{wake}} (p_\infty - \bar{p}) \; dS \tag{4.1}$$

In the Eq. 4.1 the over-bar indicates the time average operation. $W = \bar{w} + w'$, W is the instantaneous velocity, $\bar{w}$ is the time-averaged streamwise velocity obtained by averaging the streamwise velocities from different uncorrelated PIV samples, w' is the fluctuating component of the streamwise velocity and is obtained from $w' = w - \bar{w}$. W_∞ is the freestream velocity; ρ is the density of air and p_∞ is the static pressure in the freestream, $\bar{p}$ is the time-averaged pressure in the measurement volume.

From the drag equation (Eq. 4.1), it can be seen that the time averaged drag evaluation consists of three integrals computed over a surface downstream of the object. The viscous terms in this computation are neglected as the drag measurement is on a surface that is located sufficiently far from the model. The first integral in the equation represents the momentum term, the second one represents the Reynolds stress term and the third one is the pressure term. These integrals are discussed in detail in the following subsections.

4.2.1. Momentum term

The first integral in the Eq. 4.1 represents the momentum term. It is a measure of the momentum deficit in the wake of an object along the streamwise direction as relative to the incoming momentum upstream of that object. It is obtained from the time-averaged velocity field in the wake of the object. The air density ($\rho = 1.225 kg/m^3$) is assumed to be constant throughout the entire experiment. The freestream velocity W_∞ is considered as the velocity that is set at the wind tunnel. However the time-averaged velocities measured at the boundaries of the measurement planes in PIV measurements differ slightly from the wind velocity set at the tunnel exit. This difference could be due to a combination of factors. The expansion of the air stream on leaving the tunnel exit could result in a different freestream velocity at the measurement plane. The measurement uncertainties of PIV could also lead to differences in freestream velocity.

As a first approximation to bridge the difference in the freestream velocity, a mean of the streamwise velocities obtained from the top and side boundaries of the measurement plane is computed. This estimate may not be sufficient and hence freestream velocity corrections should be applied.

Freestream corrections for incoming flow

The presence of a bluff object can cause large distortions of the incoming flow leading to changes in the drag measurements at the body. For the evaluation of drag by control volume approach, two velocity measurements are required - one velocity measurement at the incoming plane (W_∞) and the other at the outflowing plane ($\overline{w}$). Ideally the incoming velocity is assumed to be equal to the outflowing velocity in case of closed test sections and for models which offer very less solid blockage. However, this is not true in case of open test sections where the jet flowing out of the test section exit expands into an open chamber. As a result, the flow velocity reduces. The velocity perceived at the measurement plane is lower than the actual freestream value. These effects are further enhanced in the presence of bluff objects, and lead to large deviations in the loads measured by the control volume method. In order to reduce these deviations, Mercker and Wiedemann [49] have suggested corrections to account for the expansion of the jet and nozzle blockage that typically occurs in Open-Jet wind tunnels.

There are four primary effects associated with open jet wind tunnels [50] that need correction. Out of them the two that are applicable in this case are Jet Expansion and the Nozzle Blockage corrections. As the measurement plane is sufficiently far from the center of the model ($L_{ts} - x_m$, see Figure 4.3), other interference effects such as the Collector Blockage and Empty-Tunnel Pressure Gradients are assumed to be negligible.

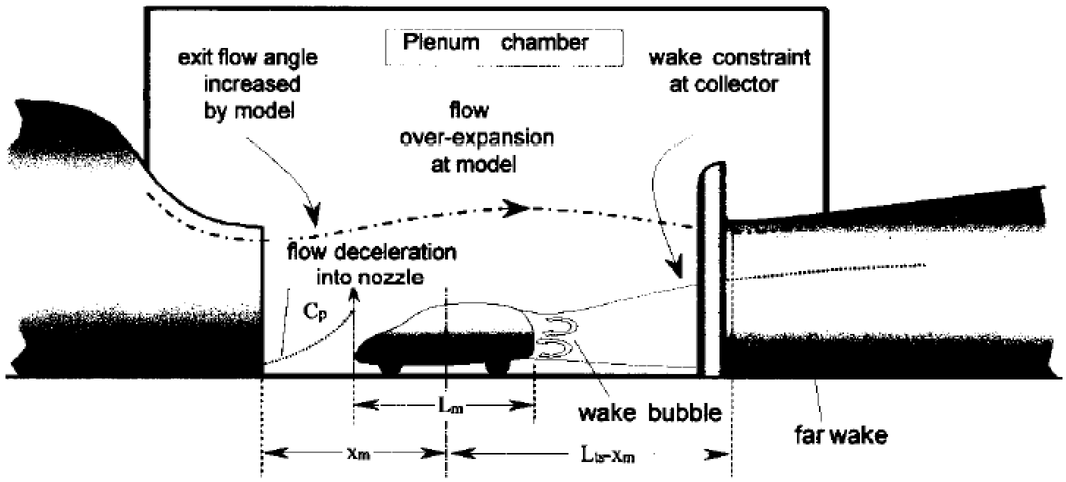

Figure 4.3: Schematic of flow over a model in an Open-Jet Wind Tunnel. Adapted from Agardograph 336 [50].

(a) Nozzle blockage

Presence of the bluff model in close proximity to the nozzle exit plane decreases the effective nozzle exit area causing an increase in the flow velocity at the periphery of the jet. The presence of high pressure region upstream of the model causes an increase in the exit flow angle further enhancing the jet expansion effects. This effect increases as the model moves closer to the nozzle. The correction factor for the nozzle blockage corrections is given as:

$$\epsilon_N = \frac{\epsilon_{qn} {R_N}^3}{\left({R_N}^2 + {x_m}^2\right)^{3/2}} \tag{4.2}$$

(b) Jet expansion

Due to the pressure difference between the flow exiting the nozzle and the stagnant air surrounding the test section, there is a jet expansion outwards as shown in Figure 4.3. This causes an increase in the flow cross-section as the flow moves downstream over and beyond the model. Thus the flow decelerates following the flow continuity equation. Thus, the flow upstream to the model is corrected according to the correction factor:

$$\epsilon_s = \tau \sqrt{\frac{V_m}{L_m}} \left(\frac{A_m}{A^{*3/2}}\right) \tag{4.3}$$

where $\tau = -0.211$ is the tunnel shape factor for a square tunnel cross section obtained from Agardograph 109 [51]. V_m, A_m, L_m are the model volume, frontal area and the length respectively. A^* is the effective nozzle area given by:

$$A^* = \frac{A_N}{\left(1 + \epsilon_{qn}\right)} \tag{4.4}$$

Here, A_N is the nozzle exit area and ϵ_{qn} is the nozzle blockage factor given by:

$$\epsilon_{qn} = \frac{A_m}{2A_N}\left(\frac{1 - x_s}{\sqrt{{x_s}^2 + {R_N}^2}}\right) \tag{4.5}$$

The two terms x_s and R_N are evaluated as follows:

$$x_s = \frac{x_m + L_m}{2 + \sqrt{\frac{A_m}{2\pi}}}, \quad R_N = \sqrt{\frac{2A_N}{\pi}} \tag{4.6}$$

Table 4.1 shows all the parameters used for the corrections of the freestream velocities in this study.

The time-averaged freestream velocity $W_{\infty,PIV}$ measured on the PIV measurement plane is then corrected to obtain the incoming freestream velocity W_∞ on plane as follows:

$$\left(\frac{W_\infty}{W_{\infty,PIV}}\right) = 1 + \epsilon_s + \epsilon_N \tag{4.7}$$

Correction Parameters			
τ	-0.211	A^*	$0.1523\ m^2$
L_m	$0.485\ m$	x_s	$0.4042\ m$
A_m	$0.0139\ m^2$	R_N	$0.3191\ m$
V_m	$0.00673\ m^3$	ϵ_{qn}	0.0502
A_N	$0.16\ m^2$	ϵ_s	-0.005805
x_m	$0.3425\ m$	ϵ_N	0.0159
$\left(\frac{W_\infty}{W_{\infty,PIV}}\right)$	1.010095		

Table 4.1: Parameters for freestream velocity corrections for 0° front cowling rotation case

4.2.2. Reynolds stress term

The Reynolds stresses are a part of the total stress in a fluid and they give an indication of the rate of mean momentum transfer by turbulent fluctuations. The Reynolds stresses are obtained by applying Reynolds decomposition to the Navier Stokes equations as well as to the continuity equation followed by time averaging of these equations. The non-linear convective terms obtained from these equations after performing such an operation are primarily responsible for the Reynolds stresses [52]. The evaluation of these stresses makes use of the fluctuating part of each velocity component. As the operation is performed on a set of uncorrelated samples (N samples), Reynolds stresses are obtained and evaluated according to the following equations:

$$RS_{xx} = \frac{1}{N}\sum_{1}^{N}\overline{u'^2}, \qquad RS_{yy} = \frac{1}{N}\sum_{1}^{N}\overline{v'^2} \qquad RS_{zz} = \frac{1}{N}\sum_{1}^{N}\overline{w'^2} \tag{4.8}$$

$$RS_{xy} = \frac{1}{N}\sum_{1}^{N}\overline{u'v'}, \qquad RS_{xz} = \frac{1}{N}\sum_{1}^{N}\overline{u'w'} \qquad RS_{yz} = \frac{1}{N}\sum_{1}^{N}\overline{v'w'} \tag{4.9}$$

In the above equations, the terms inside the summations are obtained as follows:

$$\overline{u'^2} = \frac{1}{N}\sum_{1}^{N}u'^2, \qquad \overline{v'^2} = \frac{1}{N}\sum_{1}^{N}v'^2, \qquad \overline{w'^2} = \frac{1}{N}\sum_{1}^{N}w'^2 \tag{4.10}$$

where $u' = u - \bar{u}, \quad v' = v - \bar{v}, \quad w' = w - \bar{w}$

From the equation 4.1, it is observed that the drag computation is only dependent on the normal Reynolds stress term (RS_{zz}) in the streamwise direction. Thus this term is evaluated for each point in the measurement plane and summed up to obtain the total Reynolds stress integral in the drag equation. From equation 4.1, it can be noted that this term contributes negatively to the aerodynamic drag.

4.2.3. Pressure term

The last integral in equation 4.1 represents the pressure term. The evaluation depends upon the difference between freestream pressure and the mean pressure field obtained at each point in the measurement plane located in the wake. The mean pressure field in the wake is reconstructed from the velocity field obtained from PIV measurements using the methodology provided by van Oudheusden [41]. This methodology is discussed in this sub-section and the mean pressures are obtained.

Pressure determination methodology

The mean-pressure gradient is obtained from Reynolds averaging of the momentum equation, as indicated by the overbar

$$\nabla\bar{p} = -\rho(\bar{V}.\nabla)\bar{V} - \rho\nabla.(\overline{V'V'}) + \mu\nabla^2\bar{V} \tag{4.11}$$

In equation 4.11, $\bar{V} = \{\bar{u} \;\; \bar{v}\}\, and\, V' = \{u' \;\; v'\}$. The viscous terms in this equation could also be neglected owing to a high value of Reynolds number (Murai et. al. [53]). In this process, only the in-plane pressure gradients are evaluated. Even though the flow is highly three dimensional, the pressures are computed only along a plane. Hence the out of plane pressure gradients can be neglected. After applying these assumptions and expressing the equation 4.11 in Cartesian coordinates, the following equations are obtained

$$\frac{\partial \bar{p}}{\partial x} = -\rho\left\{\bar{u}\frac{\partial \bar{u}}{\partial x} + \bar{v}\frac{\partial \bar{u}}{\partial y} + \frac{\partial \overline{u'^2}}{\partial x} + \frac{\partial \overline{u'v'}}{\partial y}\right\} \tag{4.12}$$

$$\frac{\partial \bar{p}}{\partial y} = -\rho\left\{\bar{u}\frac{\partial \bar{v}}{\partial x} + \bar{v}\frac{\partial \bar{v}}{\partial y} + \frac{\partial \overline{v'^2}}{\partial y} + \frac{\partial \overline{u'v'}}{\partial x}\right\} \tag{4.13}$$

Equations 4.12 and 4.13 suggest that the time-averaged pressure gradients can be obtained from time-averaged velocity fields, velocity gradients and the gradients of the Reynolds stresses. The gradients are computed using a finite central difference scheme on the generated Cartesian grid of the measurement plane according to the following equations:

$$\frac{\partial \bar{V}}{\partial x} = \frac{\overline{V_{\imath+1,\jmath}} - \overline{V_{\imath-1,\jmath}}}{2\Delta x} \tag{4.14}$$

$$\frac{\partial \bar{V}}{\partial y} = \frac{\overline{V_{\imath,\jmath+1}} - \overline{V_{\imath,\jmath-1}}}{2\Delta y} \tag{4.15}$$

where $\bar{V} = \{\bar{u} \quad \bar{v}\}$, i and j represent the indices of the points in the measurement plane in the x and y directions respectively. Δx and Δy is the spacing between the vectors in the x and y directions. The gradients of the Reynolds stresses are also obtained by a similar method.

After the determination of pressure gradients from equations 4.12 and 4.13, the Poisson equation for pressure is obtained by taking the divergence of the steady momentum equation (Eqn 4.11).

$$\nabla^2 \bar{p} = -\rho\nabla.(\bar{V}.\nabla)\bar{V} - \rho\nabla.\nabla.(\overline{V'V'}) \tag{4.16}$$

The above Poisson equation (eqn 4.16) can be written as a linear equation in $\bar{p}$ given by $A\bar{p} = f$. The pressure gradients that are evaluated by Equations 4.12 and 4.13 are inputted to the Poisson solver algorithm which solves this linear equation iteratively. 'A' represents the Laplace operator and f represents the source term. For solving this equation, appropriate boundary conditions are needed.

The boundary conditions are specified by using known values of pressure and pressure gradients for the boundary points in the domain. The boundary conditions used in this study are given in Table 4.2. The implementation of these boundary conditions is illustrated in Figure 4.4.

Boundary conditions		
Bottom boundary	Neumann	$\frac{dp}{dy} = 0$
Top boundary	Dirichlet	$\bar{p} = p_\infty$
Left boundary	Dirichlet + Neumann	$\frac{dp}{dy} = m, \frac{dp}{dx} = n,$ $p = p_\infty$
Right boundary	Dirichlet + Neumann	$\frac{dp}{dy} = m, \frac{dp}{dx} = n,$ $p = p_\infty$

Table 4.2: Specifications of pressure boundary conditions

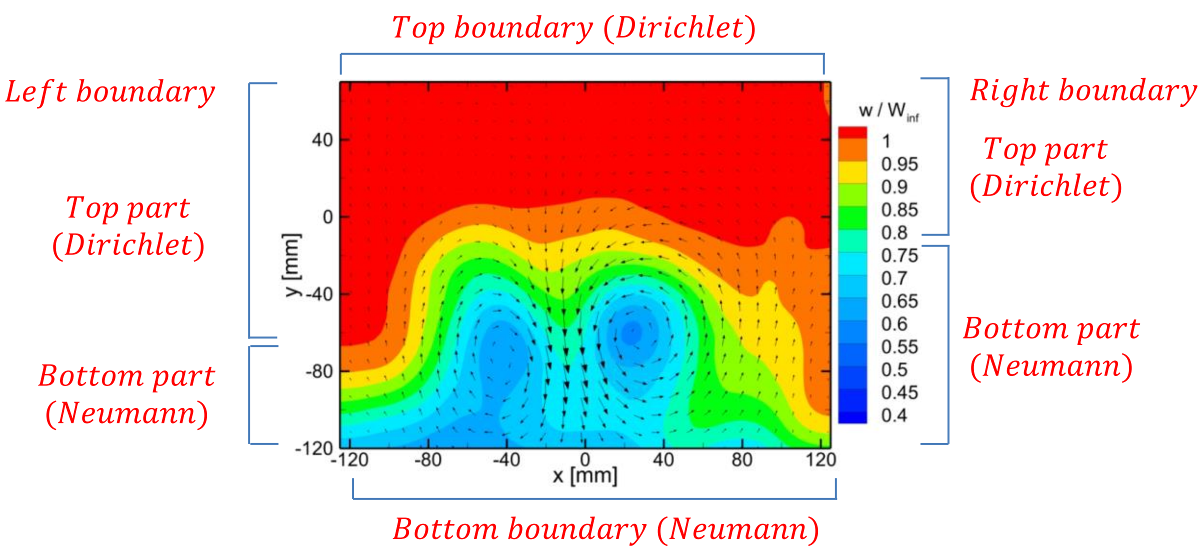

Figure 4.4: Boundary conditions applied to the time-averaged velocity field at a plane z/D = 2.

During the implementation of these boundary conditions, it is assumed that the non-bounded top boundary is at freestream conditions (p_∞ being the freestream pressure). Neumann boundary condition is used for wall-bounded bottom boundary. This is because of the fact that the normal (vertical) velocity component at the bottom boundary vanishes (impermeable wall) and further the gradients of the vertical velocity in the plane of the bottom wall are zero. The RHS of the steady state momentum equation in the y-direction (neglecting viscous terms due to high Reynolds number) results in a zero normal pressure gradient. This can be seen in the following equation

$$\frac{\partial p}{\partial y} = -\rho \left\{ u \underbrace{\cancel{\frac{\partial v}{\partial x}}}_{0} + \underbrace{\cancel{v}}_{0} \frac{\partial v}{\partial y} + w \underbrace{\cancel{\frac{\partial v}{\partial z}}}_{0} \right\} \tag{4.17}$$

The wake formed in the measurement plane extends from the center of the plane till the bottom portion of both left and right boundaries (from y = -65 till y = -120 on the left boundary and from y = -20 till the bottom on the right boundary in Figure 4.4). As a result, freestream conditions cannot be assumed on the entire boundary on either side. A combination of Dirichlet and Neumann conditions is applied to either of the side boundaries. Both these boundaries are partitioned into two parts – top and the bottom parts. The top part of both the side boundaries (from y = -65 till y = 70 for the left boundary and from y = -20 to y = 70 for the right boundary in Figure 4.4) is assumed to have Dirichlet boundary conditions whereas the Neumann boundary conditions are assigned to the bottom parts (from y = -65 till y = -120 for the left boundary and from y = -20 to y = -120 for the right boundary in Figure 4.4). Freestream pressure (p_∞) is assumed on the top part of both the left and right boundaries. The pressure gradients at the boundary points on the bottom part of the left and right boundaries are determined using values of velocities and velocity gradients of their immediate neighboring points by using forward and backward differencing scheme respectively. This can be seen in the following equations

$$\left.\frac{\partial p}{\partial y}\right|_b = -\rho\left\{u_b\left.\frac{\partial v}{\partial x}\right|_b + v_b\left.\frac{\partial v}{\partial y}\right|_b + w_b\left.\frac{\partial v}{\partial z}\right|_b\right\} = m \tag{4.18}$$

$$\left.\frac{\partial p}{\partial x}\right|_b = -\rho\left\{u_b\left.\frac{\partial u}{\partial x}\right|_b + v_b\left.\frac{\partial u}{\partial y}\right|_b + w_b\left.\frac{\partial u}{\partial z}\right|_b\right\} = n \tag{4.19}$$

The subscript 'b' indicates that the particular quantity is evaluated at the boundary point. In the equations 4.18 and 4.19, the derivative w.r.t z is zero as there is no variation of any of the velocity components in the z-direction. The linear equation $A\bar{p} = RHS$ is solved along with appropriate boundary conditions in order to determine $\bar{p}$ by the Poisson solver algorithm. As a result, mean pressure field is obtained. Thereafter, the pressure term is evaluated.

4.3. Uncertainty quantification of drag

PIV measurements are conducted to investigate flow properties derived from the velocity field. Uncertainty quantification in PIV is important in order to determine an interval that contains the error of the measurement technique. After the determination of the instantaneous flow field, the uncertainties related to the velocity components are determined using the equation 4.27. Once the uncertainties associated with these velocity components are estimated, they need to be propagated into the derived quantities of interest. This section discusses the propagation of the instantaneous uncertainty of PIV measurements to the average drag derived from the velocity field. It must be noted that uncertainty quantification of the derived quantities like drag is affected by a couple of factors. First of all, it could be influenced by any kind of correlation between velocity components in time and/or space. Secondly, the uncertainty related to statistical quantities like Reynolds stresses or average drag are affected by the finite sample size [54].

From Eqn 4.1, it is clear that the average drag is a combination of the three terms. Thus, average drag is expressed as a function of the mean streamwise velocity, the

Reynolds normal stress in the streamwise direction and the mean pressure in the following equation

$$\bar{F}_{Drag} = F\left(\bar{w}, \overline{w'^2}, \bar{p}\right) \quad (4.20)$$

Hence the uncertainty associated with the average drag will depend on the uncertainty of each of the three variables in Eqn 4.20. Using the uncertainty propagation formula, the uncertainty of the average drag can be evaluated by the following equation [55]:

$$U_y^{\ 2} = \sum_{i=1}^{N}\left(\frac{\partial F}{\partial x_i}\right)^2 U_{x_i}^{\ 2} + 2\sum_{i=1}^{N-1}\sum_{j=i+1}^{N}\frac{\partial F}{\partial x_i}\frac{\partial F}{\partial x_j}\rho\left(\delta x_i, \delta x_j\right)U_{x_i}U_{x_j} \quad (4.21)$$

where $y = \bar{F}_{Drag}$, $N = 3$, $x_i = \left\{\bar{w}, \overline{w'^2}, \bar{p}\right\}$, $x_j = \left\{\bar{w}, \overline{w'^2}, \bar{p}\right\}$, $(\delta x_i, \delta x_j)$ = errors of (x_i, x_j), $\rho\left(\delta x_i, \delta x_j\right)$ = Cross-correlation coefficient between δx_i *and* δx_j, U_{x_i} represents the uncertainty of variable x_i and F represents the RHS of Eqn 4.1.

In this study, it is assumed that the variables under consideration are not correlated to each other. As a result, cross-correlation coefficient would be zero. Thus, the equation 4.21 reduces to the following equation

$$U_y^{\ 2} = \sum_{i=1}^{N}\left(\frac{\partial F}{\partial x_i}\right)^2 U_{x_i}^{\ 2} \quad (4.22)$$

Substituting the appropriate variables for the different notations in equation 4.16 and expanding the summation, the equation can be rewritten as follows

$$U_{\bar{D}}^{\ 2} = \left(\frac{\partial F}{\partial \bar{w}}\right)^2 U_{\bar{w}}^{\ 2} + \left(\frac{\partial F}{\partial\, \overline{w'^2}}\right)^2 \left(U_{\overline{w'^2}}\right)^2 + \left(\frac{\partial F}{\partial \bar{p}}\right)^2 U_{\bar{p}}^{\ 2} \quad (4.23)$$

The derivative of F with respect to each of the variables is obtained directly by differentiating Eqn 4.1 and are represented by the following equations

$$\left(\frac{\partial F}{\partial \bar{w}}\right) = \rho \iint_{S_{wake}} \left(W_\infty - 2\bar{w}\right)\, dS \quad (4.24)$$

$$\left(\frac{\partial F}{\partial\, \overline{w'^2}}\right) = -\rho \iint_{S_{wake}} 1\ dS \quad (4.25)$$

$$\left(\frac{\partial F}{\partial \bar{p}}\right) = \iint_{S_{wake}} -1\ dS \quad (4.26)$$

The RHS of eqn 4.23 also depends on the uncertainties of mean streamwise velocity, Reynolds normal stress and mean pressure. The method of evaluation of these uncertainties is discussed separately in the following subsections. The derivative of drag with respect to the time-averaged streamwise velocity (in Equation 4.24) depends upon the magnitude of freestream velocity, the magnitude of time-averaged velocity in the wake and also on the area of the measurement plane. However, the derivatives of drag with respect to Reynolds normal stress and mean pressure depend only on the area of the measurement plane and are independent of the freestream and wake velocities.

4.3.1. Uncertainty of mean streamwise velocity

Assuming that the samples are independent and follow a normal distribution of standard deviation σ_w, the standard uncertainty of the mean streamwise velocity is [56]:

$$U_{\overline{w}} = \frac{\sigma_w}{\sqrt{N}} \tag{4.27}$$

In the Eqn 4.27, σ_w represents the standard deviation of the streamwise velocity and it can be obtained directly from PIV measurements. $'N'$ represents the number of uncorrelated PIV samples collected during the measurement.

4.3.2. Uncertainty of Reynolds normal stress

The Reynolds normal stress for the streamwise velocity component w is defined as the variance of w and represented by the following equation [54]:

$$R_{ww} = \overline{w'^2} = \sigma_w{}^2 = \frac{1}{N-1}\sum_{i=1}^{N}(w_i - \overline{w})^2 \tag{4.28}$$

where w' is the fluctuating part of the streamwise velocity w and $w' = w - \overline{w}$.

The standard uncertainty of variance of N samples that are independent and follow a normal distribution of standard deviation σ_w, is evaluated as follows [56]:

$$U_{\sigma_w{}^2} = \sigma_w{}^2\sqrt{\frac{2}{N-1}} \tag{4.29}$$

Using this definition of the Reynolds normal stress in Eqn 4.28 and that of uncertainty of variance in Eqn 4.29, the uncertainty of Reynolds normal stress can be evaluated as follows

$$\left(U_{\overline{w'^2}}\right) = U_{\sigma_w{}^2} = \sigma_w{}^2\sqrt{\frac{2}{N-1}} \cong \sigma_w{}^2\sqrt{\frac{2}{N}} \tag{4.30}$$

In the equation 4.30, the square of the standard deviation can be obtained directly from the PIV measurements.

4.3.3. Uncertainty of time-averaged pressure

The reconstruction of pressure from PIV data in turbulent flows is quite challenging due to the small magnitude of pressure fluctuations [57, 58]. The uncertainty of static pressure is affected by several factors. Some of these factors include uncertainty of the velocity data, spatial and temporal resolutions of the PIV data and boundary conditions used for the evaluation of pressure [41]. The standard uncertainty of reconstructed average pressure is evaluated by applying linear uncertainty propagation formula along the Poisson's equation and it is represented as follows

$$U_{\bar{p}} = \frac{\rho d}{\sqrt{12}}\sqrt{\left[2(U_{\bar{V}})^2\left(\left(\frac{\partial \bar{u}}{\partial x}\right)^2 + \left(\frac{\partial \bar{v}}{\partial y}\right)^2 + \left(\frac{\partial \bar{u}}{\partial y}\right)^2 + \left(\frac{\partial \bar{v}}{\partial x}\right)^2\right)\right] + \left[\frac{12}{d^2}\left(U_{\overline{V'^2}}\right)^2\right] + \left[\frac{1}{d^2}\left(U_{\overline{u'v'}}\right)^2\right]} \quad (4.31)$$

where 'd' represents the grid spacing and 'ρ' represents the density of the fluid used for PIV measurements. The Eqn. 4.31 is derived based on certain assumptions which can be listed as follows:

(a) In this approach, it is assumed that all the mean velocity components have the same uncertainty $U_{\bar{V}}$, all the Reynolds normal stress components have the same uncertainty $U_{\overline{V'^2}}$ and all the Reynolds shear stress components have the same uncertainty $U_{\overline{u'v'}}$ at all points on the grid of the measurement plane.

(b) The errors of all the components of mean velocity are uncorrelated.

(c) Equation 4.31 is the uncertainty in solving the Poisson's equation and it does not account for the uncertainty in boundary conditions.

In order to derive the Eqn. 4.31, each term on the LHS of the Poisson's equation at a particular point on the grid is expressed in terms of mean pressure at that point using the central differencing scheme. Similarly, each term on the RHS of the equation is expressed in terms of either mean velocity or Reynolds stress depending on the term. The uncertainties of each of the terms of the equation is expressed in terms of the uncertainties of known quantities like mean pressure, mean velocity and Reynolds stresses. Finally the linear uncertainty propagation formula is applied to obtain the equation for the uncertainty of mean pressure. The complete derivation of the time-averaged pressure is shown in Appendix A.

4.4. Proper Orthogonal Decomposition

Proper Orthogonal Decomposition (POD) is a powerful method of data analysis aimed at identifying the behaviour and properties of large-scale turbulent structures and separating them from the less coherent turbulent fluctuations.

Data analysis using the POD is often conducted by decomposition of statistical fluctuations in order to extract 'mode shapes' or basis functions from experimental data of high-dimensional systems [59]. POD is helpful in understanding how the different properties of the large-scale turbulent flow structures are distributed among the different modes. In this study, the POD analysis is performed in order to understand the motion and behaviour of the flow structures formed in the near wake of a scaled bobsleigh model.

Mathematical procedure of POD analysis

In this study, the POD analysis is carried out using the method of snapshots. The input data for POD consists of k two dimensional velocity fields (snapshots) sampled in time $V^{(k)} = (u,v)_{i,j}^{(k)}$. Here i,j are the indices of the grid points in the measurement plane and k is the snapshot index. These velocity distributions are decomposed into a linear combination of M spatial basis functions (POD modes,φ_m) and corresponding time coefficients ($c_m^{(k)}$).

$$V^{(k)} = \sum_{m=1}^{M} c_m^{(k)} \varphi_m \tag{4.32}$$

where m represents the mode index and M represents the total number of modes. The total number of modes is equal to the total number of snapshots. In equation 4.32, V is a function of space and time (x, y and t) and c_m is a function of time (t). The basis functions φ_m are orthonormal to each other and these functions are a function of spatial coordinates (x and y). The time coefficients represent the amplitude that the corresponding basis function contributes to a particular snapshot (mode).

The u velocity of every single velocity distribution $V^{(k)}$ is entered into a row and put into a matrix.

$$U = \begin{bmatrix} U^{(1)} \\ U^{(2)} \\ \vdots \\ U^{(K)} \end{bmatrix} = \begin{bmatrix} u_{i=1,j=1}^{(1)} & u_{i=1,j=2}^{(1)} & \dots & u_{i=1,j=J}^{(1)} & u_{i=2,j=1}^{(1)} & \cdots & u_{i=I,j=J}^{(1)} \\ u_{i=1,j=1}^{(2)} & u_{i=1,j=2}^{(2)} & \dots & u_{i=1,j=J}^{(2)} & u_{i=2,j=1}^{(2)} & \cdots & u_{i=I,j=J}^{(2)} \\ \cdots & \cdots & \cdots & \cdots & \cdots & \cdots & z\cdots \\ u_{i=1,j=1}^{(K)} & u_{i=1,j=2}^{(K)} & \dots & u_{i=1,j=J}^{(K)} & u_{i=2,j=1}^{(K)} & \cdots & u_{i=I,j=J}^{(K)} \end{bmatrix} \tag{4.33}$$

where I × J is the number of total grid points in the velocity field and K is the total number of snapshots. The v component is processed in the same way as the u component.

The spatial correlation matrix for velocity distributions is defined as

$$C = \frac{1}{K}(UU^T + VV^T) \tag{4.34}$$

The basis functions are obtained by solving the eigenvalue problem of the correlation matrix

$$C\varphi_m = \lambda_m \varphi_m \tag{4.35}$$

In the eqn. 4.35, φ_m represents the matrix containing the eigenvector and λ_m matrix of eigenvalues. The basis functions φ_m represent the coherent flow structures that are observed in the flow. Each POD mode represents a component of the flow field, which can be reconstructed as a linear combination of all the POD modes.

5

Results and Discussion

This chapter presents the wind tunnel test results obtained from the stereoscopic PIV as well as balance measurements. Several processing operations and data reduction techniques are applied to the raw data obtained from the measurements as described in Chapter 4 and time-averaged results are obtained. These results are analyzed in detail and further interpreted.

Section 5.1 thoroughly analyzes the flow structures in the near wake of the bobsleigh model. It discusses the effects of varying the nose shape and nose rotation angle, as well as the effect of introduction of passive flow control devices on the time averaged velocity and the vorticity fields. Secondly the pressure field is evaluated from the three-dimensional velocity fields and presented in sections 5.2. The velocity fluctuations in the flow field are determined and few interesting cases are compared and presented in section 5.3. The contributions of several terms for the determination of the aerodynamic drag along with the uncertainties of those terms are presented in section 5.4. A comparison between the drag forces obtained from the PIV measurements and the balance measurements is also made in section 5.4. The aerodynamic drag is then compared between different nose shapes in the presence of different passive flow control devices and the results of the comparison are presented. Finally section 5.5 presents the results of the POD analysis performed.

5.1. Near wake mean flow topology

5.1.1. Variation of mean flow topology with measurement plane location

The near wake of the bobsleigh model at $z/D = 1$ shows a large momentum deficit downstream of the model and the formation of two counter-rotating vortices. The latter are due to the rotation of the flow from the sides of the bobsleigh surface towards the inside of the rear cowling. Between the two vortices, a clear downwash is visible at the plane of symmetry of the model (see Figure 5.1-left). The two vortices are symmetrical with respect to the symmetry plane and have approximately the same intensity (see Figure 5.1-right). Further downstream ($z/D = 2$, Figure 5.2), the two vortices are still visible and maintain their symmetry with respect to the symmetry plane of the model. However, the peak vorticity reduces by about 30% with respect to the $z/D = 1$ plane. As a result of the turbulent diffusion of the flow structures, the wake becomes broader and higher streamwise velocities in the wake are encountered.

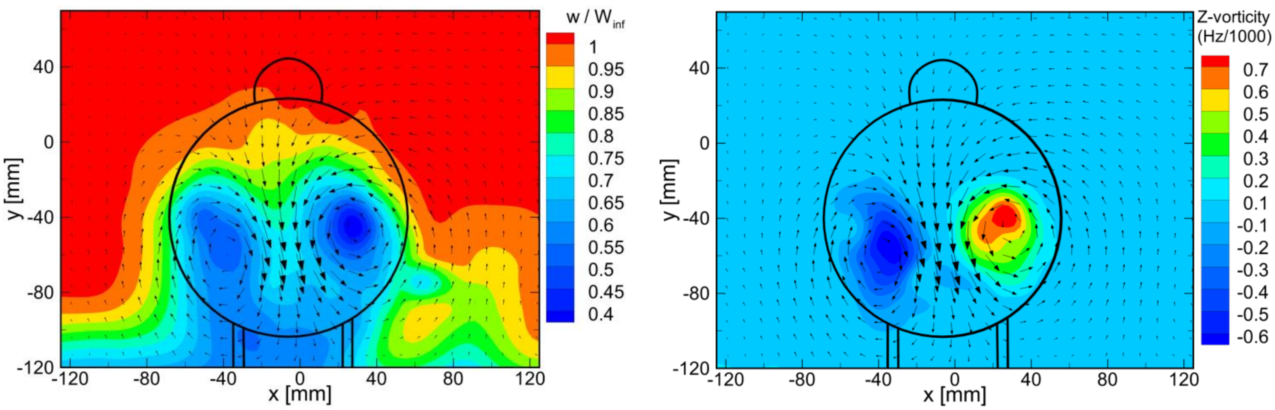

Figure 5.1: Time-averaged velocity (left) and vorticity (right) fields at plane z/D =1. For sake of clarity, one every three vectors is shown both in the x- and in the y-direction.

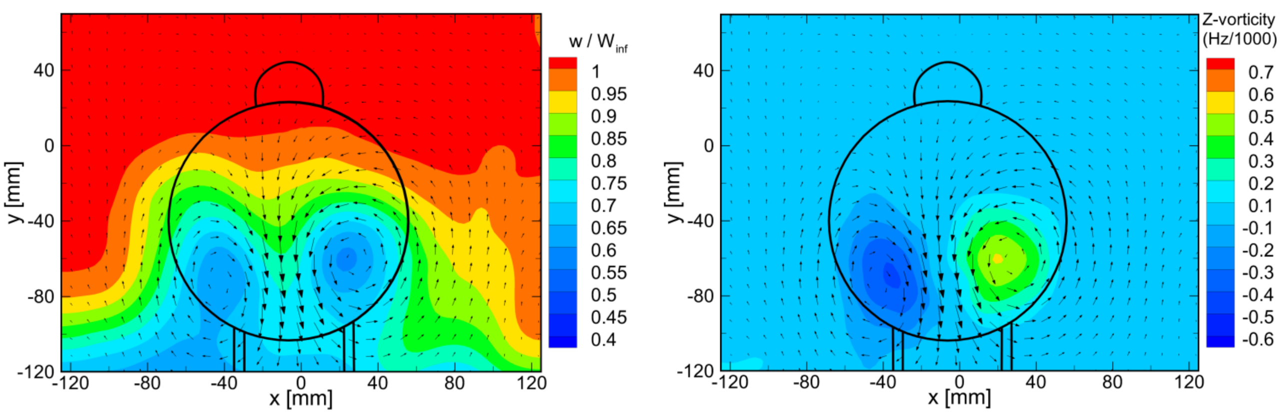

Figure 5.2: Time-averaged velocity (left) and vorticity (right) fields at plane z/D =2.

Comparison of y-velocity profiles:

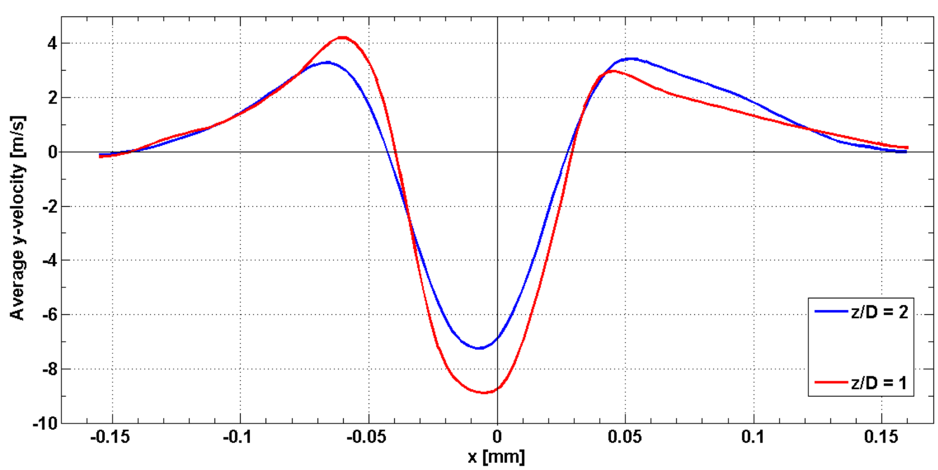

Figure 5.3: Average y-velocity profile comparison between z/D = 1 and z/D = 2 along a line joining the center of the two vortices.

From the above velocity profile comparison (see Figure 5.3) between the two planes, it is observed that as the measurement plane is moved downstream, the slope of the average vertical velocity profile ($d\bar{v}/dy$) along the line joining the centers of the two vortices decreases. By definition, the vorticity in a plane depends on the slope of the vertical velocity. As the slope of the average vertical velocity reduces downstream, the average vorticity also decreases. Hence, it is observed that the vortices reduce in strength and get diffused as the plane of observation moves downstream.

Comparison of Z-vorticity profiles:

In Figure 5.4, the Z-vorticity is plotted along the line joining the centers of the two vortices. From the Z-vorticity profile comparison between the two different z-planes in Figure 5.4, it can be clearly observed that the magnitude of peak vorticity reduces by 37.5% as we move the plane of observation further downstream. This clearly indicates that the vortices that are formed at the plane z/D = 1 tend to get diffused as they propagate downstream.

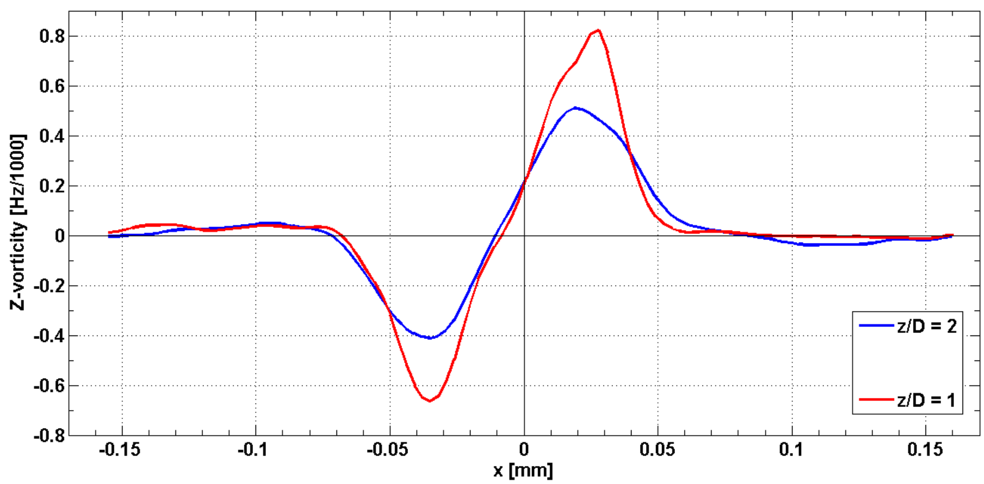

Figure 5.4: Z-vorticity profile comparison between the two different z-planes

5.1.2. Effect of nose shape on mean flow topology

Comparing the mean velocity plots in Figure 5.5-left and Figure 5.6-left, it is observed that the wake occupies a larger area in the reference case compared to the case of the ducted nose. Also, lower velocities are obtained in the wake for the reference case. As a result, the momentum deficit is higher in the reference case. The lower momentum deficit in case of the ducted nose is because the amount of fluid that enters the ducts does not encounter a stagnation point. In the vorticity plots in Figure 5.5-right and Figure 5.6-right, we observe that the formation of the vortex pair is symmetric with respect to the vertical axis in the reference case whereas in case of the ducted nose, the vortex pair is asymmetrical as the vortex axis makes an angle with the vertical axis. We also observe that the strength of the vortex pair increases as the vortices become asymmetrical in case of the ducted nose. In case of the ducted nose, the fluid which approaches the bobsleigh model upstream, passes through the ducts to reach the wake. This jet flow through the ducts entrains the fluid that is flowing outside along the sidewalls of the bobsleigh. The entrainment of the fluid from outside increases the turbulent character of the fluid in the wake. As a result, there is an increase in the vortex strength in case of the ducted nose.

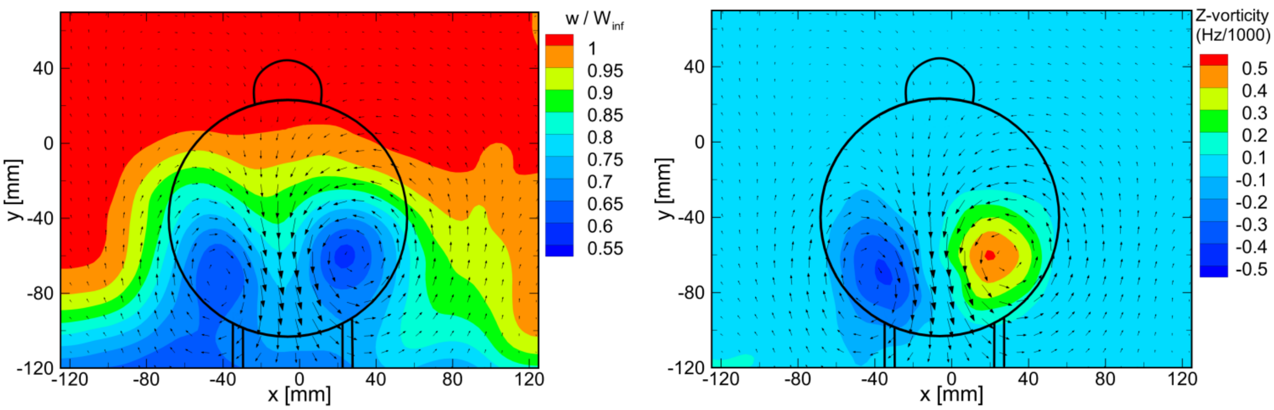

Figure 5.5: Time-averaged velocity (left) and vorticity (right) fields at plane z/D =2 for a reference configuration with no nose rotation.

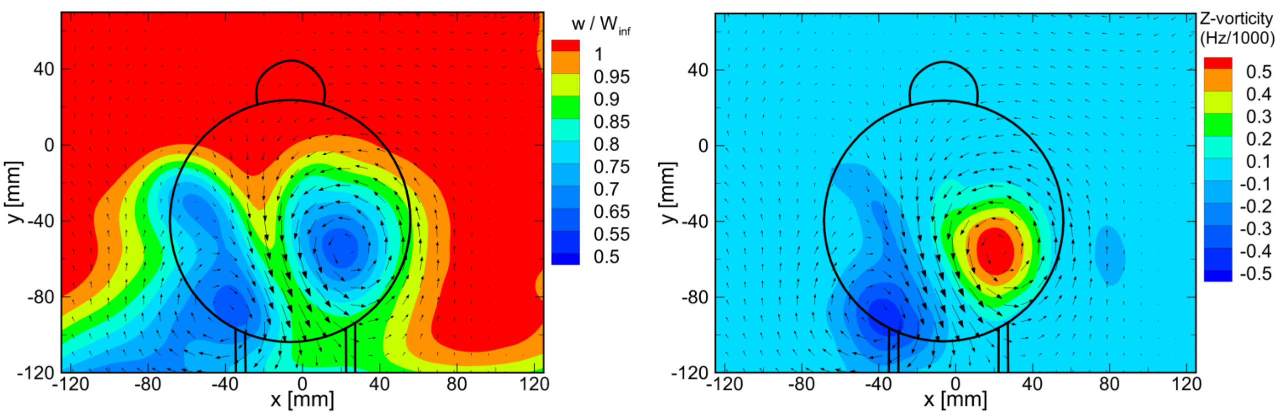

Figure 5.6: Time-averaged velocity (left) and vorticity (right) fields at plane z/D =2 for ducted nose configuration with no nose rotation.

5.1.3. Effect of nose rotation angle on mean flow topology

The mean flow topology in the near wake of the bobsleigh is investigated for different front-cowling rotation angles. The front-cowling is rotated towards the left of the model from 0° to 20° with steps of 5°. The time-averaged velocity plots in Figure 5.7 to Figure 5.11 suggest that as the angle of rotation increases, the momentum deficit initially reduces and then increases. At smaller rotation angles when the increase in frontal area is not significant, the area uncovered by the front cowling increases and more fluid passes through to the wake directly without any blockage from the crew model. Hence the momentum deficit decreases. As the nose is rotated to higher angles, the increase in frontal area dominates over the increase in area uncovered by nose rotation due to additional blockage by the crew model. As a result, the momentum deficit increases marginally from 5° to 20°. This momentum deficit is computed over the entire measurement plane. The variation of momentum deficit as a function of the angle of misalignment of the front cowling is shown in Figure 5.12-left.

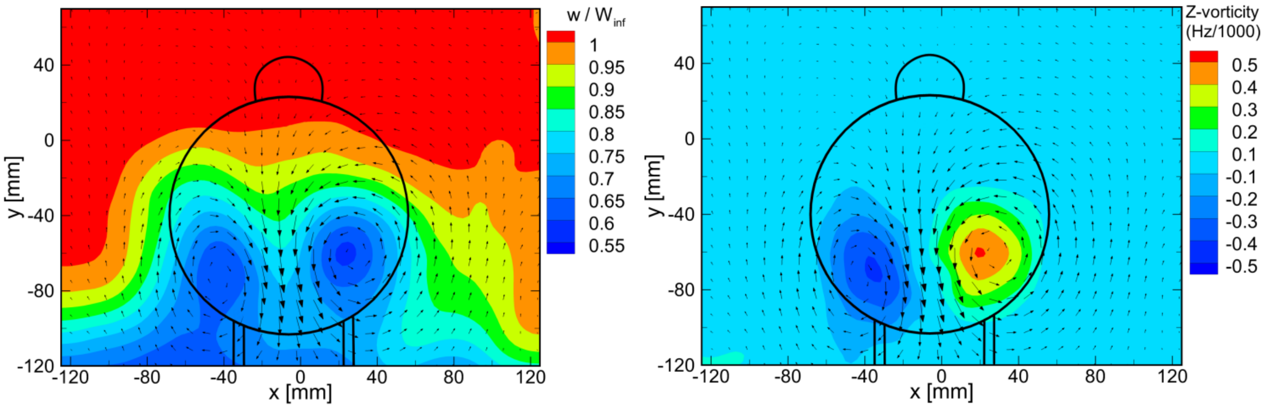

Figure 5.7: Time-averaged velocity (left) and vorticity (right) fields at plane z/D =2 for no nose rotation.

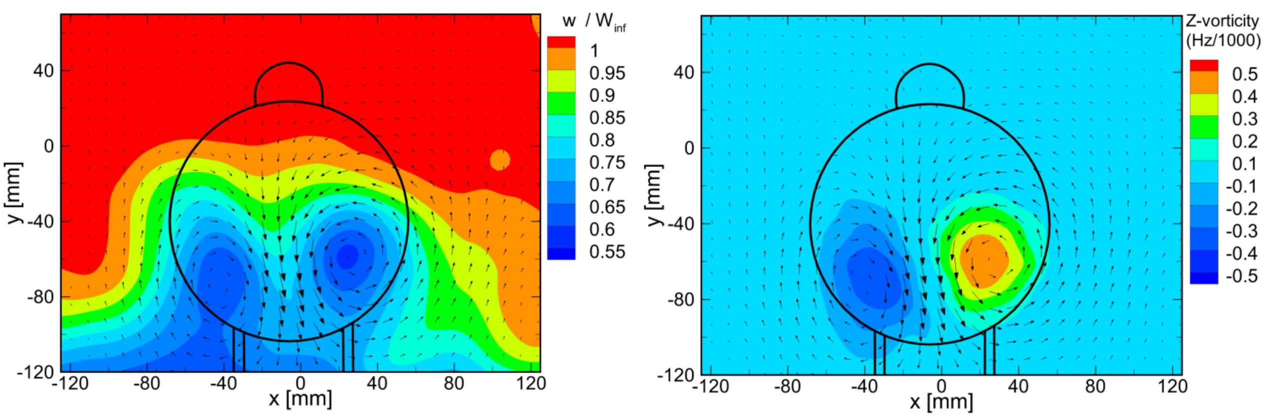

Figure 5.8: Time-averaged velocity (left) and vorticity (right) fields at plane z/D =2 for nose rotation of 5°.

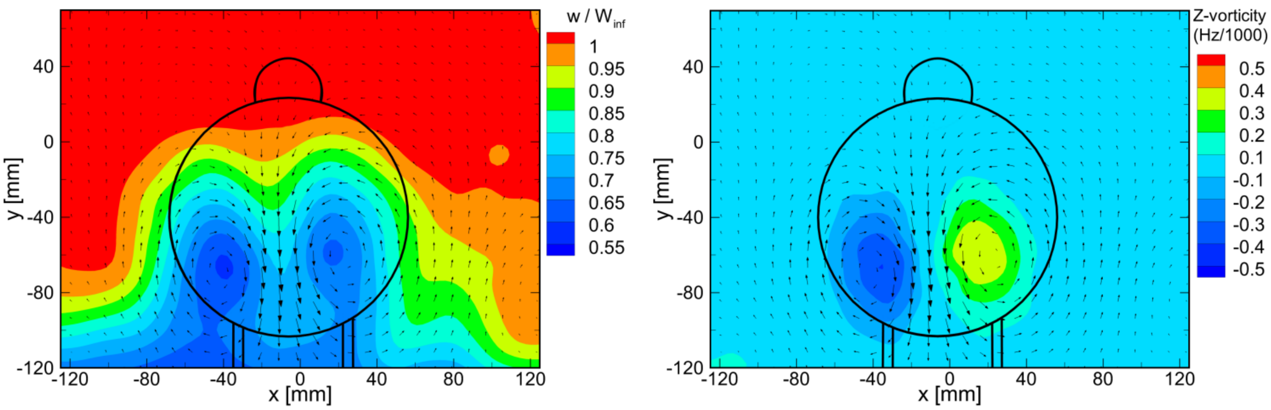

Figure 5.9: Time-averaged velocity (left) and vorticity (right) fields at plane z/D =2 for nose rotation of 10°.

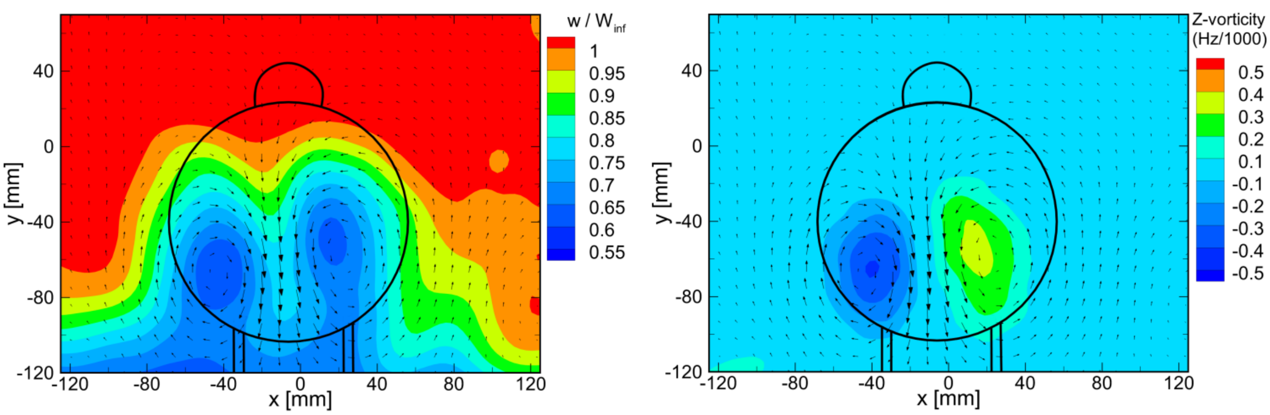

Figure 5.10: Time-averaged velocity (left) and vorticity (right) fields at plane z/D =2 for nose rotation of 15°.

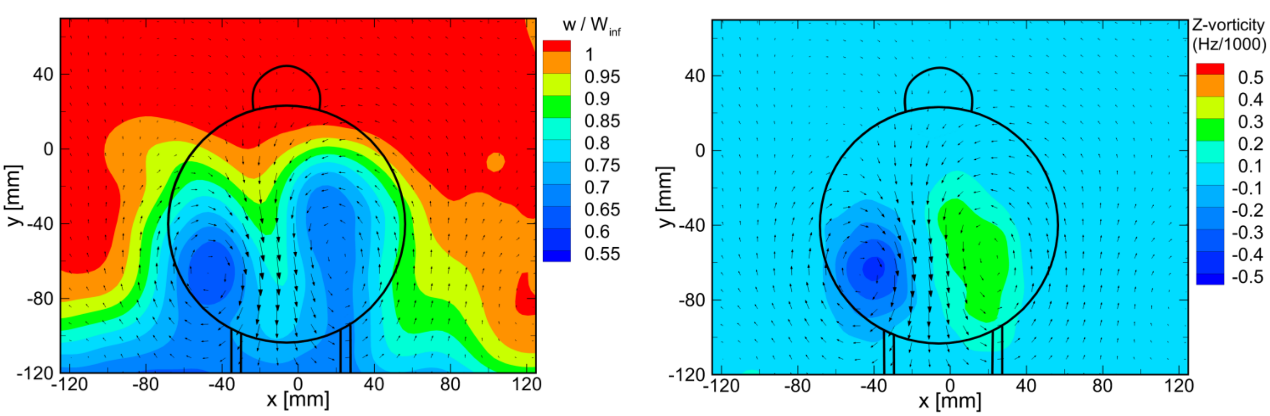

Figure 5.11: Time-averaged velocity (left) and vorticity (right) fields at plane z/D =2 for nose rotation of 20°.

From the vorticity plots in Figure 5.7 to Figure 5.11, it is observed that the strength of the left vortex does not change significantly with the increase in angle of misalignment of the front cowling. As the nose is rotated to the left and the angle is increased, the flow at the left side of the bobsleigh separates from the front-cowling and reattaches onto the rear-cowling. However, due to the length of the rear-cowling (approximately 2.25 D), the flow after reattachment recovers to a condition similar to that in absence of flow separation. Hence, close to the model's trailing edge, the flow on the left side of the bobsleigh is only marginally affected by the front-cowling rotation. As a result, the left vortex shows only minor differences with respect to the 0° front-cowling rotation case, as can be observed in Figure 5.12 where the peak vorticity of the left vortex is nearly unchanged with the angle of misalignment of the front cowling.

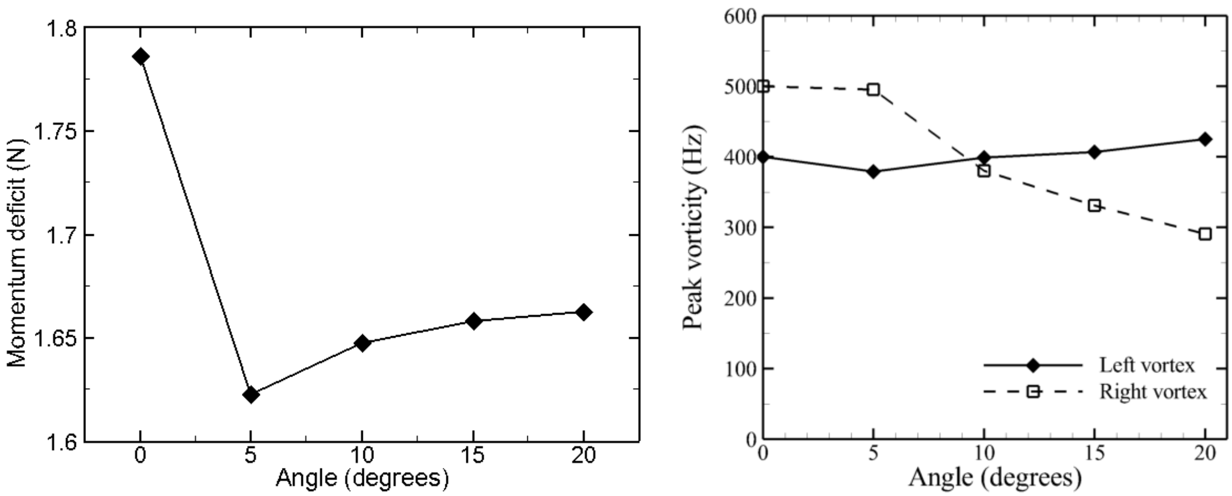

Figure 5.12: Momentum deficit (left) and peak vorticity (right) at different angles of rotation of the front cowling at a measurement plane z/D =2.

Conversely, the peak vorticity of the right vortex decreases by 40% from 0° to 20° (see Figure 5.12-right). As the nose angle increases, the area uncovered by the front cowling increases and more fluid passes through to the wake directly. As a consequence, the pressure difference between the side of the bobsleigh and the inside of the rear cowling decreases, thus reducing the strength of the right vortex.

It is important to note that in case of the ducted nose, the vortex strength of the right vortex increases whereas in case of the 20° misalignment, it decreases with respect to the reference case. In case of the ducted nose, the freestream flow gets accelerated through a uniform duct channel. The flow exiting the duct further entrains the fluid from outside the side walls of the bobsleigh. As a result, the pressure at the location of the right vortex is lower than that of the reference configuration. The lower pressure results in a higher vorticity. However, as compared to the case of the ducted nose, the flow in the case of the 20° misalignment does not have a uniform channel to pass through. Instead, the flow initially gets accelerated due to the small area uncovered due to the nose rotation, and then decelerates as the flow diffuses into the wake. Moreover, there is no flow entrainment in this case. As a result of the lower velocities in the wake, higher pressures are obtained and thereby the strength of the right vortex formed in this case is lower compared to the reference case.

5.1.4. Effect of passive flow control devices on mean flow topology

Some passive control devices like zigzag tape and vortex generators are used to influence the aerodynamics of the flow around the bobsleigh model. From the mean velocity plots of the reference case (Figure 5.13-left) and the case with the vortex generators (Figure 5.15-left), it is observed that in the presence of vortex generators on the sidewalls of the bobsleigh model, lower velocities are obtained in the wake and the wake occupies a larger area as compared to that of the reference case. The broader wake results in a drag increase. The increase in drag is mostly due to the increase in frontal area which causes an increase in vortex drag. With the use of zigzag strips, the mean velocity profile (Figure 5.14-left) indicates slightly higher wake velocities as compared to the reference case (Figure 5.13-left). We observe a slight reduction in drag due to delayed separation of flow over the sidewalls. With the use of the zig-zag strips, it is observed that the flow separates from the sidewalls at a point further downstream as compared to the reference case. Therefore the flow enters the rear cowling with a higher curvature in case of the zig-zag strips as compared to the reference case. From the vorticity plots, it is observed that in case of the zig-zag strips, the vorticity increases by 5%. This increase cannot be attributed to a physical phenomenon and lies within the error limits of the measurement technique. However, in case of the vortex generators, there is an average reduction of 20% in the vorticity. This is due to the fact that the vortex generators break a large vortex into smaller vortices of lower strength.

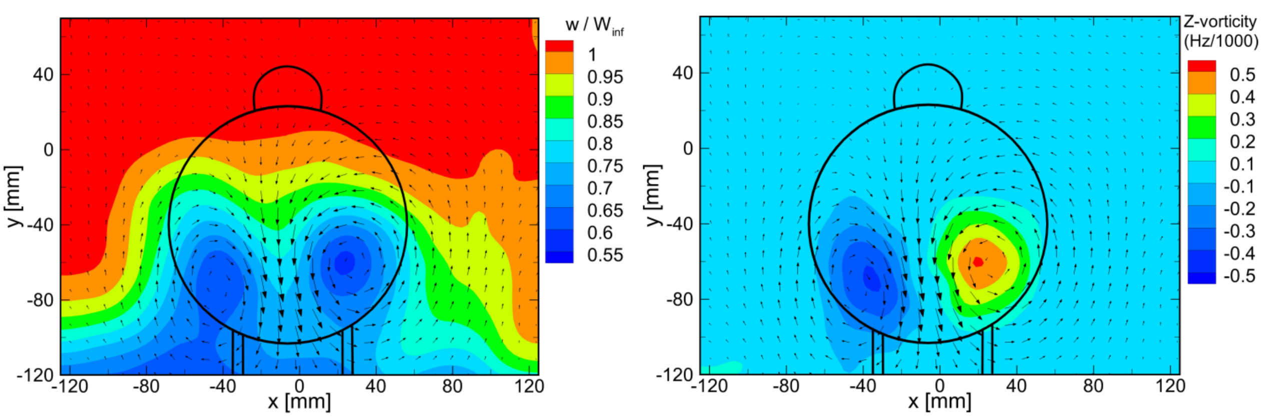

Figure 5.13: Time-averaged velocity (left) and vorticity (right) fields at plane z/D =2 for a clean configuration with no nose rotation.

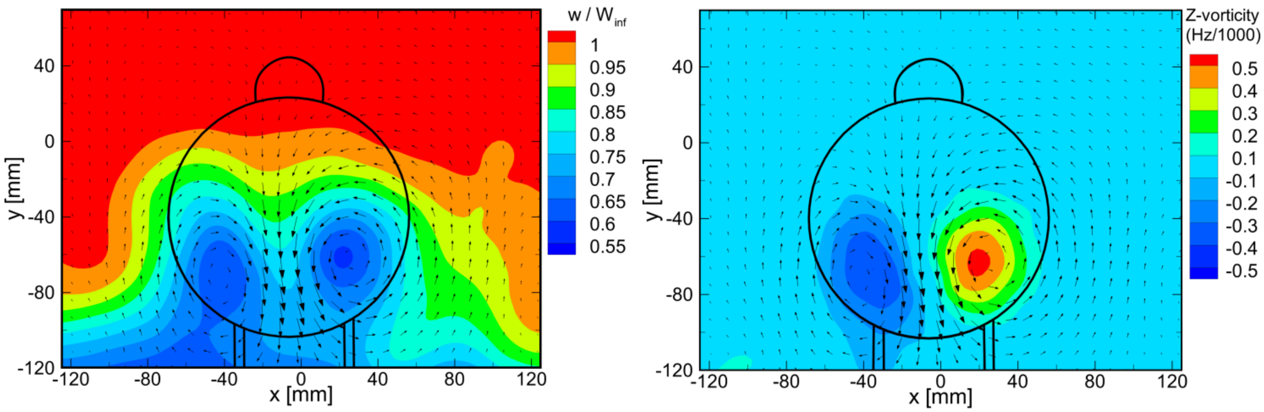

Figure 5.14: Time-averaged velocity (left) and vorticity (right) fields at plane z/D =2 for zig-zag strips configuration with no nose rotation.

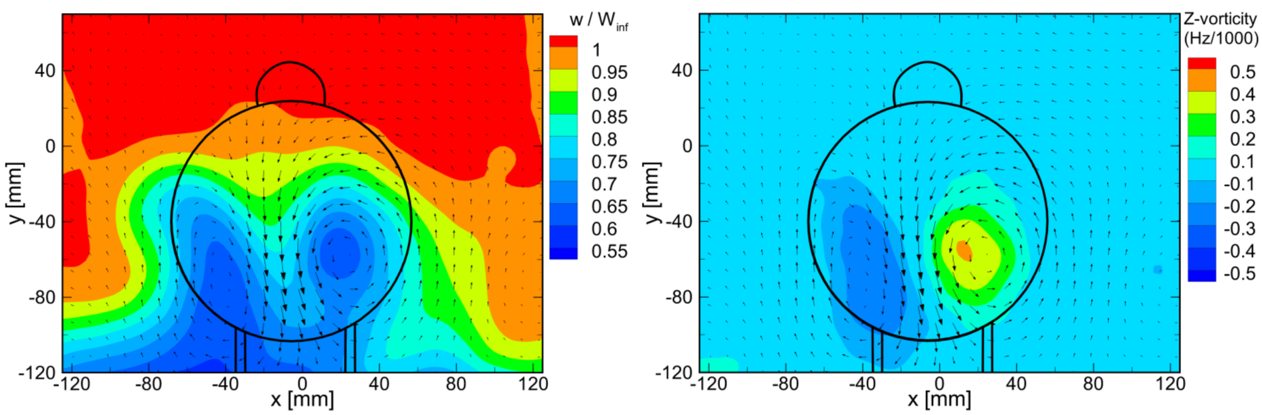

Figure 5.15: Time-averaged velocity (left) and vorticity (right) fields at plane z/D =2 for a configuration with vortex generators and no nose rotation.

5.2. Pressure fields

The static pressure fields are evaluated by solving the Pressure Poisson Equation (Eq.2.16) using the three dimensional velocity field data obtained from stereoscopic PIV. It must be noted that the pressure fields are extremely sensitive to the velocity gradients in the measurement domain and the applied boundary conditions. The pressure fields are validated using the vorticity fields. The vortex core must have lower pressure than the ambient pressure. Thereafter, the pressure term is computed using these validated pressure fields.

5.2.1. Comparison between two different planes

The closer the plane of observation to the bobsleigh model, the higher is the pressure loss and stronger is the eddy formation. This is because at a distance closer to the bluff body, the turbulent fluctuations are higher and as the plane moves further downstream (as in Figure 5.16- right), the flow structures start to diffuse and the eddy strength decreases as well.

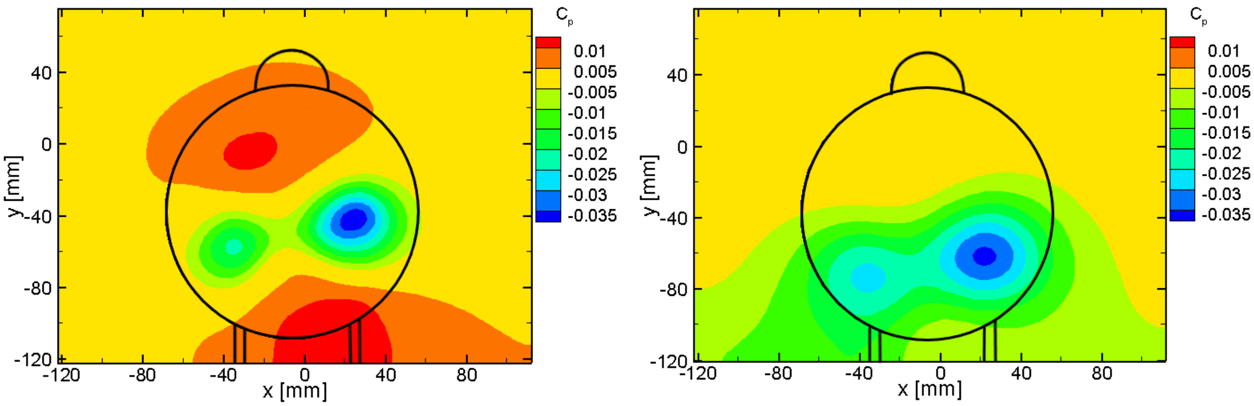

Figure 5.16: Pressure fields at plane z/D = 1 (left) and at plane z/D =2 (right) for a clean configuration with no nose rotation.

In case of the pressure plot on a plane z/D = 1 (see Figure 5.16-left), we observe high pressure regions above and below the low pressure region. This is because the freestream jet flow entrains the flow that is present along the sidewalls of the bobsleigh model and this entrained flow reduces the incoming freestream velocity. Due to the deceleration of the flow, the pressure increases in that region.

5.2.2. Comparison between two different nose angles

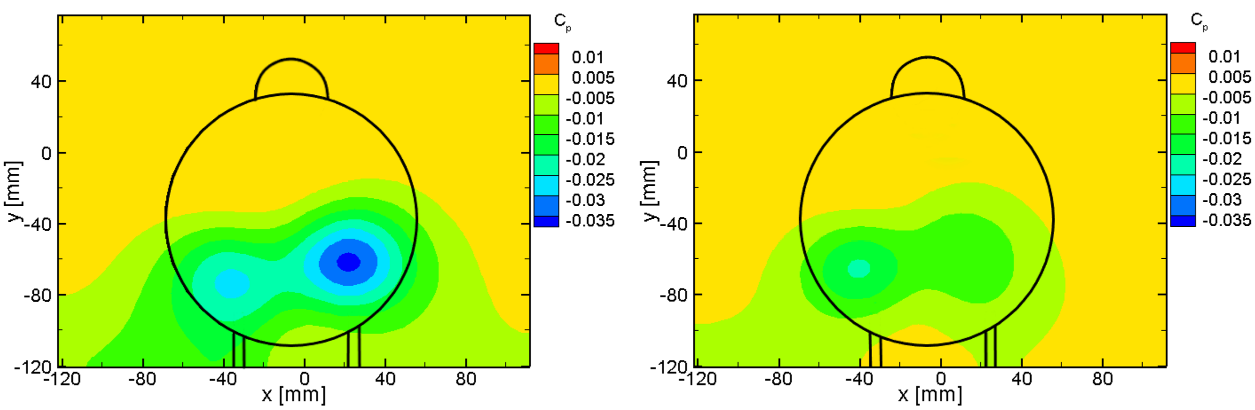

Figure 5.17: Pressure fields at plane z/D = 2 with the front cowling rotation of 0° (left) and 20° (right) for a clean configuration.

From the above plots of the pressure field at two different front cowling angles, higher pressures are observed in case of the 20° misalignment (see Figure 5.17 - right). As explained earlier in section 5.1.3, the strength of the right vortex decreases with increase in misalignment angle. As a result, a weaker right vortex is formed in case of the 20° misalignment thereby resulting in a higher pressure at the location of the right vortex ($x = 20\,mm$, $y = -65\,mm$ in Figure 5.17). The strength of the left vortex nearly remains the same with increase in the misalignment angle as shown in Figure 5.12 in section 5.1.3. As a result, a similar pressure is expected in both the cases at the location of the left vortex ($x = -40\,mm$, $y = -80\,mm$ in Figure 5.17). The minor differences observed in the pressure field at the left vortex location is due to the higher uncertainty involved in the process of pressure determination.

5.2.3. Comparison between two different nose shapes

From Figure 5.18, lower pressure coefficients are observed in the wake in case of the ducted nose as compared to the reference case. As explained earlier in section 5.1.2, in case of the ducted nose, the fluid which approaches the bobsleigh model upstream, passes through the ducts to reach the wake. In addition to this, the fluid flowing along the outer sidewalls of the bobsleigh is entrained due to the jet flow through the ducts. This increases the velocity of the fluid reaching the wake. As a result, the momentum deficit is lower in case of the ducted nose. Due to higher wake velocities in case of the ducted nose, the pressures in the wake are significantly lower as compared to the reference case.

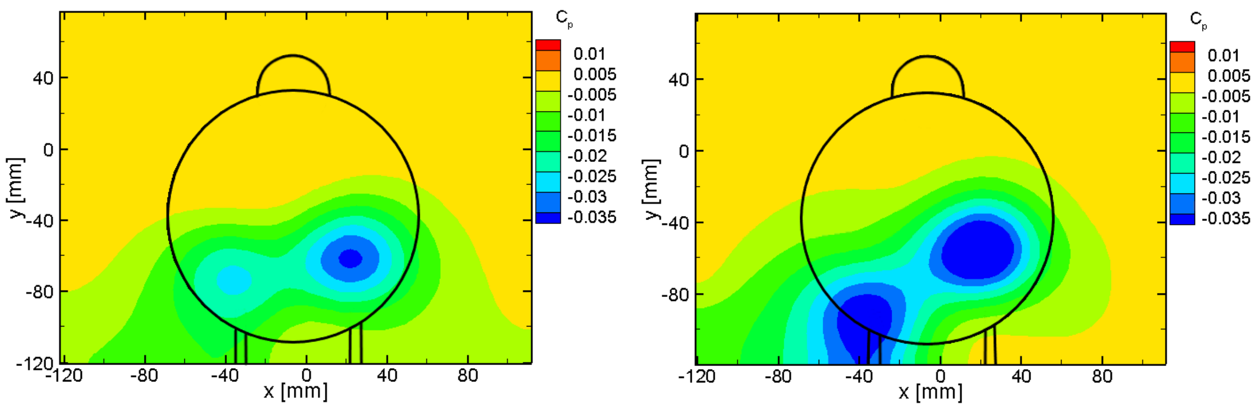

Figure 5.18: Pressure fields at plane z/D = 2 with no front cowling rotation for reference configuration (left) and ducted nose configuration (right).

5.2.4. Comparison between two different configurations

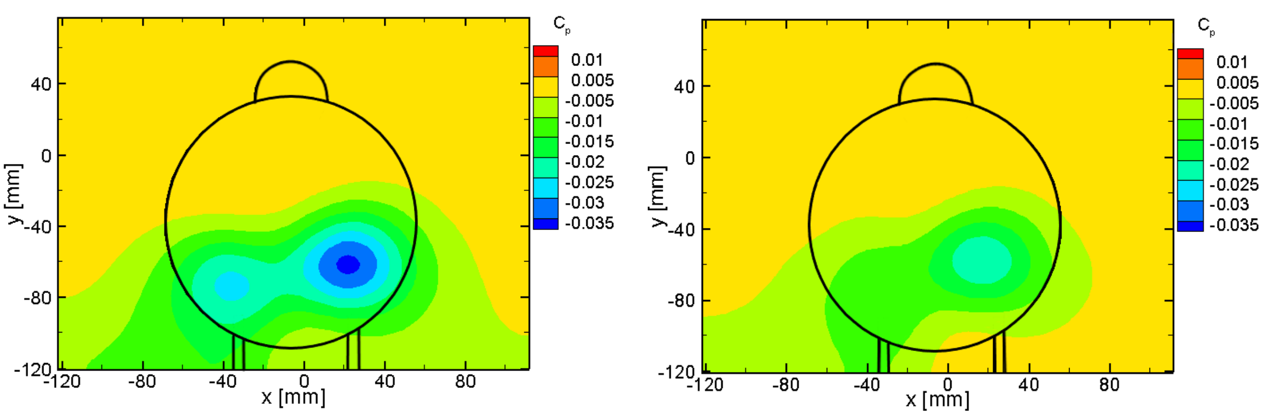

Figure 5.19: Pressure fields at plane z/D = 2 with no front cowling rotation for clean configuration (left) and configuration with vortex generators (right).

From Figure 5.19, lower pressure coefficients are observed in the wake in case of the vortex generators compared to the clean configuration. The vortex generators break the formation of a big vortex into smaller vortices and thereby reduce the vortex strength. As the vortex strength reduces, there is a decrease in circulation and an increase in wake pressures as compared to the clean configuration.

5.3. Velocity fluctuations

The fluctuations in the velocity field are a measure of the turbulence intensity in the flow. In this section, firstly the non-dimensional streamwise RMS velocity of the clean configuration with no nose rotation (reference configuration) is plotted and analyzed. Further, comparisons are drawn between the velocity fluctuations at different speeds and also at different configurations.

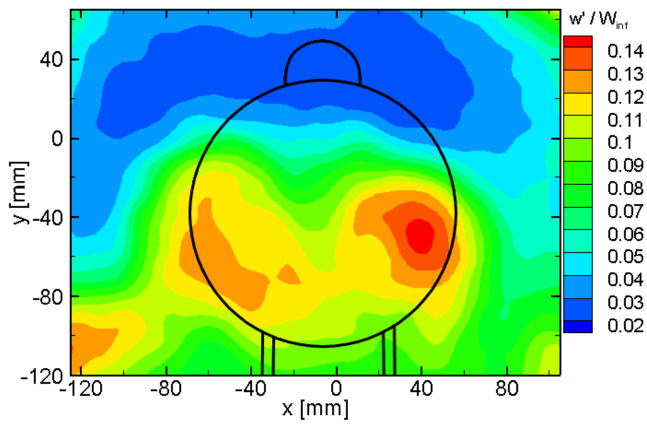

Figure 5.20: Non-dimensional streamwise RMS velocity for the reference case

From the plot of the fluctuations in *z*-velocity (see Figure 5.20), it can be observed that large fluctuations are present in the region where the vortices are formed in the wake. The turbulence added due to the formation of the vortices produces large fluctuations. From Figure 5.20, it is observed that the region above the bobsleigh having the lowest fluctuations has freestream conditions. The large fluctuations present along the edges of the contour are due to the formation of the turbulent shear layer between the outer wall of the model and the fluid.

5.3.1. Comparison between two different wind velocities

From Figure 5.21, it is observed that as the streamwise velocity increases from 15 m/s to 25 m/s, the streamwise RMS velocity increases as well. This is because at higher speeds, the effects of turbulence are more prominent. As the wind velocity increases, the Reynolds number of the flow increases and thus the turbulent character of the flow increases as well. However, the non-dimensional streamwise RMS velocity (w'/W_∞) remains nearly constant. This can be observed in the plots shown in Figure 5.21.

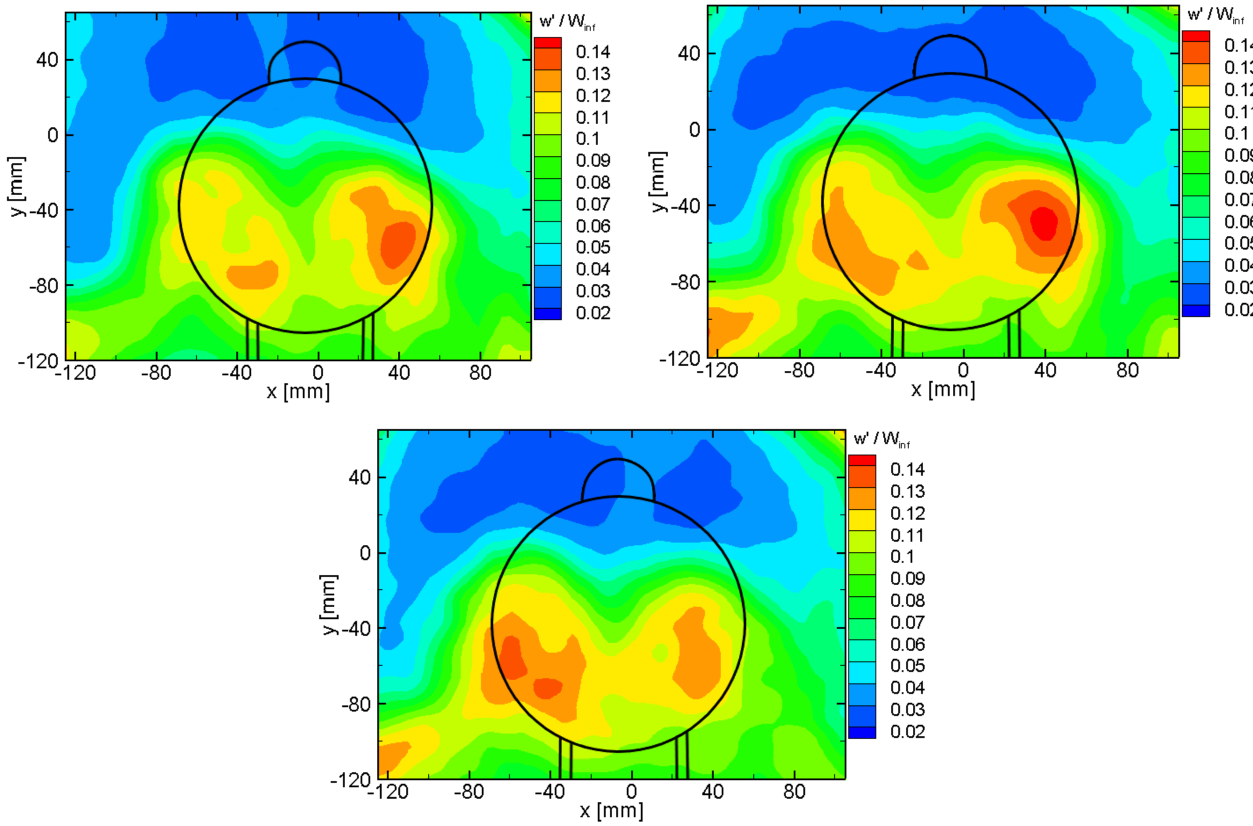

Figure 5.21: Non-dimensional streamwise RMS velocity at plane z/D = 2 with no front cowling rotation at speeds of 15 m/s (upper left), 20 m/s (upper right) and 25 m/s (bottom centre)

5.3.2. Comparison between two different configurations

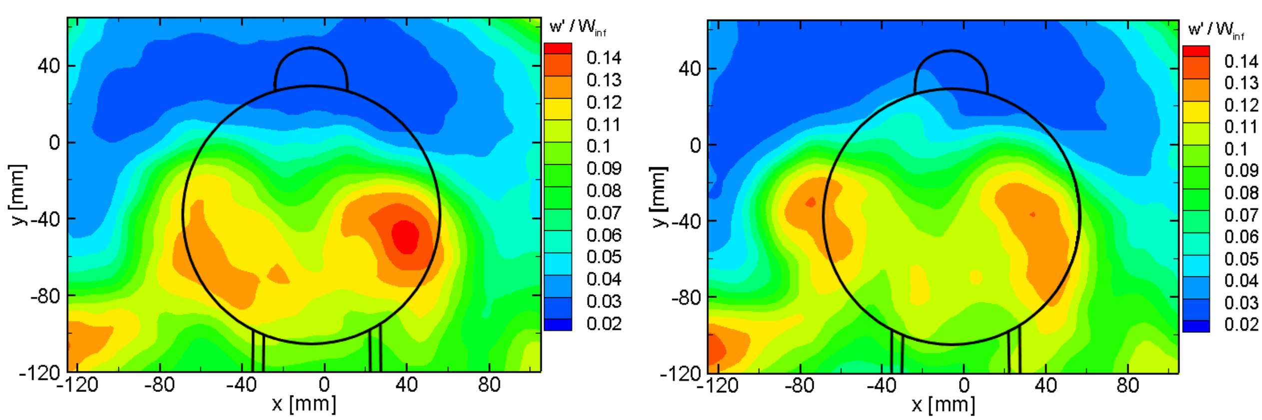

Figure 5.22: Non-dimensional streamwise RMS velocity at plane z/D = 2 with no front cowling rotation for the clean configuration (left) and for the configuration with vortex generators (right)

From the contours of non-dimensional streamwise RMS velocities for two different configurations (see Figure 5.22), it is observed that in case of the vortex generators, the turbulence intensity is lower in the wake region as compared to the clean case. This is due to the fact that the vortex generators break up a single large vortex into smaller vortices thereby reducing the strength of the vortex and hence reducing the velocity fluctuations in the wake.

5.4. Aerodynamic drag

The aerodynamic drag is a combination of several terms as shown in Section 2.4. This section presents the average contribution of each of the terms constituting the aerodynamic drag namely the momentum term, the Reynolds stress term and the pressure term. A pie chart indicating the independent contribution of each term at a cross-plane z/D = 2 is shown in Figure 5.23. The significance of each term is explained in the section 4.2.

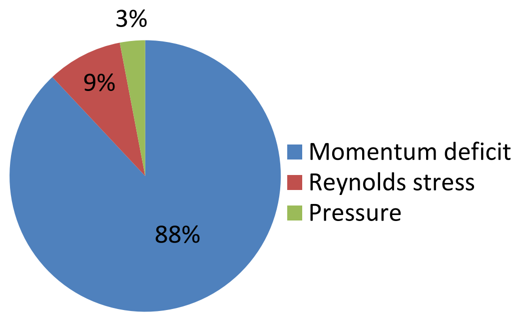

Figure 5.23: Contribution of several factors to overall aerodynamic drag

(a) Momentum term

The momentum term has the most significant contribution to the aerodynamic drag. The deficit in momentum is found to be very large in the regions where there is a formation of vortical structures in the near wake of the bobsleigh model. The vortices transfer energy from the streamwise velocity component to the in-plane components causing large momentum deficits in the streamwise direction thereby contributing to the total drag.

In this research, for different nose rotation angles (0° to 20°) and a freestream velocity of 20 m/s, the momentum term was found to contribute in the range 87% to 89% to the total aerodynamic drag.

(b) Reynolds Stress term

The Reynolds stress term is composed of the integral of fluctuating streamwise velocity components Re_{zz}. In this study the fluctuating components in the streamwise direction primarily arise from the turbulence caused by the formation of the vortices in the wake and due to the shear layers formed on the sidewalls of the bobsleigh while the flow enters the rear cowling.

In this study, for different nose rotation angles (0° to 20°) and a freestream velocity of 20 m/s the integral of Re_{zz} results in a contribution in the range of 8% to 9% to the total aerodynamic drag. This is consistent with the fact that the Reynolds Stress is the second largest contributor.

(c) Pressure term

The pressure term is the least of the contributors to the drag force and it is evaluated using the methodology described in section 2.4. The absolute pressures in the wake are related to the strength of the vortical structures formed in the wake of the body. Stronger the vortex, lower will be the pressure in the wake. As observed earlier in section 5.1.3, the strength of the right vortex decreases whereas that of the left vortex remains the same as the nose rotation angle is increased. Hence, as the angle of nose rotation is increased, the pressure difference that is responsible for the pressure term in the drag equation decreases. The pressure term contributes in the range 2% to 4% to the total aerodynamic drag.

Contribution of terms to drag computation				
Term	Value (N)	% contribution	Uncertainty U (N)	$(U/\bar{F}_{Drag})$*100
Momentum	1.7858	88	0.1153	6.73
Reynolds	-0.1395	8	0.0088	0.51
Pressure	0.0661	4	0.0126	0.74
Drag ($\bar{F}_{Drag}$)	1.7125	100	0.1163	6.79

Table 5.1: Contribution of individual terms to the total drag along with uncertainty for the reference configuration

The values indicated in Table 5.1 are obtained after applying the freestream velocity correction (as shown in section 4.2.1) based on the work of Merker and Wiedemann (1996). Table 5.1 shows the contribution of all the terms towards the computation of the overall drag. It is observed that the momentum term contributes the maximum and pressure term contributes the minimum to the overall drag. The major contribution of the momentum term is due to the fact that the momentum term depends upon the streamwise velocity which has a much higher magnitude compared to that of velocity fluctuations. Even the pressure difference between the freestream and the wake is quite negligible compared to the streamwise velocity. However, it is observed that the uncertainty of the momentum term is the highest and that of the Reynolds stress term is the lowest.

5.4.1. Uncertainty analysis

As shown earlier in section 4.3, the average aerodynamic drag is primarily a function of three variables namely the mean streamwise velocity, the Reynolds normal stress and the average pressure. Each of these variables has a particular uncertainty which contributes to the overall uncertainty of the average drag. The uncertainty of each of the variables is computed using the formulae mentioned in section 4.3. The Table 5.2 shows the uncertainty of these variables computed for the reference configuration.

Variable	Uncertainty	Reference value
Mean streamwise velocity $(\overline{\mathbf{w}})$	0.1238 m/s	20.2 m/s
Reynolds normal stress $\left(\overline{\mathbf{w}'^2}\right)$	0.1514 m^2/s^2	17 m^2/s^2
Mean pressure $(\overline{\boldsymbol{p}})$	0.2168 Pa	250 Pa

Table 5.2: Uncertainty of different variables contributing to the uncertainty of overall drag

The uncertainty of the mean pressure is comparatively higher than that of both the Reynolds normal stress and the mean streamwise velocity because of the fact that pressure is a derived quantity whereas the Reynolds stress components and the mean streamwise velocity are directly obtained from PIV measurements. Hence the uncertainty in the computation of mean pressure increases with every step of pressure determination. Secondly, the uncertainty of mean pressure depends upon the uncertainty of the other two variables along with an additional variable namely the Reynolds shear stress (as shown in Eqn 4.31 in section 4.3) which adds to the uncertainty of pressure. The uncertainty of Reynolds shear stress depends on the correlation between the two in-plane velocity components. The higher magnitude of uncertainty for the Reynolds shear stress is due to the fact that the in-plane velocity components are highly correlated.

5.4.2. Comparison between PIV and balance measurements

Figure 5.24 shows the comparison of the drag coefficient obtained from balance measurements and stereoscopic PIV. The latter is obtained from time-averaged results over 500 uncorrelated samples on plane z/D = 2. For the computation of the momentum deficit from the PIV results, the flow velocity upstream of the model must be known. If this velocity is set equal to the free-stream velocity (20 m/s), the drag coefficient is underestimated by about 10% with respect to the balance measurements. However, due to the expansion of the jet at the exit of the test section, the flow velocity upstream of the model is lower than the free-stream velocity.

Upon applying the freestream velocity correction as mentioned in section 4.2.1, a difference of 2% to 3% is observed between the balance and the corrected PIV drag coefficient measurements. The uncertainty on, the drag coefficient obtained from PIV, is evaluated using the error propagation formula [54]. Since the momentum term accounts for the major contribution to the overall drag, the uncertainty in the Reynolds stress term and the pressure term is neglected. The error bars indicate the expanded uncertainty on the drag evaluated at 95% confidence level.

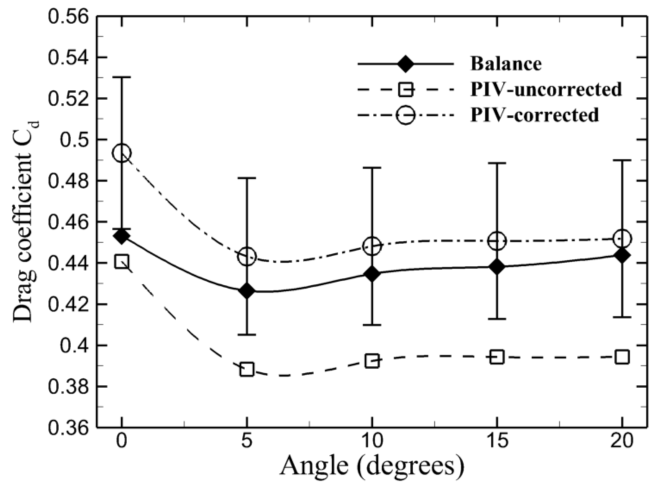

Figure 5.24: Drag coefficient at different angles of rotation of the front cowling along with error bars indicating uncertainty in drag evaluated at 95% confidence level.

The plot of Figure 5.24 shows that the aerodynamic drag first decreases for front-cowling rotations below 5° and then increases. The initial reduction in aerodynamic drag is due to the fact that from 0° to 5°, a strong jet flow occurs due to the fluid passing through the area uncovered by the nose rotation; such jet flow energizes the wake. However, as the angle increases further from 5° to 20°, the increase in frontal area plays a dominant role in lowering the wake velocities and increasing the momentum deficit. This counteracts the advantageous jet-effect within the wake and in turn increases the drag at higher angles.

5.4.3. Comparison at different speeds

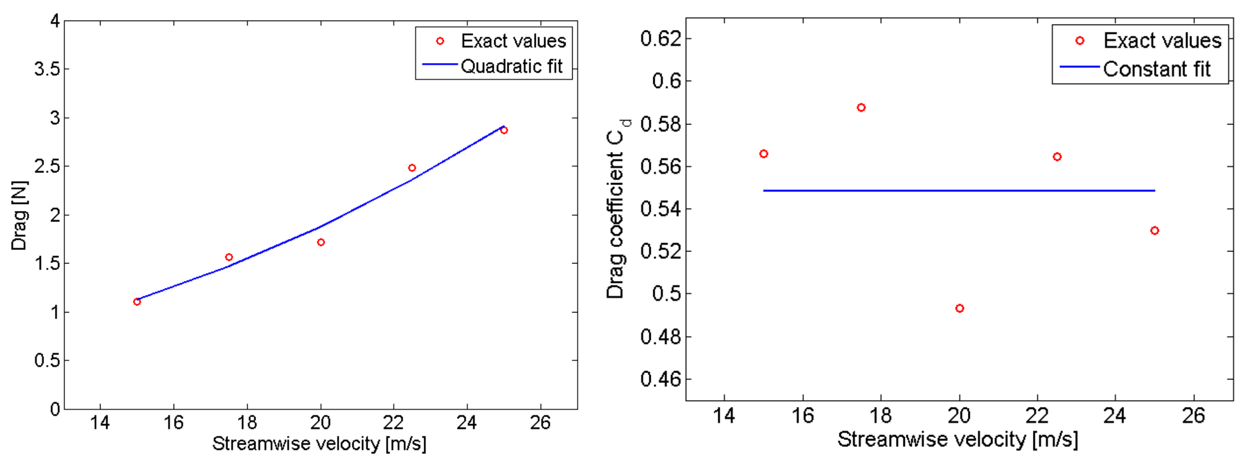

Figure 5.25: Variation of aerodynamic drag (left) and drag coefficient (right) with streamwise velocity at a plane z/D = 2 with no front cowling rotation

From Figure 5.25-left, it is observed that red points in the plot indicate the exact drag values obtained from PIV measurements and the blue curve is a quadratic fit for the measured values. The drag increases in a quadratic manner with the increase in velocity. Similarly from Figure 5.25-right, it can be observed that a constant fit for the drag coefficient is applied with the increase in speed. Table **5.3** shows the deviations of the measured values from the fitted curve for both the cases.

Drag (N)				Drag coefficient C_d			
Velocity (m/s)	Measured drag (N)	Quadratic fit (N)	Error (N)	Velocity (m/s)	Measured C_d	Constant fit	Error
15	1.105	1.1252	-0.0202	15	0.5659	0.5482	0.0177
17.5	1.5614	1.4662	0.0952	17.5	0.5875	0.5482	0.0393
20	1.7125	1.8768	-0.1643	20	0.4934	0.5482	-0.0548
22.5	2.4809	2.3570	0.1239	22.5	0.5647	0.5482	0.0165
25	2.8721	2.9067	-0.0346	25	0.5296	0.5482	-0.0186
RMS error = 0.103 N				RMS error = 0.0331			

Table 5.3: RMS error due to deviation of the measured points from the fitted curves for drag and C_d as a function of velocity

The quadratic increase in drag with increase in velocity is well expected from the drag equation $\left(F_{Drag} = 0.5 \times \rho \times v^2 \times C_d \times A\right)$. The drag coefficient $\left(C_d = F_{Drag}/(0.5 \times \rho \times v^2 \times A)\right)$ is expected to remain nearly constant with the velocity of the fluid due to the fact that drag increases with the square of the velocity and thus the ratio of the drag to the square of velocity for a constant frontal area is nearly a constant.

The RMS error in the computation of drag by the curve fitting method as observed in Table **5.3** is 0.103 N. However, the uncertainty in drag obtained by the linear error propagation formula is 0.1163 N (see Table 5.1). The difference observed between the two values is due to the assumptions made during the application of linear error propagation on the full Poisson's equation for pressure.

5.4.4. Comparison between different configurations

From Figure 5.26, focussing on the effect of the passive flow control devices on the original front cowling (normal nose), it is observed that there is a drag reduction of 2.5% compared to the clean configuration in the presence of zigzag strips whereas an increase of 2.8% is observed in the presence of vortex generators.

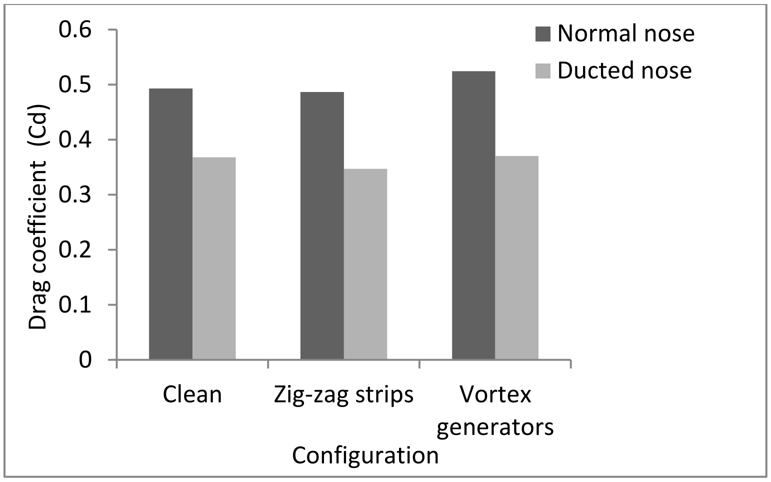

Figure 5.26: Aerodynamic drag using passive flow control devices

However, looking at the clean configuration, it is observed that there is a drag reduction of about 30% when the normal nose is modified and replaced by the ducted nose configuration. In the presence of zigzag strips and vortex generators on the modified front cowling, the reduction is around 40%. This increase in drag reduction is due to the combination of the effects of shape modification and addition of passive flow control devices.

5.5. Proper Orthogonal Decomposition Analysis

The POD analysis is conducted on the velocity fluctuations of the reference configuration (at $z/D = 2$ plane and no nose rotation). In this study the first two POD modes are shown in Figure 5.27 and Figure 5.28 and colour contoured by the velocities in the x and y directions. In each of the modes, two major large-scale turbulent flow structures are observed. The motion of the flow structures can be observed by combining the two POD modes. From the v-components of the two modes, it can be observed that the flow structures have a quasi-circular motion. The flow structures have a clockwise rotation along with a horizontal motion. The intensity of one of the structures reduces and that of the other increases from one mode to another. However, it can also be seen that the two modes are not perfectly correlated to each other. This is because as the flow is highly three-dimensional, the flow structures tend to get shifted from their original position from one mode to another. From the u-components of the POD modes, it can be observed that the two major flow structures are formed at mirror-image positions with respect to each other between the two modes. However the intensity of both the structures reduces from the first mode to the second mode. From the w-components of the two modes, it is observed that one of the two major flow structures performs a translational motion away from and close to the other in the first and the second modes respectively. The intensity of one of the structures increases while that of the other decreases from one mode to another. The fractions of the energy in flow fluctuations of the first and the second modes are approximately 7.5% and 6% respectively. These two modes are the most energetic among the 500 modes that are obtained from the POD analysis.

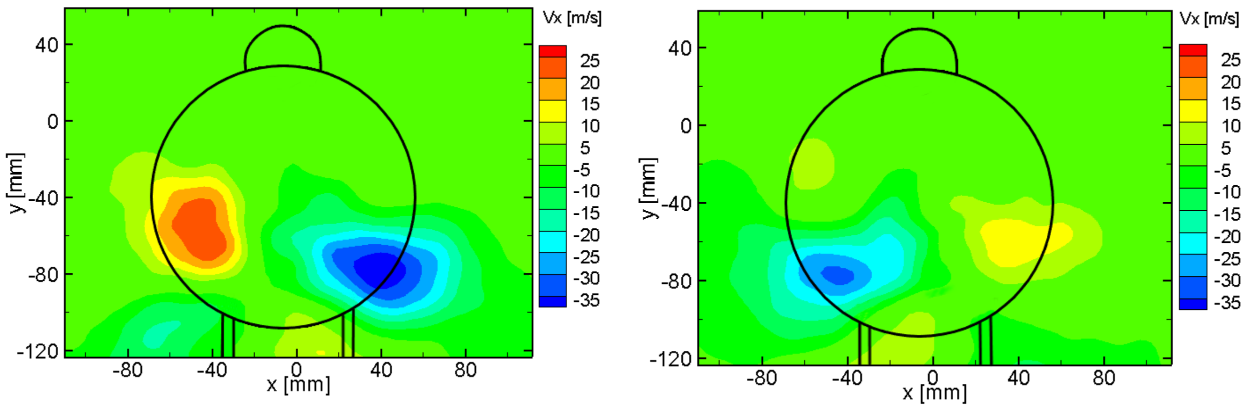

Figure 5.27: Shape of the u-components of the first (left) and second (right) POD modes for the reference configuration.

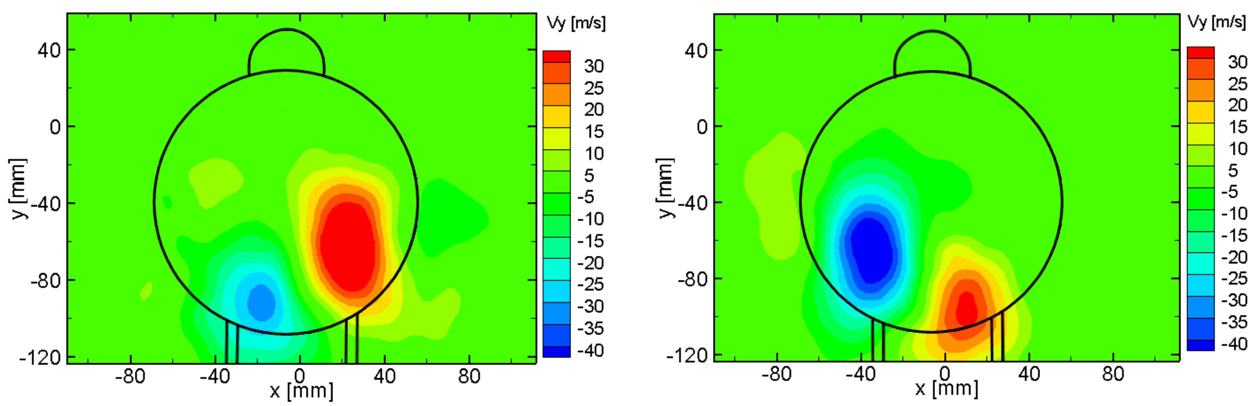

Figure 5.28: Shape of the v-components of the first (left) and second (right) POD modes for the reference configuration.

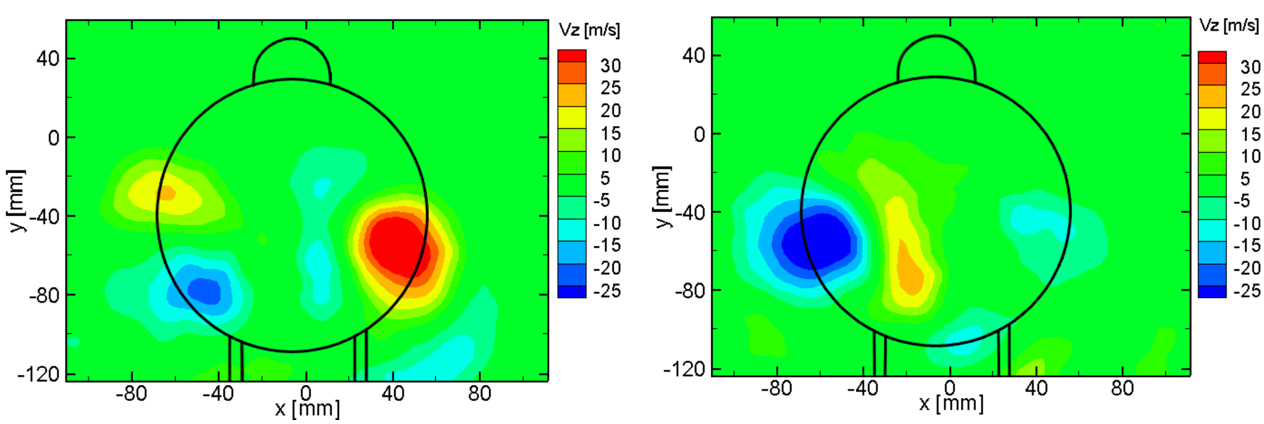

Figure 5.29: Shape of the w-components of the first (left) and second (right) POD modes for the reference configuration.

6

Conclusions and Recommendations

The present work in this thesis is a continuation of the effort at TU Delft towards drag reduction in the field of speed sports. The main focus of this thesis is to investigate the near wake flow topology of the scaled model of a bobsleigh in order to gain a thorough understanding on the possible sources and mechanisms of drag generation and to get a deeper insight on the flow structures generated in the wake. The near wake investigation has been performed by means of 2D stereoscopic PIV measurements and the aerodynamic drag has been evaluated from these measurements using the control volume approach. The drag obtained from PIV measurements is compared to that obtained from external balance measurements in order to check the accuracy of the results. Further, the thesis contributes to a more comprehensive assessment and a thorough understanding of the complex flow in the wake of a bobsleigh. The complex nature of the flow is observed by the presence of a number of vortical structures along with twisted streamlines in the cavity of the scaled model of a bobsleigh.

6.1. Conclusions

On reviewing all the relevant literature, gathering all the experimental data, processing the data and analyzing the results, conclusions can be drawn upon the research carried out for this thesis.

Bobsleigh is a bluff-body which has a pressure difference present between the flow upstream of the body and the flow in the wake of the body. The aerodynamic drag of such bodies is strongly influenced by geometry and flow separation. Thus the pressure drag is the major component of the total drag.

The investigation of the near wake flow topology of the bobsleigh has revealed the presence of two counter-rotating vortices with a significant downwash between them in case of the reference configuration. As the vortices are convected downstream, the peak vorticity of the two vortices is reduced by 40%. A turbulent diffusion of the flow structures is observed as the measurement plane is moved downstream.

The concept of ducted nose configuration was introduced in order to examine the contribution of momentum deficit to the total drag. In the presence of a ducted nose, a 30% reduction in the aerodynamic drag is observed for the clean configuration as a result of a lower momentum deficit obtained due to the flow passing directly to the wake through the ducts. This illustrates the fact that momentum deficit is a major source of aerodynamic drag.

The investigation of the effect of the front cowling misalignment on the drag revealed that there is a reduction of drag for smaller misalignment angles (upto 5°) and a marginal increase in drag for further increase of misalignment (from 5° to 20°). The initial decrease in drag for smaller angles was due to the acceleration of the flow in between the sidewall and the crew due to the area uncovered by the small rotation thereby creating a jet effect while the increase in frontal area was not significant. As the angle increases further, the frontal area becomes more significant and the jet effect reduces due to the increase in the uncovered area and due to the distortion of the flow by the presence of the crew. This effect is analyzed and demonstrated through average velocity plots and vorticity plots for all the angles of misalignment.

The idea behind the attachment of passive flow control devices was to check whether they can alter the flow so as to reduce the aerodynamic drag. From this investigation, it is revealed that the vortex generators are successful in breaking the large flow structures (eddies) of high intensity into smaller ones with lower intensity. However, these devices increase the total drag by 2.8% compared to the clean configuration due to a higher frontal area in the presence of the vortex generators. The addition of zig-zag strips resulted in a drag reduction of 2.5%. Overall, it is concluded that the passive flow control devices are not very effective in reducing drag.

This thesis also determines the average pressure fields for all the bobsleigh configurations that are analyzed. The pressure determination is based on solving the Pressure Poisson Equation using the velocity fields obtained from PIV data. The pressure fields serve as a confirmation of the results obtained from the vorticity and the time average-velocity plots.

Another interesting parameter that is discussed is the velocity fluctuations in the flow. It gives us a measure of the turbulence intensity at different regions of the wake. It has been found that the fluctuations are at its maximum at the location of the formation of vortices. However, the boundaries which have the freestream conditions experience the lowest velocity fluctuations. Velocity fluctuations are computed at different streamwise velocities in order to illustrate that the turbulence intensity in the flow increases with the increase in Reynolds number.

From the analysis of aerodynamic drag conducted on a vertical plane that is approximately 2D behind the bobsleigh model, it can be seen that the momentum deficit is the highest contributor to the aerodynamic drag (88%) followed by the Reynolds stresses (9%) and pressure (3%). The aerodynamic drag obtained from PIV is first corrected for freestream velocities due to the jet expansion effect and the nose blockage effect. After correction, the PIV drag results are compared to the results obtained from external balance measurements and there is a good agreement of the two sets of results with a deviation of 2% to 3%. The aerodynamic drag variation with streamwise velocity reveals that the drag increases in a quadratic manner with velocity whereas the drag coefficient is nearly a constant with a variation of $\pm$ 10%.

The most novel part of this thesis is the uncertainty quantification of drag. This is done by using the linear error propagation formula. The uncertainty of each of the terms of the drag equation is evaluated. It is shown that the uncertainty of the momentum term is the maximum as compared to the other terms. This is due to the higher magnitude of the streamwise velocity component as compared to the velocity fluctuations. The uncertainty of average pressure is derived from the full Poisson's equation for pressure. The uncertainty of other flow variables contributing to the drag is also computed. It is also shown that among all the flow variables, the uncertainty of average pressure is the maximum due to the fact that pressure is a derived quantity in PIV and the uncertainty increases with every step of pressure determination.

Finally, a POD analysis is performed for the velocity fluctuations of the reference configuration. The results show that the first two modes of fluctuations are the most energetic ones among the 500 different modes that are obtained. The fractions of the total energy contained in the first and second modes are 7.5% and 6%. The v-components of the two modes show a quasi-circular motion whereas the w-components of the two modes illustrate a translational motion of the flow structures. However, not a lot can be concluded from the POD analysis as it can be seen that the two modes are not perfectly correlated due to the highly three dimensional nature of the flow.

6.2. Recommendations

Even though there are conclusive evidences available for most of the observations in this thesis, there are quite some limitations in terms of lack of knowledge on a few aspects. Even though this research was based on fundamental flow behaviour investigation on a bobsleigh, the scaled model used was not an exact representation of the real bobsleigh. It would be recommended to carry out this research with a more realistic model with additional features such as the bumpers attached to the cowling and changes can be made to the cross sectional shape of the model for more accurate quantitative results.

A complete knowledge of all features of the external flow behaviour cannot be given with the use of the PIV measurements performed in this thesis. In order to get an insight into the separation and reattachment of the flow on the surface of the bobsleigh, it would be recommended to carry out PIV measurements on a vertical mid-plane of the model or on a plane that is more strategically placed so as to capture the maximum changes in flow behaviour.

The accuracy of force balance measurements can be improved as well. In this research, balance measurements were made to investigate the nose rotation for varying wind speeds and nose configurations. The increments in nose rotation were taken to be 5°. It would be recommended to gather force data at smaller nose rotation increments in order to gain a better understanding of the variation of the drag with nose rotation.

Finally it is recommended to also perform shape optimization of the bobsleigh nose in order to reduce drag with nose rotation. It would be also very interesting to think of innovative solutions like boat-tailing of the rear cowling or using different configurations of vortex generators at more strategic locations on the bobsleigh to minimize aerodynamic drag in order to improve the performance of the bobsleigh and thereby gain a competitive advantage in the field of speed sports.

Bibliography

[1] International Bobsleigh & Skeleton Federation (IBSF). Our sports: bobsleigh. http://www.ibsf.org/en/oursports, 2015. [Online]. Accessed: 2015-12-23.

[2] IBSF, Bobsleigh history, [Online] http://www.ibsf.org/en/our-sports/bobsleigh- history, 2015.

[3] R. Starkman - Toronto Star (December 2009). *Canadians capture gold, silver in World Cup bobsleigh competition.* http://www.thestar.com/sports/2009/12/19/canadians_capture_gold_silver_in_world_cup_bobsleigh_compition.html

[4] P. Dabnichki, F. Motallebi, and E. Avital. Advanced bobsleigh design. Part 1: body protection, injury prevention and performance improvement. *Proceedings of the Institution of Mechanical Engineers, Part L: Journal of Materials: Design and Applications*, 218:129–137, 2004.

[5] *International bobsleigh rules 2015*. International Bobsleigh & Skeleton Federation, June 2015.

[6] J. D. Anderson Jr. *Fundamentals of Aerodynamics*. McGraw-Hill, fourth edition, 2005.

[7] F. M. White. *Viscous fluid flow*. McGraw-Hill, second edition, 1991.

[8] R. G. J. Flay. Bluff body aerodynamics. In Y. Tamura and A. Kareem, editors, *Advanced Structural Wind Engineering*, chapter 3, pages 59–84. Springer Japan, 2013.

[9] P.Dabnichki and E. Avital. Influence of the position of crew members on aerodynamics performance of two-man bobsleigh. *Journal of Biomechanics*, 39:2733–2742, 2006.

[10] H. Schlichting. *Boundary-Layer Theory*. McGraw-Hill, seventh edition, 1979.

[11] G. Buresti, G. Iungo, and G. Lombardi. Methods for the drag reduction of bluff bodies and their application to heavy road-vehicles. 1st interim report contract between CRF and DIA, DDIA 2007-6, Dipartimento di Ingegneria Aerospaziale, Università di Pisa, October 2007.

[12] K. R. Cooper. Bluff-body aerodynamics as applied to vehicles. *Journal of Wind Engineering and Industrial Aerodynamics*, 49:1–21, 1993.

[13] T. A. Talay. Introduction to the aerodynamics of flight. NASA-SP-367, National Aeronautics and Space Administration, 1975.

[14] A. Winkler and A. Pernpeintner. Improving the performance of a bobsleigh by aerodynamic optimization. *The Engineering of Sport 7*, 2:329–338, 2008.

[15] Eric W. Weisstein. (2007) *Cylinder Drag.* [Online]. Available from: http://scienceworld.wolfram.com/physics/CylinderDrag.html [Accessed 20th November 2011].

[16] H.Ubbens. Aerodynamic analysis of cowling misalignment on a two man bobsleigh, Master of Science thesis, Delft University of Technology - Faculty of Aerospace Engineering, December 2016.

[17] Yunus A Cengel, Robert H Turner, John M Cimbala, and Mehmet Kanoglu. *Fundamentals of thermal-fluid sciences*. McGraw-Hill New York, NY, 2005.

[18] O. Lewis. Aerodynamic analysis of a 2-man bobsleigh. Master of Science thesis, Delft University of Technology - Faculty of Aerospace Engineering, October 2006.

[19] P. Dabnichki, F. Motallebi and D. Luck. Advanced bobsleigh design. Part 2: aerodynamic modifications to a two-man bobsleigh. *Proceedings of the Institution of Mechanical Engineers, Part L: Journal of Materials: Design and Applications*, 218:139–144, 2004.

[20] H. Chowdhury, F. Alam, S. Arena, and I.Mustary. An experimental study of airflow behaviour around a standard 2-man bobsleigh. *Procedia Engineering*, 60:479–484, May 2013.

[21] Winkler A., Pernpeintner A.: The Engineering of Sport 7, Vol. 2. In Estivalet M., Brisson P. (Eds.) Improving the Performance of a Bobsleigh by Aerodynamic Optimization. Biarritz, 2-6 June. Springer – Verlag France, 2008.

[22] H. Chowdhury, B. Loganathan, F. Alam, and H.Moria. Aerodynamic body position of the brakeman of a 2-man bobsleigh. *Procedia Engineering*, 112:424–429, 2015.

[23] Glenn Research Center, NASA https://www.grc.nasa.gov//k-12/airplane/tunvsmoke.html

[24] William H. Rae, Jr. Alan Pope. Low-speed wind tunnel testing. Wiley & Sons second edition (1984).

[25] Muzafferuddin Mahmood (2011). Flow Visualization in Wind Tunnels, Wind Tunnels and Experimental Fluid Dynamics Research, Prof. Jorge Colman Lerner (Ed.), ISBN:978-953-307-623-2, InTech, Available from: http://www.intechopen.com/books/wind-tunnels-and-experimental-fluid-dynamics-research/flow-visualizationin-wind-tunnels

[26] Yash Hemant Shah. Drag analysis of a full scale cyclist model using large-scale 4D-PTV. Master of Science thesis, Delft University of Technology - Faculty of Aerospace Engineering, July 2017

[27] Prasad A (2000) Stereoscopic particle image velocimetry. Exp Fluids 29:103– 116

[28] F Scarano. Experimental Aerodynamics. Technical report- Delft University of Technology, Aerospace Engineering Department. First edition (February 2013).

[29] Andrea Sciacchitano. *Uncertainty quantification in particle image velocimetry and advances in time-resolved image and data analysis*. PhD thesis, TU Delft, Delft University of Technology, 2014.

[30] Hecht, Eugene (2002). Optics (4th ed.). Addison Wesley. ISBN: 0-321-18878-0

[31] Raffel M, Willert C, Kompenhans J (eds) (1998) Particle image velocimetry—a practical guide. Springer, Berlin Heidelberg New York.

[32] Samimy, M., Lele, S.K.: Motion of particles with inertia in a compressible free shear layer. Phys. Fluids 3(8), 1915–1923 (1991)

[33] Christian Willert. Stereoscopic digital particle Image velocimetry for application in wind tunnel flows. Meas. Sci. Technol.; 1997. Vol 8. 1465 p.

[34] LaVision. Helium filled soap bubbles generator. URL https://lavision.de /en/products/flowmaster/2d-stereo-piv/index.php.

[35] Calluaud D, David L (2004) 3D PIV measurements of the flow around a surface-mounted block. Exp Fluids 36:53–61.

[36] Wieneke B (2004) Application of self-calibration stereo PIV in enclosed measurement volumes. In: Proceedings of the 12th international symposium on the application of laser techniques to fluid mechanics, Lisbon, Portugal, July 2004.

[37] F Scarano, L David, M Bsibsi, D Calluaud. S-PIV comparative assessment: image dewarping +misalignment correction and pinhole + geometric back projection - Experiments in fluids, 2005 – Springer.

[38] John David Anderson Jr. *Fundamentals of aerodynamics*. Tata McGraw-Hill Education, 2010.

[39] DF Kurtulus, F Scarano, and L David. Unsteady aerodynamic forces estimation on a square cylinder by tr-piv. *Experiments in Fluids*, 42(2):185–196, 2007.

[40] Bas W van Oudheusden, Fulvio Scarano, Eric WM Roosenboom, Eric WF Casimiri, and Louis J Souverein. Evaluation of integral forces and pressure fields from planar velocimetry data for incompressible and compressible flows. *Experiments in Fluids*, 43 (2-3):153–162, 2007.

[41] BW Van Oudheusden. Piv-based pressure measurement. *Measurement Science and Technology*, 24(3):032001, 2013.

[42] Joe Hoffman. *Chapter 9. Elliptic partial differential equations*, volume 2. McGraw–Hill, ISBN 0-8247-0443-6, 2001.

[43] Glenn Research Center, NASA
https://www.grc.nasa.gov/www/k-12/airplane/tunbalext.html

[44] TU Delft Wind Tunnel Lab: *M-Tunnel*
http://www.lr.tudelft.nl/organisatie/afdelingen/aerodynamics-wind-energy-flight-performance-and-propulsion/facilities/wind-tunnel-lab/

[45] H.J. Alons. *OJF External Balance*. Nationaal Lucht en Ruimtevaartlaboritorium (National Aerospace Laboratory NLR), 2008.

[46] LaVision. 3D Calibration plates.
http://lavision.de/en/products/strainmaster/system-components/calibration-plates/index.php

[47] Wieneke B (2003) Stereo-PIV using self-calibration on particle images. In: Proceedings of the 5h international symposium on PIV, Busan, Korea, September 2003.

[48] J. Westerweel. Fundamentals of digital particle image velocimetry. *Measurement Science and Technology*, 8:1379–1392, 1997.

[49] Edzard Mercker and Jochen Wiedemann. On the correction of interference effects in open jet wind tunnels. Technical report, SAE Technical Paper, 1996.

[50] Kevin Cooper. Bluff-body blockage corrections in closed-and open-test-section wind tunnels. *Wind Tunnel Wall Correction (AGARD-AG-336), BFR Ewald, ed., Advisory Group for Aerospace Research and Development, North Atlantic Treaty Organization, Neuilly-sur-Seine Cedex, France*, 1998.

[51] HC Garner, EW Rogers, WE Acum, and EC Maskell. Subsonic wind tunnel wall corrections (agardograph-109). *Advisory Group For Aerospace Research And Development Neuilly-Sur-Seine (France)*, 1966.

[52] Hendrik Tennekes and John Leask Lumley. *A first course in turbulence*. MIT press, 1972.

[53] Yuichi Murai, Taishi Nakada, Takao Suzuki, and Fujio Yamamoto. Particle tracking velocimetry applied to estimate the pressure field around a savonius turbine. *Measurement science and technology*, 18(8):2491, 2007.

[54] A. Sciacchitano and B. Wieneke, PIV uncertainty propagation, Meas. Sci. Technol. 27 084006 (2016).

[55] Coleman H W and Steele W G 2009 *Experimentation, Validation, and Uncertainty Analysis for Engineers* 3rd edition (Hoboken, NJ: Wiley).

[56] Benedict L H and Gould R D 1996 Towards better uncertainty estimates for turbulence statistics *Exp. Fluids* 22 129–36.

[57] Ghaemi S, Scarano F (2013) Turbulent structure of high-amplitude pressure peaks within the turbulent boundary layer. J Fluid Mech 735:381–426.

[58] Joshi P, Liu X, Katz J (2014) Effect of mean and fluctuating pressure gradients on boundary layer turbulence. J Fluid Mech 748:36.

[59] L. Sirovich, "Turbulence and the dynamics of coherent structures, parts i-iii," Quart. J. Appl. Math. 45(3), 561 (1987).

[60] Winkler A and Pernpeintner A. Automated Aerodynamic Optimization of the Position and Posture of a Bobsleigh, Procedia Engineering 2 (2010) 2399–2405.

A

Uncertainty of time-averaged pressure

This appendix presents the full derivation of the expression for the uncertainty of time-averaged pressure from the Poisson's equation. The Poisson's equation for average pressure in Eqn. 4.16 is expressed in Cartesian coordinates as follows:

$$\frac{\partial^2 \bar{p}}{\partial x^2}+\frac{\partial^2 \bar{p}}{\partial y^2}=-\rho\left\{\left(\frac{\partial \bar{u}}{\partial x}\right)^2+\left(\frac{\partial \bar{v}}{\partial y}\right)^2+\bar{u}\frac{\partial^2 \bar{u}}{\partial x^2}+\bar{v}\frac{\partial^2 \bar{v}}{\partial y^2}+\bar{u}\frac{\partial^2 \bar{v}}{\partial x \partial y}+\bar{v}\frac{\partial^2 \bar{u}}{\partial x \partial y}+2\frac{\partial \bar{u}}{\partial y}\frac{\partial \bar{v}}{\partial x}+\frac{\partial^2 \overline{u'^2}}{\partial x^2}\right.$$
$$\left.+\frac{\partial^2 \overline{v'^2}}{\partial y^2}+2\frac{\partial^2 \overline{u'v'}}{\partial x \partial y}\right\} \tag{A.1}$$

The Eqn. A.1 can be simplified by using the differential form of the continuity equation

$$\bar{u}\frac{\partial^2 \bar{u}}{\partial x^2}+\bar{v}\frac{\partial^2 \bar{v}}{\partial y^2}+\bar{u}\frac{\partial^2 \bar{v}}{\partial x \partial y}+\bar{v}\frac{\partial^2 \bar{u}}{\partial x \partial y}=\bar{u}\frac{\partial}{\partial x}\cancelto{0}{\left(\frac{\partial \bar{u}}{\partial x}+\frac{\partial \bar{v}}{\partial y}\right)}+\bar{v}\cancelto{0}{\left(\frac{\partial \bar{u}}{\partial x}+\frac{\partial \bar{v}}{\partial y}\right)}=0 \tag{A.2}$$

Implementing the above simplification into Equation A.1, we get the following simplified equation

$$\frac{\partial^2 \bar{p}}{\partial x^2}+\frac{\partial^2 \bar{p}}{\partial y^2}=-\rho\left\{\left(\frac{\partial \bar{u}}{\partial x}\right)^2+\left(\frac{\partial \bar{v}}{\partial y}\right)^2+2\frac{\partial \bar{u}}{\partial y}\frac{\partial \bar{v}}{\partial x}+\frac{\partial^2 \overline{u'^2}}{\partial x^2}+\frac{\partial^2 \overline{v'^2}}{\partial y^2}+2\frac{\partial^2 \overline{u'v'}}{\partial x \partial y}\right\} \tag{A.3}$$

The terms in the Eqn. A.3 are evaluated by using the central differencing scheme as follows

$$\frac{\partial^2 \bar{p}}{\partial x^2}=\frac{\bar{p}_{i+1}-2\bar{p}_i+\bar{p}_{i+1}}{(\Delta x)^2};\quad \frac{\partial^2 \bar{p}}{\partial y^2}=\frac{\bar{p}_{j+1}-2\bar{p}_j+\bar{p}_{j-1}}{(\Delta y)^2} \tag{A.4}$$

$$\left(\frac{\partial \bar{u}}{\partial x}\right)^2=\left(\frac{\bar{u}_{i+1}-\bar{u}_{i-1}}{2\Delta x}\right)^2;\quad \left(\frac{\partial \bar{v}}{\partial y}\right)^2=\left(\frac{\bar{v}_{j+1}-\bar{v}_{j-1}}{2\Delta y}\right)^2 \tag{A.5}$$

$$2\frac{\partial \bar{u}}{\partial y}\frac{\partial \bar{v}}{\partial x}=2\left(\frac{\bar{u}_{j+1}-\bar{u}_{i-1}}{2\Delta y}\right)\left(\frac{\bar{v}_{i+1}-\bar{v}_{i-1}}{2\Delta x}\right) \tag{A.6}$$

$$\frac{\partial^2 \overline{u'^2}}{\partial x^2} = \frac{\overline{u_{\iota+1}{}'^2} - 2\overline{u_\iota{}'^2} + \overline{u_{\iota-1}{}'^2}}{(\Delta x)^2} \;;\quad \frac{\partial^2 \overline{v'^2}}{\partial y^2} = \frac{\overline{v_{\iota+1}{}'^2} - 2\overline{v_\iota{}'^2} + \overline{v_{\iota-1}{}'^2}}{(\Delta y)^2} \tag{A.7}$$

$$2\frac{\partial^2 \overline{u'v'}}{\partial x \partial y} = \frac{1}{2d^2}\left(\overline{u'_{\iota+1,\jmath+1}v'_{\iota+1,\jmath+1}} - \overline{u'_{\iota+1,\jmath+1}v'_{\iota+1,\jmath+1}} - \overline{u'_{\iota+1,\jmath+1}v'_{\iota+1,\jmath+1}} + \overline{u'_{\iota+1,\jmath+1}v'_{\iota+1,\jmath+1}}\right) \tag{A.8}$$

The uncertainties of all the terms of the Poisson's equation are evaluated using the linear uncertainty propagation formula and is represented as follows:

Uncertainty of the LHS:

It is assumed that the uncertainty of mean pressure is equal to $U_{\bar{p}}$ at all the grid points

$$\begin{aligned}\left(U_{\frac{\partial^2 \bar{p}}{\partial x^2}}\right)^2 &= \left(\frac{1}{(\Delta x)^2}\right)^2 . \left(U_{\bar{p}_{i-1}}\right)^2 + \left(\frac{-2}{(\Delta x)^2}\right)^2 . \left(U_{\bar{p}_i}\right)^2 + \left(\frac{1}{(\Delta x)^2}\right)^2 . \left(U_{\bar{p}_{i+1}}\right)^2 \\ &= \frac{6}{d^4}\left(U_{\bar{p}}\right)^2\end{aligned} \tag{A.9}$$

Similarly,

$$\left(U_{\frac{\partial^2 \bar{p}}{\partial y^2}}\right)^2 = \frac{6}{d^4}\left(U_{\bar{p}}\right)^2$$

Therefore

$$\left(U_{\frac{\partial^2 \bar{p}}{\partial x^2}+\frac{\partial^2 \bar{p}}{\partial y^2}}\right)^2 = \left(U_{\frac{\partial^2 \bar{p}}{\partial x^2}}\right)^2 + \left(U_{\frac{\partial^2 \bar{p}}{\partial y^2}}\right)^2 = \frac{12}{d^4}\left(U_{\bar{p}}\right)^2 \tag{A.10}$$

Uncertainty of the RHS:

It is assumed that the uncertainty of all the mean velocity components is equal to $U_{\bar{V}}$ at all grid points. In this case, $\bar{V} = \{\bar{u} \quad \bar{v}\}$

$$\left(U_{\left(\frac{\partial \bar{u}}{\partial x}\right)^2}\right)^2 = \left(\frac{\bar{u}_{i+1} - \bar{u}_{i-1}}{2(\Delta x)^2}\right)^2 \left(U_{\bar{u}_{i+1}}\right)^2 + \left(\frac{\bar{u}_{i-1} - \bar{u}_{i+1}}{2(\Delta x)^2}\right)^2 \left(U_{\bar{u}_{i-1}}\right)^2$$

$$= \left(\frac{1}{d}\left(\frac{\partial \bar{u}}{\partial x}\right)\right)^2 (U_{\bar{V}})^2 + \left(\frac{-1}{d}\left(\frac{\partial \bar{u}}{\partial x}\right)\right)^2 (U_{\bar{V}})^2 = \frac{2}{d^2}\left(\frac{\partial \bar{u}}{\partial x}\right)^2 (U_{\bar{V}})^2 \tag{A.11}$$

Similarly,

$$\left(U_{\left(\frac{\partial\bar{v}}{\partial y}\right)^2}\right)^2 = \frac{2}{d^2}\left(\frac{\partial\bar{v}}{\partial y}\right)^2 (U_{\bar{V}})^2$$

$$\begin{aligned}\left(U_{2\left(\frac{\partial\bar{u}}{\partial y}\cdot\frac{\partial\bar{v}}{\partial x}\right)}\right)^2 &= \left[\frac{1}{2\Delta y}\cdot\left(\frac{\partial\bar{v}}{\partial x}\right).2\right]^2\left(U_{\bar{u}_{j+1}}\right)^2 + \left[\frac{-1}{2\Delta y}\cdot\left(\frac{\partial\bar{v}}{\partial x}\right).2\right]^2\left(U_{\bar{u}_{j-1}}\right)^2 \\ &+ \left[\frac{1}{2\Delta x}\cdot\left(\frac{\partial\bar{u}}{\partial y}\right).2\right]^2\left(U_{\bar{u}_{i+1}}\right)^2 + \left[\frac{-1}{2\Delta x}\cdot\left(\frac{\partial\bar{u}}{\partial y}\right).2\right]^2\left(U_{\bar{u}_{j+1}}\right)^2 \\ &= \frac{2}{d^2}(U_{\bar{V}})^2\left[\left(\frac{\partial\bar{v}}{\partial x}\right)^2 + \left(\frac{\partial\bar{u}}{\partial y}\right)^2\right] \qquad (A.12)\end{aligned}$$

It is also assumed that the uncertainty of all components of Reynolds normal stress is equal to $U_{\overline{V'^2}}$ and the uncertainty of all components of Reynolds shear stress is equal to $U_{\overline{u'v'}}$ at all the points of the grid. In this case, $U_{\overline{V'^2}} = \left\{U_{\overline{u'^2}} \quad U_{\overline{v'^2}}\right\}$

$$\begin{aligned}\left(U_{\frac{\partial^2\overline{u'^2}}{\partial x^2}}\right)^2 &= \left(\frac{1}{(\Delta x)^2}\right)^2\cdot\left(U_{\overline{u'^2}_{i+1}}\right)^2 + \left(\frac{-2}{(\Delta x)^2}\right)^2\cdot\left(U_{\overline{u'^2}_{i}}\right)^2 \\ &+ \left(\frac{1}{(\Delta x)^2}\right)^2\cdot\left(U_{\overline{u'^2}_{i-1}}\right)^2 \\ &= \frac{6}{d^4}\cdot\left(U_{\overline{V'^2}}\right)^2 \qquad (A.13)\end{aligned}$$

Similarly,

$$\left(U_{\frac{\partial^2\overline{v'^2}}{\partial y^2}}\right)^2 = \frac{6}{d^4}\cdot\left(U_{\overline{V'^2}}\right)^2$$

$$\begin{aligned}\left(U_{2\left(\frac{\partial^2\overline{u'v'}}{\partial x\partial y}\right)}\right)^2 &= \left(\frac{1}{2d^2}\right)^2\cdot\left(U_{\overline{u'_{i+1,j+1}v'_{i+1,j+1}}}\right)^2 \\ &+ \left(\frac{-1}{2d^2}\right)^2\cdot\left(U_{\overline{u'_{i+1,j-1}v'_{i+1,j-1}}}\right)^2 \\ &+ \left(\frac{-1}{2d^2}\right)^2\cdot\left(U_{\overline{u'_{i-1,j+1}v'_{i-1,j+1}}}\right)^2 + \left(\frac{1}{2d^2}\right)^2\cdot\left(U_{\overline{u'_{i-1,j-1}v'_{i-1,j-1}}}\right)^2 \\ &= \frac{1}{d^4}\cdot\left(U_{\overline{u'v'}}\right)^2 \qquad (A.14)\end{aligned}$$

The uncertainties of all the terms of the Poisson's equation can be related as follows

$$\left(U_{\frac{\partial^2\bar{p}}{\partial x^2}+\frac{\partial^2\bar{p}}{\partial y^2}}\right)^2 = \left(U_{\left(\frac{\partial\bar{u}}{\partial x}\right)^2}\right)^2 + \left(U_{\left(\frac{\partial\bar{v}}{\partial y}\right)^2}\right)^2 + \left(U_{2\left(\frac{\partial\bar{u}}{\partial y}\cdot\frac{\partial\bar{v}}{\partial x}\right)}\right)^2 + \left(U_{\frac{\partial^2\overline{u'^2}}{\partial x^2}}\right)^2 + \left(U_{\frac{\partial^2\overline{v'^2}}{\partial y^2}}\right)^2 + \left(U_{2\left(\frac{\partial^2\overline{u'v'}}{\partial x\partial y}\right)}\right)^2 \quad (A.15)$$

Substituting the evaluation of every term computed above, the following equation is obtained

$$\frac{12}{d^4}\left(U_{\bar{p}}\right)^2 = \left[\frac{2}{d^2}(U_{\bar{V}})^2\left(\left(\frac{\partial\bar{u}}{\partial x}\right)^2 + \left(\frac{\partial\bar{v}}{\partial y}\right)^2 + \left(\frac{\partial\bar{u}}{\partial y}\right)^2 + \left(\frac{\partial\bar{v}}{\partial x}\right)^2\right)\right] + \frac{12}{d^4}.\left(U_{\overline{V'^2}}\right)^2 + \frac{1}{d^4}.\left(U_{\overline{u'v'}}\right)^2$$

$$U_{\bar{p}} = \frac{\rho d}{\sqrt{12}}\sqrt{\left[2(U_{\bar{V}})^2\left(\left(\frac{\partial\bar{u}}{\partial x}\right)^2 + \left(\frac{\partial\bar{v}}{\partial y}\right)^2 + \left(\frac{\partial\bar{u}}{\partial y}\right)^2 + \left(\frac{\partial\bar{v}}{\partial x}\right)^2\right)\right] + \left[\frac{12}{d^2}\left(U_{\overline{V'^2}}\right)^2\right] + \left[\frac{1}{d^2}\left(U_{\overline{u'v'}}\right)^2\right]} \quad (A.16)$$

The equation (A.16) derived above is the expression to evaluate the uncertainty of time-averaged mean pressure.